Stratification of Cathode Catalyst Layers for Low-temperature Proton Exchange Membrane Fuel Cells (PEMFC)

By Zikhona Zisanele Nondudule

Thesis

Submitted in partial fulfillment of the requirements for the degree of

Master of Engineering in Chemical Engineering

Supervised by:

Dr. Mahabubur Chowdhury (Supervisor)

Dr. Jessica Chamier (Co-supervisor)

Faculty of Engineering

Department of Chemical Engineering

Cape Peninsula University of Technology

December 2020

Plagiarism Declaration:

I know the meaning of plagiarism and declare that all the work in the document, except for that which is properly acknowledged, is my own.

Synopsis

Over the past few years, significant progress has been made to commercialize proton exchange membrane fuel cells (PEMFC) however, they are still being manufactured at a high cost. PEMFCs currently use platinum as a catalyst for both anode and cathode which vastly contributes to the high raw material cost. The great value of platinum as a catalyst in PEMFC applications is that it outperforms all other catalysts in its activity, selectivity as well as stability (Holton & Stevenson, 2013).

The rate of the oxidation reduction reaction (ORR) occurring in the cathode catalyst layer primarily determines the cell voltage, as the rate of the anodic reaction is considerably faster by comparison. The characteristics of the cathode catalyst layer, therefore, have a huge impact on the overall performance of PEMFC. The existing PEMFC cathode catalyst layers (CCLs) are sub-optimally designed, leading to significant mass transport limitations that result in inefficient catalyst utilization. Many works have been done to improve the CCL characteristics which concluded that porosity variation in the catalyst layer improved membrane electrode assembly (MEA) performance. Designing an electrode with a distinctive inner and outer catalyst layer to improve the ORR was proposed by Yoon et al., (2003). This technique is called stratification and was used in this study to optimize the cathode catalyst (CL). In the current study Ionomer gradient MEAs were designed to increase Pt utilization in the catalyst layer enabling Pt loading reduction, without sacrificing performance and lifetime. To study the MEA performance, the electrochemical surface area (ECSA), polarization curves, and electrochemical impedance spectroscopy (EIS) responses were evaluated under various relative humidity (RH) conditions. The integrity of stratified MEAs was tested by conducting an electrochemical carbon corrosion test and was compared to that of a monolayer MEAs.

The optimal two-layer design was achieved when the Pt loading ratio between the layers was 1:6. An MEA containing this ratio presented the highest electrochemical surface area (ECSA) and highest performance at 0.65 V with reduced mass transport losses. Using ionomer stratification to decrease the Pt loading in an MEA yielded better performance compared to the traditional monolayer MEA. Stratified MEAs were shown to be more durable than monolayer MEAs both at high (0.4 $mgPt/cm^2$) and lower (0.35 $mgPt/cm^2$) Pt loadings. The high ionomer loading adjacent to the membrane and the bi-layer interface of the stratified CCL increased moisture in the CL, decreasing the degradation rate of the stratified CCLs. This study, therefore, contributes to the development of more durable MEAs for low-temperature PEMFCs.

Acknowledgements

I have been very fortunate to have done my masters project through the University of Cape Town. It has been an exciting experience and I have learnt a lot. Firstly, I would like to thank God almighty for giving me the strength to persevere and complete my studies through everything. I would like to thank my former manager Nabeel Hussain for affording me with this opportunity and for always believing in me. I want to thank Hyplat (pty) Ltd. for allowing me to partake in this journey with them, particularly Sharon Blair for supporting my studies. My gratitude extends to Shawn Solomons and Francois van Schalkwyk who assisted me with setting up my experiments. It would have never been possible without them.

To my co-supervisor Jessica, I know this has been a long journey for both of us. You put up with me when I could not juggle between my job and studies; you continue to support me tirelessly even when I am slacking. Your patience and kindness are incomparable and for that, I will always be grateful.

Dr. Mahabubur Chowdhury, thank you for accepting me as one of your students and guiding me through this process.

I would like to thank Shuang Ma Andersen (Department of Green Technology, University of Southern Denmark), Miranda Waldron (Centre for Imaging and Analysis, UCT), Darija Susac (Centre for Catalysis Research, UCT), and Firdaus Hendricks (HySA catalysis, UCT) for the tremendous amount of effort put into assisting me with physical characterization. I also want to thank Humbulani Negondeni and Zuko Ntengo for using their precious time to assist me with drawings.

A special thanks to my family- my mother, Zoleka Nondudule, my sister in law, Lungelwa Homana, and my brother, Bongani Nondudule, who were always willing to take care of my daughter so I could have more time for my studies.

Lastly, I would like to thank my partner Motlokoa Khasu for being the love and support that I needed the most. And my daughter Iyana for understanding and tolerating me when I was not at my best. I love you endlessly.

Contents

List of Figures

List of Tables

Nomenclature

Symbol	Description	Unit
e^-	Electron	
H^+	Proton	
σ	Ionic conductivity	
τ	Average crystallite size	nm
E^0	Potential energy	
I	Current	
R_i	Internal resistance	Ω
V	Voltage	
V_b	Scan rate	mv/s
Q	Total charge	$\mu C/cm^2$
Q_f	Gibbs free energy of formation	

Constants

Constant	Value	Unit	Description
F	96485	C/mol	Faraday's constant

Glossary

Abbreviation	Description
BET	Brunauer, Emmett, and Teller
CL	Catalyst layer
CCL	Cathode catalyst layer
CV	Cyclic voltammetry
ECSA	Electrochemical surface area
H_{ads}	Hydrogen adsorption
H_{des}	Hydrogen desorption
HOR	Hydrogen oxidation reaction
FC	Fuel cell
MEA	Membrane electrode assembly
ORR	Oxygen reduction reaction
PEM	Proton/polymer exchange membrane
PEMFC	Proton exchange membrane fuel cell
Pt	Platinum
Pt/C	Platinum supported on carbon
PtO	Platinum Oxide
SEM	Scanning electron microscopy
TBP	Triple phase boundary

CHAPTER 1

1. Introduction

1.1. Motivation of study

As the global demand for energy increases, conventional power sources that rely on hydrocarbons are being gradually replaced by low to zero-emission energy sources. Alternative energy sources are emerging resulting in the structural change of supply, demand, and prices in the energy sector. This has been witnessed in the power sector where coal has been substituted by more affordable wind and solar energy (Cohen, 2019) The transportation sector does not deviate from this transition. Automotive manufacturers such as Chevrolet, Toyota, Honda, BMW, etc. have started manufacturing fuel cell electric vehicles (FCEV) and plugin-hybrid vehicles. These vehicles are slowly penetrating the market replacing the internal combustion engine vehicles that have been in the market for over 100 years (Cohen, 2019).

Hydrogen fuel cell vehicles work by combining hydrogen (H_2) fuel stored in the tank with oxygen (O_2) in the air to produce electricity through a chemical reaction, generating water and heat as byproducts. Figure 1.1 shows the operation of a basic hydrogen fuel cell.

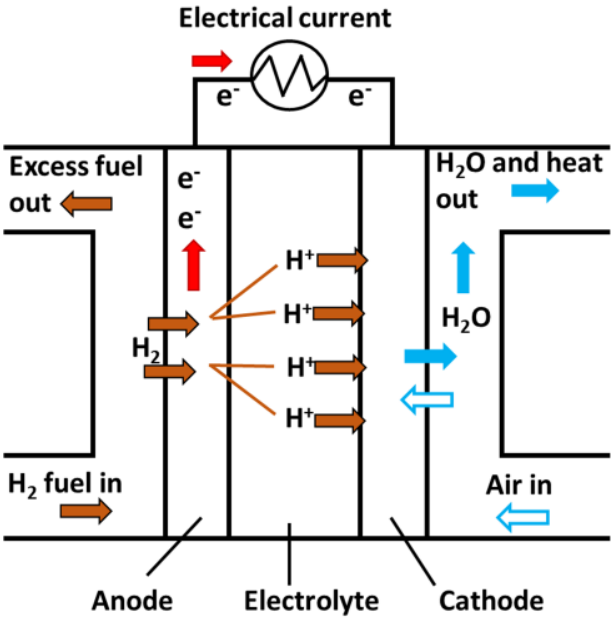

Figure 1.1. Illustration of how electricity is generated in a fuel cell.

Hydrogen energy has been widely recognized as the most promising alternative sustainable energy source for the future. Hydrogen, like electricity, is a carrier of energy that can deliver a substantial amount of energy. The chemical energy available in hydrogen can be converted into mechanical energy either by burning hydrogen in internal combustion engines or through a chemical reaction in a fuel cell (Anon., 2018). As the world attempts to combat climate change, hydrogen fuel cells offer emission-free energy with low to zero pollutants. They are adaptable in both the transportation and industrial sector, which are currently highly dependent on depleting fossil fuels for energy. Not only is hydrogen clean but it can be safely stored and easily transported. At present, the most suitable fuel cell being developed for transport, stationary, and portable fuel cell applications is the proton-exchange membrane fuel cell (PEMFC).

According to market research, slow but significant progress has been made in the fuel cell electric vehicle (FCEV) market. About 6500 FCEVs were sold worldwide between 2013-2017 (Ray, 2018). However, fuel cell buses and cars are still surpassed by full electric cars and buses by a factor of about one hundred (Harop, 2019). Fuel cells have been long introduced to penetrate the market, however, switching from fossil fuels to fuel cells comes with its challenges. One of the major challenges is the cost of commercializing PEMFCs. These challenges may be overcome with more advancements and developments in fuel cell technology, materials, and component design.

1.2. PEMFC challenges towards commercialization

The accomplishment of PEMFCs in stationary and mobile applications in the commercial sector has encouraged its use in other applications. Successful commercialization of PEMFCs can be seen once they can produce a high performance at a low cost (Cetinbas et al., 2015). High cost and durability have been identified as the two major barriers that hinder large-scale commercialization (Zhang, 2008). Most fuel cells currently use Platinum group metals (PGMs) (in the form of nanoparticles dispersed on carbon black support) as catalysts for the hydrogen oxidation reaction (HOR) and oxygen reduction reaction (ORR). One of the main approaches for cost reduction is to replace platinum with less expensive nanoparticle alloys without compromising the durability and efficiency of the MEA (Kongkanand & Mathias, 2016). Alternatively, platinum loading in a catalyst layer can be reduced.

The ORR occurring at the cathode is about 6 orders of magnitude slower than the HOR on the anode and thus limits performance. As a result, more PGMs are required for the cathode which increases raw material cost. This is a renowned challenge. Consequently, almost all research and development efforts

are aimed at improving cathode catalysts for the ORR. This includes improving both the activity and utilization of the catalyst as well as its durability and stability (Banham & Ye, 2017). How the Pt loading can be reduced without compromising durability and efficiency of the MEA remains a key question. Fuel cell vehicles monitored by the United States Department of Energy (US DOE) are reported to have used approximately 0.4 mg. cm^{-2} cathode Pt loading for automotive vehicles. The US DOE aims to achieve a cost target of $40/kW for transportation MEAs and reduce PGM total loading for both electrodes to 0.125 mg. cm^{-2} by the year 2020 (Debe, 2012).

1.3. Decreasing PGM loading

Significant progress has been made in reducing Pt loading for H_2/air PEMFCs which has led to the current application of 0.6-0.8 mg_{Pt}/cm^2 total MEA PGM loading (Gasteiger et al., 2005). Even though this has been a remarkable improvement compared to the late 1990s, recent developments in automotive applications encourage further reductions based on reasons of both cost and Pt supply limitations (Gasteiger et al., 2005). While lowering the Pt loading for the anode HOR is relatively simple, lowering the cathode loading from the current 0.4 mg/cm^2 remains a challenge due to the poor ORR kinetics. As a result, many studies have been focused on reducing Pt loading for PEMFCs to <0.1 mg/cm^2. These studies include novel methods for the development of new carbon supports and the implementation of distinct electrode fabrication methods. Severe performance losses have also been observed at high current densities (>1 A/cm^2) for low Pt loading MEAs due to significant O_2 transport resistance (Kongkanand & Mathias, 2016).

The first method enabling the Pt load reduction is the thin film method proposed by Wilson et al (1995). This method uses an impregnation technique, where Nafion solution is impregnated into the catalyst layer. The advantage of this method is that Polytetrafluoroethylene (PTFE) is added to the CL for water management. The disadvantage of this method is that it is difficult to control the amount of Nafion impregnated into the CL. The inability of Nafion to access all catalyst sites results in 10-20 % catalyst utilization (Wilson et al., 1995). The second approach was to mix Nafion with the supported catalyst in the presence of glycerol (Qi & Kaufmann, 2003). Glycerol was added to form a relatively viscous mixture that can hold the catalyst particles in suspension without forming agglomerates. The third approach was to mix Nafion with an organic solvent before adding the catalyst to the solution. This method resulted in a good homogeneous distribution of Nafion across the CL. The disadvantage of the above two methods is that PTFE cannot be added to the CL i.e. there is no water management, which causes the MEA to flood. New methods have emerged since the development of thin-film methods. Some of these methods include

the electrodeposition method (Brancovic et al., 2001), sputtering technique (Rabat & Brault, 2007), carbon nanotubes (CNTs) (Kim et al., 2008). Pt loadings as low as 0.04 mg_{Pt}/cm^2 have been reported from using the above methods. However, most of these methods are not commercially viable and still face technical problems such as reduced catalytic activity, long-term testing, and MEA structure durability (Gasteiger et al., 2005). Also, the cost of preparation of such MEAs is also dubious. Table 1.1 gives a summary of some of the fabrication methods used to reduce Pt loading in CCLs in PEMFCs with their achievements and challenges faced.

Table 1.1. A summary of electrocatalyst fabrication methods used for Pt loading reduction purposes, their advantages, and disadvantages.

Fabrication methods	Advantages	Drawbacks
Thin-film method	Relatively higher Pt utilization at lower loadings (less than 0.05 $mgPt/cm^2$); No deformation/cracking of the catalyzed layer due to lower hot-pressing temperatures & pressure; Improved contact between membrane and electrode interface	difficult to control the Pt particle size; catalyst cannot be uniformly deposited across the CL
Electrode deposition	Relatively higher Pt utilization; good Pt particle size distribution at high Pt content	Relatively high Pt loadings-higher Pt loadings used for the anode (0.7 $mgPt/cm^2$); Includes complex processes which limits large scale commercialization; produces chloride ions which are known to poison Pt and reduce the catalytic activity
Sputter deposition	Lowest loadings; Pt can be deposited into various subrates such as membrane, GDL or NCL. Easy to scale-up; uniform distribution of Pt across the CL; cheaper fabrication method	lower Pt utilization; poor contact between Pt and substrate; short durability i.e., weak physical structure
Dual-ion beam assisted deposition	Relatively low Pt loadings and higher Pt utilization	Complex processes involved which is a great concern on scalability for mass production; lower power density
Electroless deposition method	Effective for Pt/Ru binary anode electrocatalyst	High fabrication cost; large particle sizes caused by agglomeration
Deposition on sonochemically treated carbon nanotubes (CNT)	Relatively low Pt loading and high Pt utilization	High price for synthesis on CNTs; highly dependent on Pt loading methods

Another promising alternative is the development of graduated multi-layer catalyst layers. Graduated CL structure MEAs can increase the Pt catalyst efficiency by increasing the available Pt surface area resulting

in improved ORR. Recent studies have shown O_2 mass transport resistance to be inversely proportional to Pt loading and highly dependent on the available Pt surface area (Greszlar et al., 2012). Taking a step towards successful commercialization requires ORR electrocatalysts that can meet performance targets, are low in cost, and highly durable. Currently not all proposed approaches meet these demands. This study will focus on reducing the Pt loading of CCLs through ionomer graduation/stratification using the ultra-sonic spraying fabrication.

1.4. Problem statement

Fuel cell manufacturers are working tirelessly to reduce costs to grow the fuel cell market. However, the use of Pt as a catalyst results in high costs of manufacturing PEMFCs ($/kW) which hinders this progress. Optimizing cathode catalyst layer (CCL) design to enhance Pt utilization and reduce Pt loading can reduce the cost of PEMFC, and more specifically MEAs. Over the years, many structures and fabrication methods have been made to improve mass transport in the CCLs. The catalyst layer must have good water management so that it can maintain good performance. However, it is impossible to the increase thickness of a catalyst layer (CL) without compromising proton resistance, electronic resistance, and mass transport resistance (Malko et al., 2016). Increasing Pt loading can reduce activation losses but deteriorate mass transport due to reduced porosity in the CL. Likewise, increasing ionomer content can improve proton conductivity but at the cost of reduced mass transport due to lower porosity (Cetinbas et al., 2015).

Recent studies show that irregular thickness and porosity in cathode catalyst layers enhance mass transport of gases and water in and out of the CL (Macauley et al., 2018). It was found that the design of functionally graded MEAs showed improved performance in comparison with monolayer MEAs (Xie et al., 2005). However, none of these studies showed that increasing Pt utilization could allow for the reduction of the Pt loading in the CCLs while maintaining high performance. The durability of such MEAs has also not been tested. This project will focus on designing a functionally graded low-temperature PEMFC MEA with high efficiency and lower Pt loading in the CCLs. Herein, the Pt use efficiency is improved allowing for MEA ($/kW) cost reduction.

1.5. Hypothesis and Objectives

Thickness and porosity variation in the catalyst layer have been proven to significantly improve performance by allowing more reactants to flow in and out of the CL as well as improve water management in the cathode. Even though homogenous ionomer coverage is desirable for effective proton

transport, it is also detrimental for gaseous reactant transport as it hinders reactants from accessing the catalyst's active site (Zhao & Benziger, 2013). It is hypothesized that designing a CCL with non-uniform ionomer distribution may increase the efficiency of the Pt catalyst and minimize the need for higher Pt loadings in the cathode CL. This will be due to higher porosity and mean size, and hence higher permeability, providing higher catalyst activity and Pt utilization than the conventional MEA mono-layer design under the same overall Pt loadings. On the other hand, an MEA with non-uniformly distributed ionomer loading CCLs is expected to have performance parity with the conventional 0.4 mg_{Pt}/cm2 monolayer MEAs, at reduced Pt loadings.

The goal of this project is to design an MEA with decreased Pt loading with commercial benchmarked performance. To achieve this goal, the project has the following objectives:

- To determine the optimal ionomer content for a single monolayer CCL at specific relative humidity conditions;
- Improve the Pt use efficiency of a CCL in an MEA by stratification of the CCL using varying ionomer ratios;
- Design a CCL composition and structure, with reduced Pt content that can demonstrate an equal or greater performance compared to non-stratified MEA;
- Compare the durability of the stratified MEA against the monolayer benchmark with higher Pt loading.

The graded design is stratified along the through-plane direction in the membrane. It is hypothesized that designing a CCL with non-uniform ionomer distribution may increase the efficiency of the Pt catalyst and minimize the need for higher Pt loadings in the cathode CL.

1.6. Contribution of the study

1.6.1. Knowledge contribution

A significant amount of literature focused on improving the Pt use efficiency and the ORR performance in CCLs, yet there is seldom a result in the production of a lower PGM MEA which can break through to the commercial market. Some researchers have successfully managed to decrease the Pt loading of CCLs for PEMFCs yet none of their methods can be employed for large-scale commercialization due to their complex procedures or high fabrication cost. This project will look at reducing the Pt loading of CCLs for PEMFC using a fabrication technique that will allow mass production: the ultrasonic-sprayer technique.

A few studies have been carried out for ionomer-gradient design CCLs to increase Pt utilization, yet there are very few focusing on reducing Pt loading in these MEA designs. The answer to whether these MEAs can operate at lower Pt loadings is elusive. This project will therefore reduce the knowledge gap by addressing the question of whether increased Pt use efficiency in stratified MEAs allows for lower PGMS loading without sacrificing cell performance. It is one of the few studies to use ultra-sonic spraying coating to investigate Pt loading using the CCM technique and to stratify MEAs using this procedure. The effect of Pt loading distribution in the sublayers on performance, morphology, microstructure, and electrochemical activity of an MEA is also investigated.

1.6.2. Economic impact

This project is incentivized by commercial interest. Manufacturing MEAs at a lower cost with equivalent performance and durability brings the industry closer towards achieving the US DOE Pt loading target for 2020. Decreased MEA costs and increased production, could accelerate the financial viability of hydrogen fuel cells in the energy sector.

1.7. Thesis organization and structure

Chapter 1 introduces the scope of the project in the fuel cell sector. Chapter 2 presents a relevant literature review on the development of high-performance PEMFC MEAs and recent advances on multiple layer and stratified MEAs. It also gives a detailed overview of the properties and parameters that affect the PEMFC electrocatalysis. Chapter 3 explains the fabrication technique used for electrocatalyst synthesis of monolayer and stratified MEAs as well as testing protocols. Pt/C catalyst inks consisting of distinct ionomer contents were prepared for the fabrication of a 0.4 mg_{Pt}/cm^2 CCL monolayer MEA. Chapter 4 is the Ionomer optimization study. It discusses the electrochemical and physical properties of the different ionomer content MEAs in which the highest performing MEA was identified as the benchmark monolayer MEA. Chapter 5 is the stratification of CCL MEAs. The designed MEAs were characterized through morphological, microstructural, electrochemical, and physical characterization techniques and the performance of single cells containing such MEAs was measured. Chapter 5 describes the process of designing a double-layer MEA consisting of 0.4 mg_{Pt}/cm^2, 0.1 mg_{Pt}/cm^2 cathode and anode loadings respectively, based on the desired electrochemical and physical characteristics of the monolayer MEAs. Furthermore, it discusses the properties and performance of the stratified dual-layer MEA and compares it to the monolayer benchmark with higher Pt Loading. Chapter 6 shows the reduction of CCL Pt loading of the monolayer and ionomer gradient MEAs from 0.4 to 0.35 mg_{Pt}/cm^2. Chapter 7 presents the

conclusions on the stratification of MEAs using various ionomer content and make suggestions on where future work may lie.

CHAPTER 2

2. Literature Review

This section of the study presents a critical analysis of the relevant literature on fuel cell components and operation. It includes an overview of the fuel cell technology, a description of the Membrane Electrode Assembly (MEA), catalyst layer challenges, and a review of stratification methods used for Proton Exchange Membrane Fuel Cells (PEMFCs).

2.1. Basic principles of fuel cells

A fuel cell is a device that generates electricity by converting chemical energy into electric current. It converts the chemical energy from a fuel, typically hydrogen, to electrical energy without the use of combustion engines and with only water and heat as by-products. Every fuel cell contains an ion conducting electrolyte and two electrodes, the anode, and the cathode, respectively. The fuel is continuously fed to the anode while the oxidant is supplied to the cathode. Generally, the fuel is pure hydrogen or contains some hydrogen gases like methanol, ethanol, and natural gases (Cook, 2002). The oxidant is pure oxygen or contains oxygen gases like air or halogens such as chlorine. In a hydrogen fuel cell, hydrogen fuel is fed into the anode compartment and oxygen, typically air, is flowed into the cathode compartment. Electrochemical reactions occur at the surface of a catalyst layer (CL). The oxidation half-cell or hydrogen oxidation reaction (HOR) occurring at the anode is presented by (Haile, 2003):

Anode: $\mathrm{H_2 \rightarrow 2H^+ + 2e^-} \qquad \mathrm{E^0 = 0\ V\ at\ 25\ ℃}$ (2-1)

At the cathode, oxygen molecules react with the hydrogen ions transported through the PEM and the electrons conducted by the electric circuit to form water. The oxygen reduction reaction (ORR) occurring at the cathode is presented by:

Cathode: $\mathrm{\frac{1}{2}O_2 + 2H^+ + 2e^- \rightarrow H_2O} \qquad \mathrm{E^0 = 1.23\ V\ at\ 25\ ℃}$ (2-2)

Combining the reaction on the anode and cathode, the global reaction is:

$$\mathrm{\frac{1}{2}O_2 + H_2 \rightarrow H_2O} \qquad (2\text{-}3)$$

The proton exchange membrane fuel cell (PEMFC*)*

Since the invention of the first fuel cell by William Grove (1839), various kinds of fuel cells have been developed and based on the type of electrolyte being used. Generally, there are four application markets for FCs: primary power, backup power, combined heat and power (CHP), and FC vehicles (Alavi et al., 2017). Table 2.1 shows the different types of fuel cells and their uses.

Table 2.1. Types of fuel cells and their applications *(Larminie & Dicks, 2003)*.

FC type	Mobile ion	Operating temperature	Applications
Proton Exchange Membrane Fuel Cells (PEMFC)	H^+	50 – 100 ℃	Suitable for vehicles, mobile applications, and low power CHP systems
Direct methanol fuel cell (DMFC)	H^+	20 – 90 ℃	Suitable for portable electronic systems of low power, running for long times
Alkaline Fuel Cells (AFC)	CO^-	50 – 200 ℃	Used in space vehicles e.g. Apollo shuttles
Phosphoric acid Fuel Cell (PCFC)	H^+	220 ℃	Large numbers of 200 kW CHP systems in use
Molten Carbonate Fuel Cell (MCFC)	CO_3^{2-}	650 ℃	Suitable for medium to large scale CHP systems, up to MW capability
Solid Oxide Fuel Cell (SOFC)	O^{2-}	500 – 1000 ℃	Suitable for all sizes of CHP systems, from 2kW to multi MW

Amongst various types of fuel cells, the polymer electrolyte fuel cell (PEMFC) also known as the proton exchange membrane fuel cell has attracted great attention in research and development. The PEMFC is simple and operates at low temperature (50-100 °C) and higher power density (40%-60%) with the absence of pollutants (Fan, 2013). A PEMFC consists of two electrodes, the anode and cathode, which are both in contact with a proton-conducting membrane placed between them. This type of fuel cell operates

on pure hydrogen and oxygen gas as fuel. Hydrogen is catalytically oxidized in the anode to produce protons and electrons. The hydrogen ions are conducted through the proton-exchange membrane and permeate to the cathode where they react with oxygen to produce water and heat (Litster & McLean, 2004). Since the membrane is not electronically conductive, electrons released from the hydrogen are carried through an external circuit and an electric current is generated. Figure 2.1 presents a schematic of a typical PEMFC operation and the reactions that occur in the electrodes.

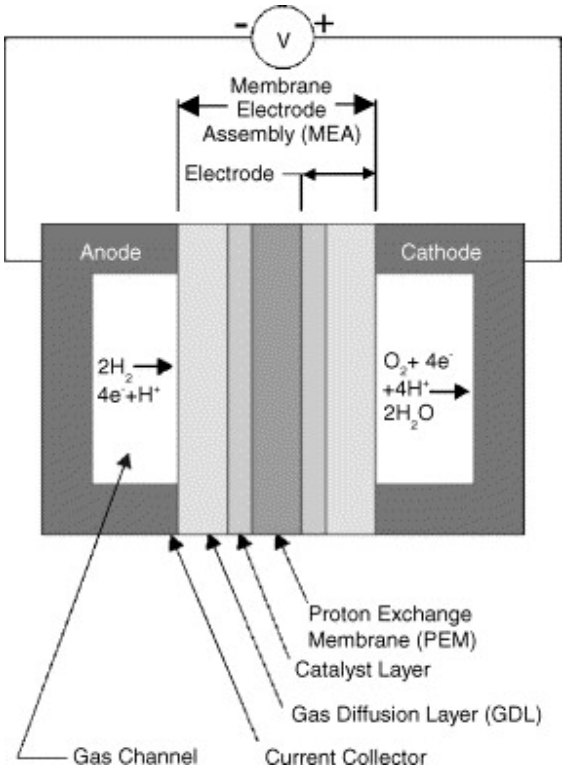

Figure 2.1. A schematic of a typical proton exchange membrane operation. Adapted from Litster and McLean (2004).

2.2. Membrane electrode assembly

At the heart of a PEMFC is the Membrane Electrode Assembly (MEA). A typical MEA consists of a proton exchange or polymer electrolyte membrane (PEM), catalyst layers, and gas diffusion layers (GDLs). These components are fabricated individually and then pressed together at high temperatures and pressures. The PEM is sandwiched between two porous, electrically conductive electrodes called GDLs. At the interface between the GDL and the membrane is a layer of catalysts where the electrochemical reactions take place. A schematic diagram showing the essential components of a fuel cell is demonstrated in Figure 2.2.

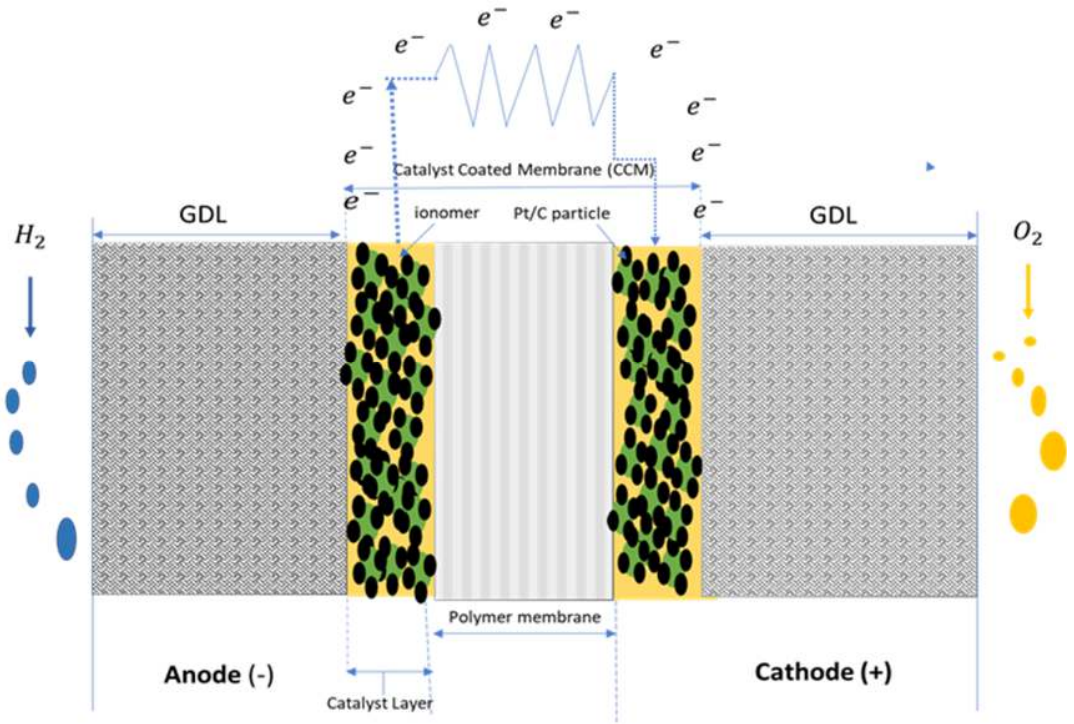

Figure 2.2. Illustration of a membrane electrode assembly depicting the three key components of an MEA: (a) Gas diffusion layer (GDL); (b) Catalyst layer; (c) Proton exchange membrane.

In the PEMFC, the MEA is responsible for facilitating three transport processes (Litster & McLean, 2004):

- Transport protons through the PEM from the anode to the cathode.
- Transport electrons through electrically conductive cell components.
- Mass transport of reactant and product gas flows through the GDLs, to and from the catalyst layer and gas channels.

There are two different types of MEA structures that have been developed and can be classified according to the location of the catalyst layer as illustrated in Figure 2.3.

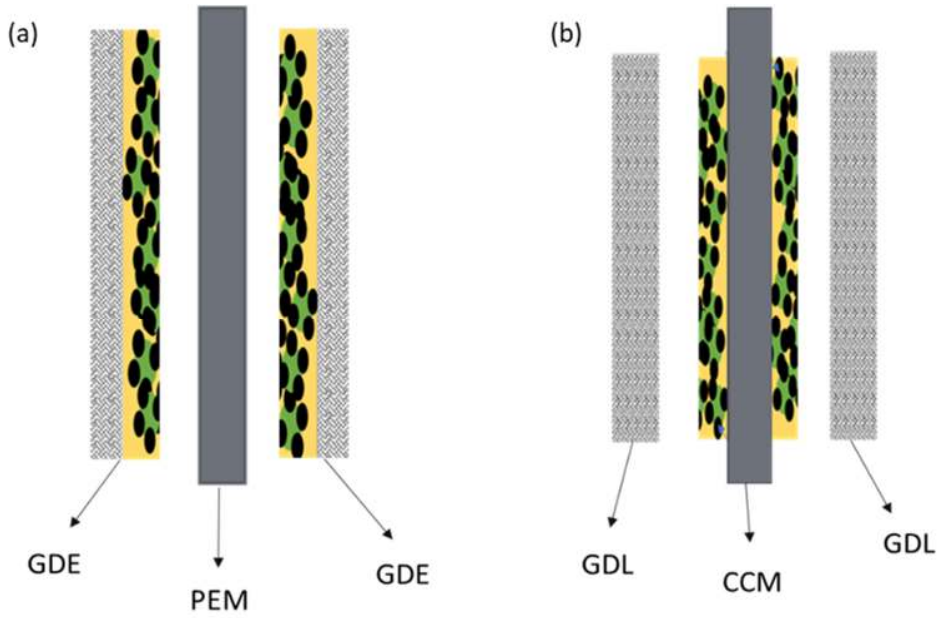

Figure 2.3. Schematic diagram of a 5-layer MEA: (a) Gas diffusion electrode; (b) Catalyst coated membrane.

Applying a catalyst ink directly on the GDL leads to a two-layer structure called a gas diffusion electrode (GDE) while applying the catalyst ink onto both sides of the proton exchange membrane results in a three-layer structure called a catalyst coated membrane (CCM). Then a final 5-layer MEA is formed when a membrane or CCM is sandwiched between two GDLs. Studies have shown improved catalyst utilization in CCM electrodes compared to GDEs (Passos et al., 2006; Rajalakshmi & Dhathathreyan, 2007). In this study, only the CCM design will be considered.

A gas diffusion layer (GDL) plays an important role in the MEA by facilitating gas transport, maintaining a balance between water removal and membrane hydration. Product water formed at the cathode is transported via the flow channels to the GDL. If water build-up occurs, flooding can occur which affects the performance of a PEMFC. GDLs are typically made from carbon cloth or carbon fiber paper.

The function of a PEM is to conduct hydrogen ions (protons) and transport them from the anode to the cathode compartment. A membrane should not allow either gas to crossover to the other side of the cell, otherwise undesirable gas crossover will occur. Typical low-temperature PEMFCs use perflurosulfonic acid membranes such as Nafion, which have a multiphase structure: a hydrophobic perflouronated polymer and sulfonic acid groups which acts as a hydrophilic phase. The hydrophobic phase is essential for the mechanical stability of the membrane while the hydrophilic phase carries water and provides high proton conductivity (Kreuer, 1997; Kreuer, 2000). In the presence of water, only the hydrophilic domains are

hydrated. Water is essential for proton conductivity as it promotes the dissociation of protons from the sulfonic acid groups and provides highly mobile hydrated protons. Hydration is the key factor to maintaining optimal performance of the membranes. To keep the membrane hydrated, one or both reactant gas streams are humidified.

2.3. Catalyst layer and the three-phase boundary layer

Typical catalyst layers are sedimentation layers consisting of spherical Pt catalyst on a carbon black support covered by a thin layer of ionomer and separated by pores. A support is used to distribute platinum particles to increase the number of reaction sites per unit catalyst mass. The ionomer is added to increase proton conductivity within the catalyst layer. As shown in Figure 2.4, micropores exist between the clusters of Pt particles and carbon. the primary clusters of Pt/C combine to form a 100 – 300 nm agglomerate. Within these agglomerates are primary pores called mesopores. Agglomerates are surrounded by ionomer film, they combine and form a secondary cluster known as an aggregate, that is ~1 - 3 μm (Soboleva et al., 2010). Secondary pores called macropores exist between agglomerates.

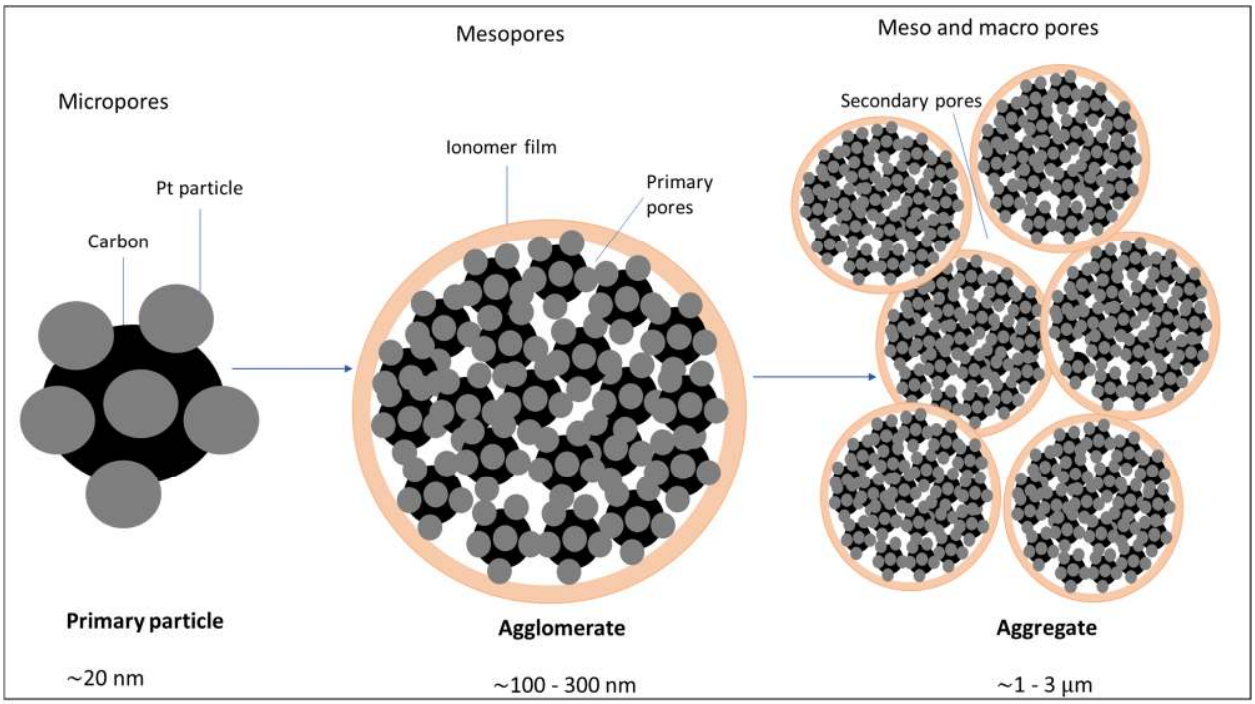

Figure 2.4. Schematic of the representation of CL microstructure of Pt particles on carbon support covered by ionomer film. Adapted from Soboleva et al. (2010).

The catalyst layer needs to be prepared such that a three-phase boundary (TPB) layer is formed. The concept of TPB considers that the HOR and ORR can only occur at confined spatial sites called the 'three-

phase boundary', where the electronically connected catalyst sites, gas, and electrolyte are in contact (O'Hayre et al., 2005). The nature of the TBP is determined by the reaction processes taking place at the catalyst/electrolyte interface and the diffusion process in the void space. In the TBP, carbon acts as an electron conductor to the GDL; the ionomer phase conducts protons and absorbs water; and the gas pores supply reactant gasses and the product liquid water (O'Hayre et al., 2005; Berg et al., 2006). A representative picture of a three-phase boundary layer is shown in Figure 2.5.

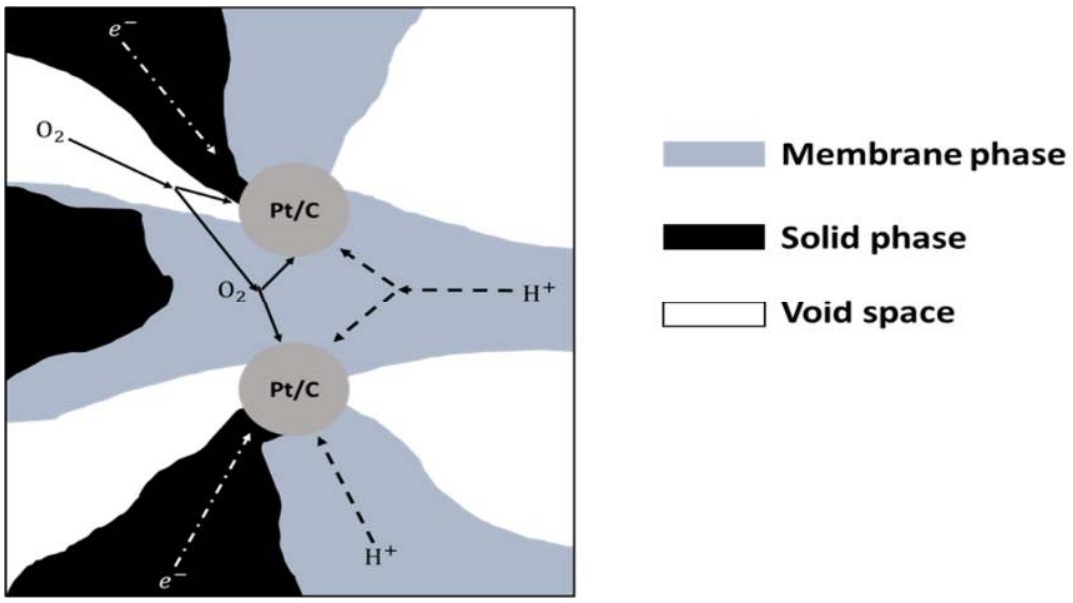

Figure 2.5. A schematic diagram of a three-phase boundary cathode catalyst layer consisting of a carbon/platinum phase (electronic conductor), the ionomer (proton conductor), and gas pores (oxygen supply). Water is present in both the ionomer and pores. Redrawn from Khajeh-Hosseini-Dalasm et al. (2010).

Oxygen supplied to the cathode diffuses in dissolved form through the void spaces and polymer membrane. Hydrogen gas is supplied to the anode side where it diffuses through the GDL void spaces to the GDL/CL interface. At the anode, hydrogen is split into electrons and protons as depicted in Equation (2-1). Electrons travel through the solid phase of the CL and along an external circuit to the cathode CL. The hydrogen ions/ protons migrate to the cathode through the membrane phase, the PEM which separates the anode and cathode. At the cathode, oxygen supplied as air diffuses through the GDL void spaces to the GDL/CL interface. Thus, protons travel through the membrane while oxygen and electrons arrive from the backing layer (GDL). The oxygen is transported in the gas phase, while electrons are transported in the conductive carbon phase and protons in the hydrated ionomer phase. All the reactive species -O, H^+ and e^- reach the reaction sites on Pt carbon clusters (in a TPB) and the ORR takes place at the cathode compartment (2-1).

The importance of the catalyst layer is to (Zamel, 2016):

- Provide a continuous pathway for proton transport
- Transport reactants/ products and effectively remove water from the membrane
- Provide a continuous pathway for electrons between the catalyst and the conductor.
- Provide a high active surface area for the reaction to take place.
- It must also provide a platform for protons, electrons, and gas-phase reactants to be transported effectively and simultaneously through the TPB.

As part of optimization efforts to improve electrode design of an MEA, several catalyst layer properties have to be carefully optimized to achieve high utilization of the catalyst material: reactant diffusivity, ionic and electrical conductivity, and the level of hydrophobicity all have to be carefully balanced. In the most desirable case, the catalyst layer should achieve high current densities using the least amount of Pt catalyst content available in CL. Catalyst utilization in the MEA is controlled by two factors (Yu et al., 2012):

(i) The catalytic activity of the Pt catalyst used, which depends on the electrochemical surface area of the Pt particles and

(ii) Proton transport resistance in the CL, which depends on the proton transport path length and the ionic bond between Pt atoms and ionomer.

2.4. Factors affecting MEA performance

2.4.1. Catalyst activity loss

The maximum amount of electrical energy generated in a fuel cell is equal to Gibbs energy (Larminie & Dicks, 2003). In the reaction (2-3), denoting the difference between the Gibbs free energy of formation of the products and reactants, ΔG_f (expressed in eV), the theoretical potential for one mole of H_2O (ideal voltage) is given by:

$$\mathrm{E} = \frac{-\Delta \mathrm{G_f}}{2\mathrm{F}} \qquad (2\text{-}4)$$

Where F is Faraday's constant. This gives a value for the electromotive force or reversible open-circuit voltage (OCV) of about 1.23 V for an FC operating below 100 °C. However, the voltage of an operating FC is generally less than this value. Voltage losses in an operational FC are caused by several factors. To characterize these losses, voltage is plotted against current density at constant operating conditions to give a polarization curve. This technique is used to characterize the performance losses of fuel cells. A

steady-state polarization curve is obtained by either measuring current as a function of cell potential or by measuring cell potential at different current densities as shown in Figure 2.6 (Wu et al., 2008).

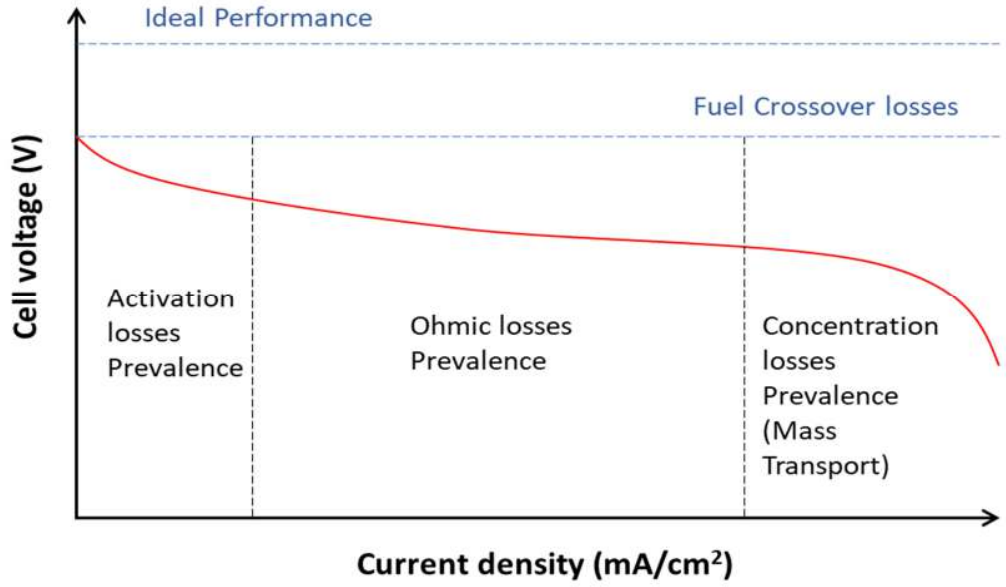

Figure 2.6. Polarization curve illustrating performance losses. Recreated from Jouin et al. (2013).

As seen in Figure 2.6, the open circuit voltage (OCV) is less than the theoretical value of 1,23 V (Zhang et al., 2006). Open circuit voltage is the amount of voltage a cell can produce when no load (current) is demanded. PEMFCs, however, suffer significant activation losses and can only achieve approximately 0.95 V at open circuit conditions and 0.62 V during current generation of 1 A/cm^2. The difference between the OCV and the ideal output voltage is caused by multiple factors, including reactant crossover, contact resistances, etc. (Li et al., 2019). The ORR amounts for 80 % of the total voltage losses in a PEM fuel cell (Inoue & Higuchi, 2009). The highest irreversible voltage losses occur between 0.3-0.5 A/cm^2 current densities, where the anode voltage losses are relatively small compared to the cathode (Marr & Li, 1999).

There are three distinct regions in a polarization curve determined for a fuel cell:

(i) *Activation overpotential*- This part of voltage losses is driven by chemical reactions. To initiate electron transfer from the hydrogen fuel at the anode to the electron acceptor oxygen at the cathode, an energy barrier must be overcome. The energy barrier comprises of activation potential required for the transfer of electrons to the cathode and incurs activation losses due to the slow kinetics of the ORR. The activation losses are observed as a sharp decrease at very low current densities in the polarization curve. The highest activation losses are experienced at the cathode due

to the lower value of exchange current density (Santarelli et al., 2006). The anode and cathode exchange current density are a function of many variables: materials and porosity of the electrode; concentration, distribution, and dimensions of catalyst layer particles; operating temperature. Any of the variables in the CL design can affect the exchange current density and the resulting activation overpotential.

(ii) *The ohmic overpotential*- Ohmic overpotential is linked to electronic and ionic losses (Santarelli et al., 2006). The ionic conductivity is a function of cell temperature and the degree of humidification of the membrane. Ohmic losses increase due to proton charge resistance when the flow of charge is hindered by internal resistance. The potential drop can be expressed by Ohm's law:

$$\Delta V = I \times Ri \qquad (2\text{-}5)$$

Where Ri is the internal resistance, and I is the circuit current. Ohmic losses can be reduced by increasing the proton conductivity of the electrode through minimizing contact resistance between the electrolyte and catalyst and reducing the total travel distance of electrons within the anode.

(iii) *Mass transport or concentration overpotential*- These losses result from the drop in concentration of the reactants at the surface of the electrodes. During the operation of a PEMFC, a stream of the hydrogen gas/ oxygen is delivered to the anode and cathode respectively, where it is consumed. There will be a slight reduction of gases in the region of the electrode as oxygen and hydrogen are being consumed. This will result in the reduction of gas partial pressure, which in turn reduces output voltage. This concentration loss will depend on the current being drawn from the cell, how well gases can circulate, and how quickly oxygen/hydrogen can be replenished. In PEMFCs the slow removal of water/ flooding can also be a cause of mass transport losses or concentration overvoltage as excess water effectively blocks the oxygen supply.

2.4.2. Water management

Water management is one of the critical issues in the design of PEMFCs because membrane hydration determines performance and durability. When the polymer membrane is dehydrated, ionic resistances increase and in extreme cases can lead to irreversible membrane damages such as the formation of pinholes and delamination (Okada, 1999; Knights et al., 2004). The polymer membrane in the MEA must be hydrated to maintain high proton conductivity, and at the same time, excess water must be removed to prevent electrode flooding. During PEM fuel cell operations, two modes of transport of water molecules

occur through the polymer electrolyte membranes as depicted in Figure 2.7: electro-osmotic drag due to a potential gradient and back diffusion due to a concentration gradient of water.

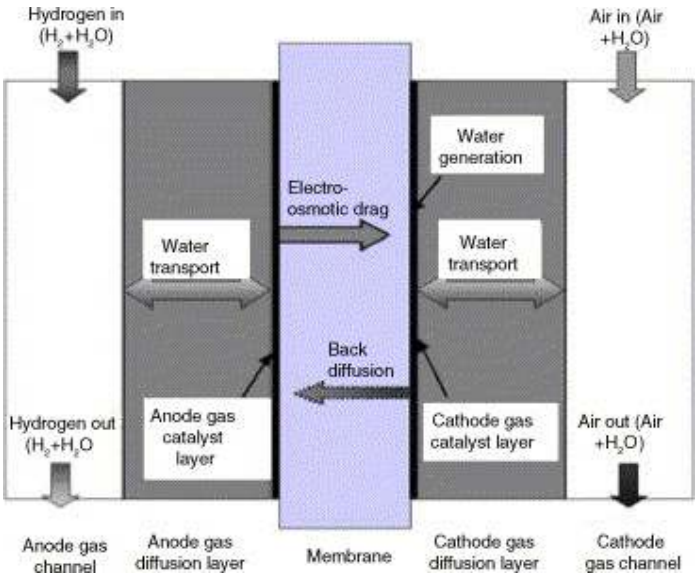

Figure 2.7. Schematic of the transport water mechanism inside a hydrogen PEMFC. Adapted from Yan et al. (2006).

Firstly, water is supplied by an external humidification system to the anode and cathode. When protons move from anode to the cathode by potential difference, they carry several water molecules in the form of hydrated protons. Electro-osmotic drag denotes the flux of water molecules from anode to cathode induced by the migration of protons (Zawodzinski et al., 1995). At the same time, water generation by electrochemical reaction provides additional water at the cathode. When there is a water concentration gradient between the cathode and the anode, back diffusion occurs from cathode to anode. Finally, water is removed at the anode and cathode outlets through bipolar plates. All these processes need to occur simultaneously, and if unbalanced, may result in water management issues. Electrode flooding may occur if proper water removal fails which results in mass diffusion limitations, particularly at the cathode (Nguyen & Knobbe, 2003). Flooding occurs when the rate of production of product water is greater than the water removal rate out of the CL. The water removal rate is a function of MEA structure and the interaction of operating conditions, such as temperature and relative humidity (Pasaogullari & Wang, 2005).

Back diffusion prevails at low current densities while at high electro-osmotic drag prevails at high currents. Accumulation of water in the electrodes must be transported out of the CL or else excess water will block

the pores of the CL and GDL, prevent gases from reaching the active sites as shown in Figure 2.8, leading to gas starvation and an immediate potential drop.

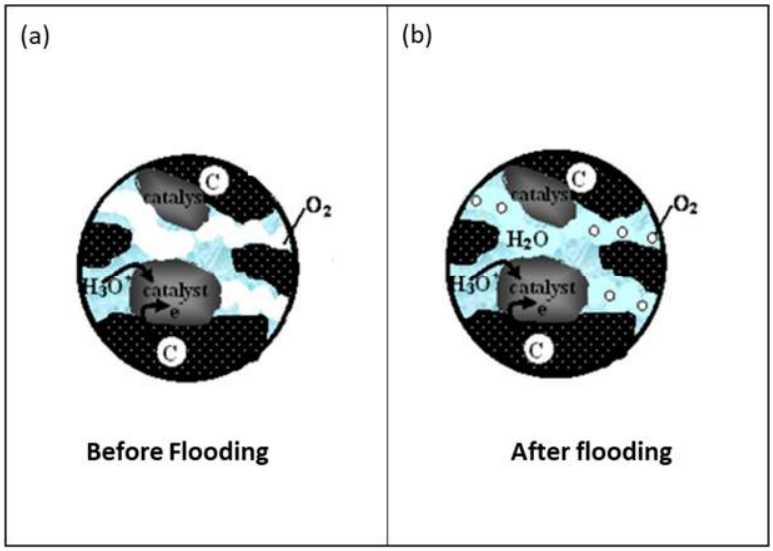

Figure 2.8. A schematic diagram showing how gas diffusion takes place in a CL: (a) before flooding; (b) after flooding. Adapted from Ji & Wei (2009).

2.5. Cathode catalyst layer design for PEMFC

The electrode performance of PEMFCs largely depends on the TPB which should possess important characteristics such as high proton conductivity, high electrochemical conductivity, and high oxygen permeability (Broka & Ekdunge, 1997). To possess efficient transport processes, the electrode should be designed to minimize the polarization losses: activation, ohmic, and mass transport losses. This can be achieved by designing a catalyst layer that can sustain a water balance without sacrificing catalyst utilization, especially on the cathode. In addition to water management, other catalyst layer properties must be optimized to achieve high catalyst utilization. Thepkaew et al. (2008) applied a 2^n full factorial design to identify the key parameters affecting the performance of active layers in PEMFCs and found that the exchange current density or activation losses were controlled by Pt loading whereas the key factors controlling ohmic losses were ionomer content and carbon or support type. In addition to catalyst layer properties, fuel cell performances are affected by operating conditions including partial pressure, temperature, and humidity.

2.5.1. Effect of Pt loading in PEMFC performance

Platinum-based electrocatalysts, the most widely used electrocatalysts in PEMFCs, play an important role in the performance of PEMFCs. They are necessary for the electrochemical oxidation of hydrogen at the anode and the ORR at the cathode. Pt loading at the cathode is generally higher than the anode due to the electrochemical kinetics of the ORR (Wee et al., 2007). High-performance electrocatalysts must improve the slow ORR kinetics at the cathode by reducing the high overpotential (Starz et al., 1999). High catalyst performance is obtained by maximum utilization of the active electrocatalyst sites, which is achieved by a simultaneous contact of the Pt with protons, electrons, and gas reactants. The Pt loading is increased to improve the oxygen diffusivities and to increase the possible TBP area – therefore increasing the amount of fuel consumption. Paganin et al. (1996) investigated the effect of platinum loading on GDEs with a 20 wt.% Pt/C weight ratio. They found that the performance in the cathode improved significantly when the loading was increased from 0.1 to 0.3 mg/cm^2. This was attributed to the effect of an increased active area at higher loadings. However, a decrease in performance was observed when the Pt loading was increased to 0.4 mg/cm^2. No explanation was given for this response, but Litster and McLean (2004) suspect it could be caused by reduced reactant transport to the areas closest to the membrane. Qi and Kaufman (2003) reported the highest performance with a 20 wt.% Pt/C weight ratio and a platinum loading of 0.20±0.05 mg/cm^2 and 0.35±0.05 mg/cm^2 for a 40 wt.% Pt/C weight ratio. A higher Pt loading was required for 40 wt. % Pt/C because of its smaller surface area (72 m^2/g for 40% Pt/C compared to 112 m^2/g for 20%Pt/C).

2.5.2. Determining the optimal ionomer content in a CL

An ionomer is added in the catalyst ink to increase the catalyst utilization- it acts both as a proton conductor and as a binder of electrodes. The ionomer content affects gas permeability, catalytic activity, and ionic resistance (Sasikumar et al., 2004). It retains moisture and prevents membrane dehydration. Increasing the ionomer content increases the water uptake in the CL (Soboleva et al., 2010). Several studies have been performed to determine the effect of ionomer in a CL and to determine the optimal ionomer content. Uchida et al. (1995) studied the effect of perfluorosulfonate ionomer (PFSI) content on cell performance, in dual-layer electrodes consisting of 0.5 mgPt/cm^2 and 25 wt. % Pt/C. The electrolyte was introduced into the electrodes by spreading a catalyst paste constituted of catalyst (Pt/C) and PFSI onto a carbon paper. The increase in PFSI content was found to increase coverage of reaction sites and decreased the volume of secondary pores. As a result, the PFSI content affected fuel cell performance in

the entire current density range and the optimal ionomer content was reported to be 1.0 mg/cm^2. Paganin et al. (1996) performed electrochemical studies on thin-film electrodes with 10 wt.% Pt/C and 0.4 mg_{Pt}/cm^2 loading. It was reported that performance improved significantly when the Nafion loadings were between 1.75 – 2.5 mg/cm^2. This performance improvement was correlated to the electrochemical surface area, membrane resistance, and linear diffusion properties. The catalyst ink was formed by mixing a Pt/C catalyst (10 wt.% Pt/C) and Nafion solution (0.87 – 2.6 mg/cm^2) with isopropanol as a solvent and deposited into the diffusion layer by a brushing technique.

Antolini et al. (1999) investigated the effect of Nafion loading in the CCL of a PEMFC, using half-cell on electrodes consisting of 0 to 1.46 mg/cm^2 Nafion loading. An optimum Nafion content of 0.67 mg/cm^2 was identified. This loading was found to correspond to minimum polarization resistances and oxygen reduction overpotential, and a maximum electrochemical active area. Passalacqua et al. (2001) studied low Pt loading (0.1 mg/cm^2) electrodes with Nafion content ranging from 14 – 66 wt.%. The results showed an optimal ionomer content of 33 wt.%, which is a trade-off between high Pt utilization and minimum mass transport limitations. Qi and Kaufman (2003) designed electrodes for the ORR using different carbon-supported catalysts mixed with Nafion, without adding any solvents. They reported an optimum Nafion content of up to 30 % using a 20 wt% E-TEK Pt/C. A decrease in performance was observed for greater values due to decreased electronic conductivity of the CL at higher Nafion loadings.

Sasikumar et al. (2004) found that ionomer loading depends on Pt loading and its loading requirement increases with a decrease in Pt loading. For electrodes with decreasing Pt loadings of 0.5, 0.25, and 0.1 mg/cm^2, the best performance was obtained with 20 %, 30 %, and 50 % ionomer loadings, respectively. Suzuki et al. (2011) also conducted a study on low Pt loading (0.1 mg_{Pt}/cm^2) CLs with ionomer loading ranging from 14 to 50 % and found an optimal ionomer content of 33 %. Most studies have found high loadings of ionomer to decrease performance due to increased ionic resistances, reduced gas diffusivity, and increased mass transport losses (Sasikumar et al., 2004). Jeon et al. (2010) studied the effect of ionomer content and RH on MEA performance. The study showed that the optimum ionomer content increased with decreasing RH due to a change in oxygen transport rate (flooding) and the number of active sites available (ionic resistances). Kim et al. (2010) examined MEAs with different Nafion loadings and found the highest cell performance at ionomer loadings of 25 wt. % at 59 % RH and 20 wt. % ionomer content at 87 % RH. Increasing RH (59 – 87%) had a positive effect on lower ionomer loading MEAs (20 wt. % and 25 wt. %) because it lowered by their activation overpotential. In contrast, the concentration overpotential of high ionomer MEAs (30 wt.% and 35 wt.%) increased with RH, lowering performance.

Ionomer changes the porosity, permeability, and hydrophobicity of the catalyst layer. It is widely recognized that the ionomer has a great impact on gas diffusion properties- the higher the ionomer loading, the smaller the CL pores for gas transport. Although ionomer is important for proton conduction, it is electronically insulating- it may cause some catalyst particles to be electronically isolated and not take part in any electrochemical reactions (Yoon et al., 2003; Qi & Kaufman, 2003). Therefore, finding the optimal ionomer content is important for achieving the best balance among all these influencing factors.

2.5.3. Effect of relative humidity on PEMFC performance

A well-hydrated membrane is a prerequisite for fast ORR kinetics and higher electrolytic conductivity in a PEMFC. The ionic conductivity in the PEM strongly depends on the degree of humidification. However, when the rate of water removal exceeds the water generation rate, the membrane dehydrates, and this results in poor performance due to larger ohmic losses. Soboleva et al. (2011) studied the role of micropores and mesopores on water sorption and fuel cell activity. They found that at high RH, a cathode catalyst layer with a narrow size distribution, larger pore volume, and low ionomer content is more beneficial due to its low water retention, whereas in dry conditions high ionomer content is crucial. The effect of relative humidity on the electrochemical surface area and charge transfer resistances was also studied by Malevich et al. (2008). The charge transfer resistance increased with decreasing RH whereas the ECSA increased with increasing RH.

This study will evaluate the performance of an MEA as a function of ionomer loading and relative humidity.

2.6. Stratification of cathode catalyst layers

Many studies have researched the CCL to improve the MEA structure and materials distribution in the CL (Yoon et al., 2003; Xie et al., 2005; Wang et al., 2004; Su et al., 2010; Shahgadli et al., 2018). They demonstrated that non-uniform CL structures can increase electrode performance compared to monolayer CLs, using the same catalyst and Pt loadings (Wang et al., 2004; Song et al., 2004; Sun et al., 2005; Srinivasano et al., 2012; Centibas et al., 2015). The concept of a non-uniform multi-layer electrode was proposed by Yoon et al. (2003) to improve oxygen reduction by developing a cathode that has good proton and electron conduction properties. This dual-layer cathode was prepared using a spraying method. Following this concept, several studies have been conducted on multi-layer cathodes for PEMFC and through these studies, it has been observed that fuel cell performance can be significantly influenced

by porosity variation (Roshandel et al., 2005). A summary of studies conducted on multi-layer cathodes for fuel cells has been tabulated in Table 2.2.

Table 2.2. An overview of literature pertaining to stratification methods used for cathode catalyst layers.

Stratification technique	Author(s)	Results
Designed double-layer (two distinct layers) structured cathodes with high (60 wt.%) and low (10 wt.%) Nafion content	Yoon et al., 2003	- The single cells adopting four kinds of double-layered cathodes showed almost the same performance, irrespective of the equivalent weight of Nafion, and Nafion content of the inner and outer layers. They showed a high pressure drop but demonstrated best performance compared to single-layer cathodes
GDEs containing gradient Nafion distribution	Xie et al.,2005	- Cathode performance improved when Nafion content is higher in the GDE towards the CL/ membrane interface and lower towards the CL/carbon paper interface.
GDE with dual-bonded CL consisting of PTFE-bonded Pt/C on a microporous layer with ionomer-bonded Pt/C deposited on it	Zhang and Shi, 2006	- Higher performance than conventional CL - Increased energetic yield from 40%-50%
Designed anode and cathode CLs with gradient Nafion content and varied Pt loading	Kim et al. (2008)	- The dual catalyst layer coated MEA showed higher cell performance at high current density region than the pristine MEA
Proposed electrode composed of a highly phase-separated external layer and a lowly phase-separated inner layer. Inner glycerol-based CL and outer NMP-based CL. Pt loading maintained at 0.2 Lowered Pt loading of the inner and outer layer to 0.16 and 0.04 mg/cm^2	Jung et al., 2014 Jung et al., 2016	- Dual-layer CL increased cell performance in the high-current region - Dual-layer electrode had approximately 4 times larger current density at 0.6 V than single CL MEA
Double-layer cathode with overall Pt loading fixed at 0.4 mg/cm^{2,} and different Pt loading ratios of inner and outer layers.	Kim et al., 2015	- The MEA with an inner layer of 0.3 mg_{Pt}/cm^2 and an outer layer of 0.1 mg_{Pt}/cm^2 exhibited the best performance. This performance

		was better than that of the conventional single-layered electrode by 13.5% at a current density of 1.4 A.cm^{-2}.
A double-layered catalyst cathode electrode for DMFC consisting of Pt/CeO2-C as an inner catalyst and Pt/C as an outer catalyst	Liu et al., 2015	- The double-layered catalyst cathode MEA exhibited a slightly lower maximum power density (87.9mWcm^{-2}), compared to a conventional one (117.4mWcm^{-2}).
Gradient design of Pt/C ratio and Nafion content in PEMFC	Chen et al., 2017	- The power density of the optimal gradient design MEA was 28.4% and 135.7% higher than the conventional single-layer catalyst layer MEA under high and low humidity, respectively.
Used glass epoxy masks to create a patterned electrode with varying thickness on the GDL, that mirrored bipolar plate flow-field channels	Macauley et al., 2017	- Applying more catalyst material in the channels was found to be more beneficial than when applied in the land regions - Reducing ionomer content in the filler improved mass transport, due to less flooding in the CL.
CCL design with various gradients of ionomer distribution	Shahgadli et al., 2018	- This ionomer-gradient design improved Pt utilization by about 15% when compared with the conventional one-layer CCL design; and reduces resistances to both mass and proton transport as well.

2.7. Factors affecting the durability of PEMFCs

Significant progress has been made in PEMFCs on materials, design, manufacturing, and application. However, durability remains a major challenge for large scale commercialization. While the lifetime of PEMFCs used for stationary applications has exceeded 3 years, the automotive MEAs do not meet the required Department of Energy (DOE) standards (Cleghorn et al., 2006). A great number of parameters influence the performance, degradation, and durability of PEMFCs. They can be attributed to operating conditions, cell design and assembly, environmental conditions, and degradation mechanisms (Jouin et al., 2013). MEA degradation results in PEMFC failure. One of the causes of MEA degradation is the degradation of the catalyst in the cathode due to high voltage, low pH, and a highly oxidative environment

(Borup et al., 2007). It has been reported that catalysts supported on carbon black gradually aggregate during long-term cell operation, which reduces the ECSA, leading to irreversible performance losses (Jourdan et al., 2014). Figure 2.9 shows a summary of degradation mechanisms experienced by the electrode during long term operation.

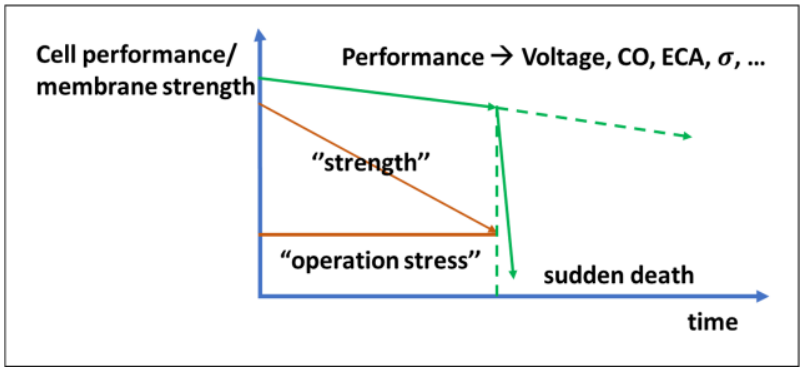

Figure 2.9. Degradation mechanism in PEMFC (CO: Hydrogen crossover, ECA: electrochemical area, and σ: ionic conductivity). Redrawn from Jourdan et al. (2015).

2.7.1. Catalyst agglomeration and dissolution

One of the major challenges hindering large-scale commercialization of PEMFCs is the cathode performance loss during extended operations. Mechanisms that contribute to cathode catalyst degradation have been proposed, including catalyst particle sintering (Wilson et al., 1993), catalyst dissolution, cathode support corrosion (Tang et al., 2006; Shao-Horn et al., 2007), and loss of ionomer/Pt contact (Zhang et al., 2009). Wilson et al. (1993) proposed that the loss of ECSA of carbon-supported platinum in degraded PEMFC is due to platinum sintering, which is caused by Pt migration. Darling and Meyers (2005) modeled the process of Pt dissolution and they showed that Pt dissolution is negligible at low and high potentials but remarkable at intermediate potentials. In their kinetic model, they demonstrated the effect of potential in Pt dissolution in the following 3 equations:

$$Pt \rightarrow Pt^{2+} + 2e^{-} \quad \text{(Pt dissolution)} \quad (2\text{-}6)$$

$$\mathrm{Pt} + \mathrm{H_2O} \rightarrow \mathrm{PtO} + 2\mathrm{H} + 2\mathrm{e}^{-} \quad \text{(Pt oxide film formation)} \quad (2\text{-}7)$$

$$\mathrm{PtO} + 2\mathrm{H} \rightarrow \mathrm{Pt} + \mathrm{H_2O} \quad \text{(chemical dissolution of Pt oxide)} \quad (2\text{-}8)$$

2.7.2. Carbon support degradation

Carbon support corrosion is the major contributing factor of catalyst layer degradation in PEMFCs. Carbon has been widely used as a support material for catalysts in PEMFC because of its high surface area on which fine metals can be deposited (Soboleva et al., 2010). Despite its widespread use as catalyst support, carbon is very susceptible to corrosion. Carbon corrosion is accelerated in environments which are wet, have a low pH (<1), high temperature (50-90 °C), high oxidative potential (0.6 – 1.2 V), and high oxygen concentration (Yu & Ye, 2007). Oxygen atoms are being generated by the catalyst and at elevated temperatures, the oxygen atoms combine with the carbon to form CO and CO_2 which leave the cell. Once a significant amount of carbon is lost as CO and CO_2, the noble metal nanoparticles are lost from the electrode or aggregate to larger particles, reducing catalytic activity, and in extreme cases leading to a structural collapse of the electrode (Yu & Ye, 2007). The CL structure collapses leaving only the unsupported platinum and ionomer. Oxidation of carbon support can also lead to changes in the surface. Furthermore, it has been reported that during the start-up and shutdown of a fuel cell, the cathode potential can reach up to 1.5 V which speeds up carbon corrosion (Yu & Ye, 2007). Figure 2.10 illustrates the carbon degradation mechanism in Pt/C catalyst layers.

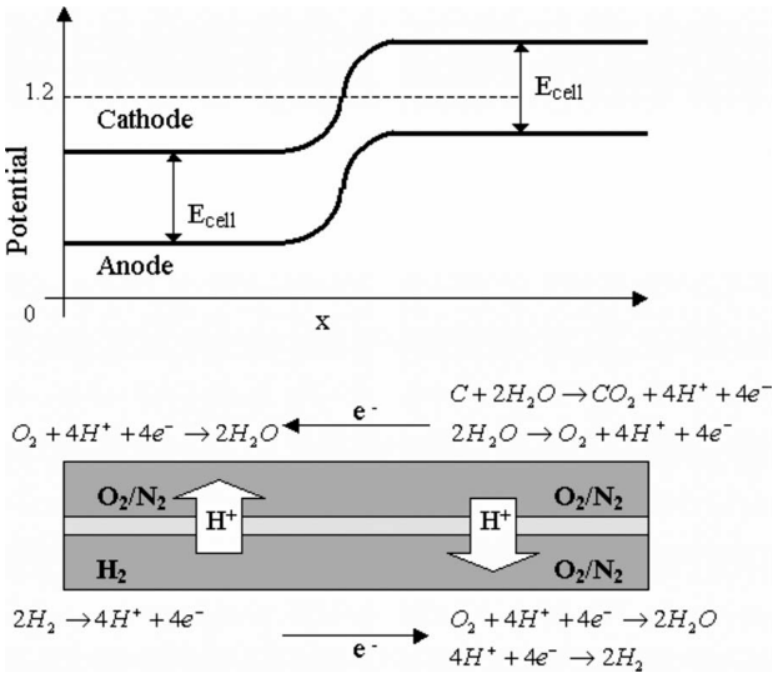

Figure 2.10. The carbon oxidation degradation mechanism. Adapted from Young et al. (2009).

2.7.3. Membrane degradation

Membrane degradation depicts the end-of-life of the cell lifetime as shown in Figure 2.11.

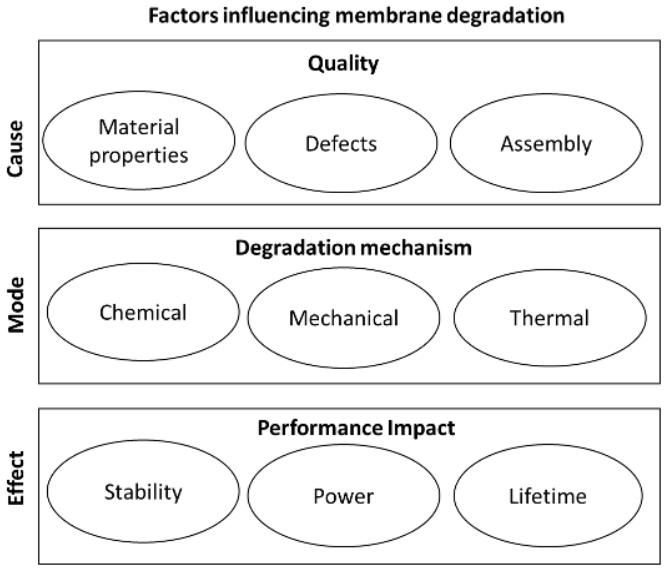

Figure 2.11. Schematic representation of membrane degradation in a fuel cell. Recreated from Kundu et al. (2006).

The three degradation mechanisms that have been identified to affect membrane degradation are:

(i) Chemical degradation- refers to the attack of polymer chains and end-groups, e.g carboxylic end-groups by hydroxyl (HOH) and peroxyl (HOOH) radicals. These radicals are believed to be formed by the decomposition of hydrogen peroxide produced by the ORR and during reactant crossover (Jourdan et al., 2014). Chemical degradation leads to membrane thinning.

(ii) Mechanical degradation- occurs when the membrane experiences creep deformation, cracking, and formation of pinholes. Membrane degradation is usually caused by fabrication defects, improper MEA assembly, and variables in the stacking system such as inhomogeneous compression of bipolar plates, orientation, and compression method (Kundu et al., 2006; Jourdan et al., 2015). Heat also contributes to mechanical degradation by deforming the membrane structure. Nafion's glass transition temperature (ionomer stability) is about 160 ˚C, thereafter it deforms.

(iii) Thermal degradation- caused by a loss of sulfonate groups at temperatures above 200 ˚C. Kreitmeier et al. (2012) proposed that when the hydrogen permeates to the cathode due to membrane defects, it can catalytically combust and produce local heat hotspots. Also, when

the fuel cell operates under fuel/air starvation, the high potentials generated at the anode result in local heat generation and holes in the membrane (Taniguchia et al., 2004).

All three mechanisms result in increased permeation rate which is characterized by an increase in hydrogen crossover.

2.7.4. Ionomer degradation

Dissolution of the ionomer occurs during long-term fuel cell operation, causing separation between the catalyst and ionomer, consequently decreasing ionic conductivity (Xie et al., 2005). Using X-ray photoelectron spectroscopy (XPS), Zhang et al. (2009) also observed that the ionomer in the catalyst layer dissolves and/or decomposes after 300 h of operation. Wood III et al. (2009) used neuron reflectometry (NR) to study the interaction between ideal layers of Nafion on carbon or Pt. they observed that the thickness of Nafion films increased with aging time, which indicated swelling. No studies have been done on ionomer degradation during fuel starvation conditions. A clear summary of all the factors affecting PEMFC degradation is shown in Figure 2.12.

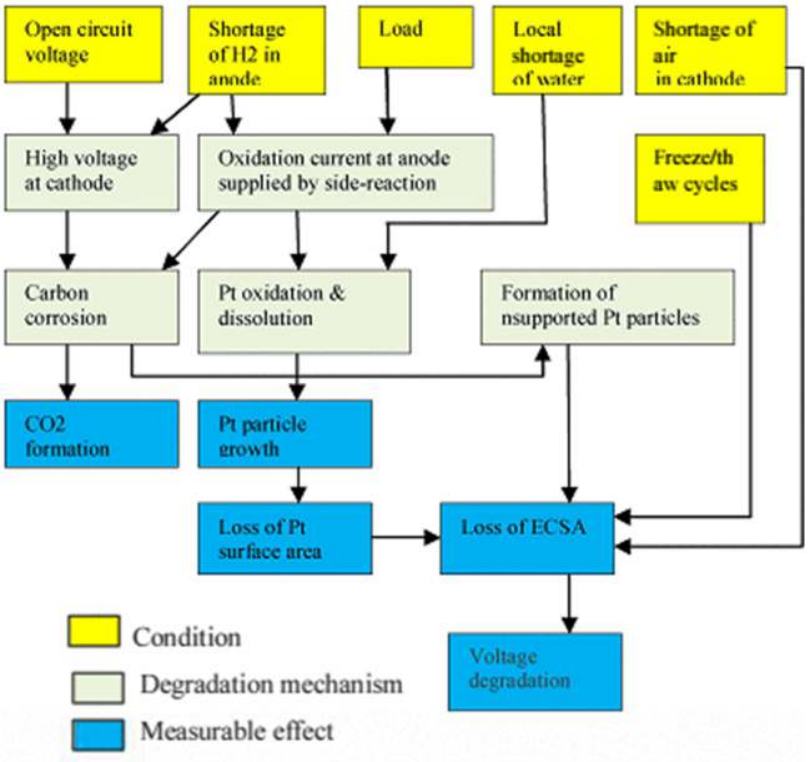

Figure 2.12. A schematic diagram depicting factors that affect the durability of a PEMFC electrode. Adapted from Jourdan et al. (2015).

2.8. Electrochemical techniques relevant for catalyst layer characterization

2.8.1. Polarization curve technique

A polarization curve was used for a comparative assessment of the performance of various MEAs. Herein, the impact exerted by modifications at the level of the materials e.g., incorporating different ionomer contents and reducing Pt loading and be measured and compared. To understand the structure of the properties which result in MEA performance, the polarization curves are correlated with the physio-electrochemical structure of the fuel cell materials. This is achieved using spectroscopy, microscopy as well as independent electrochemical measurements for specific electrocatalytic and transport properties of fuel cell materials. Electrochemical techniques for the latter purpose include cyclic voltammetry and electrochemical Impedance spectroscopy (Eslamibidgoli & Eikerling, 2016). A polarization curve also provides practical information on voltage contributions in the cell, fuel cell failure modes as well as detrimental degradation and inadequate water management.

2.8.2. Cyclic voltammetry

Cyclic voltammetry (CV) is a commonly used electrochemical tool used for fuel cell research, especially to give a detailed description of MEA activity. In-situ CV has proven to be quite valuable for ascertaining the electrochemical surface area (ECSA) in MEAs. In this technique, the potential is cycled between a lower and upper potential limit, while measuring current response in the potential cyclic region. The voltammetry study is performed using a potentiostat/ galvanostat and the cyclic voltammograms are recorded at various sweep rates. The potential is plotted against the measured current and the plot is called a cyclic voltammogram. Figure 2.13 shows a typical cyclic voltammogram obtained for a H_2/Air PEMFC.

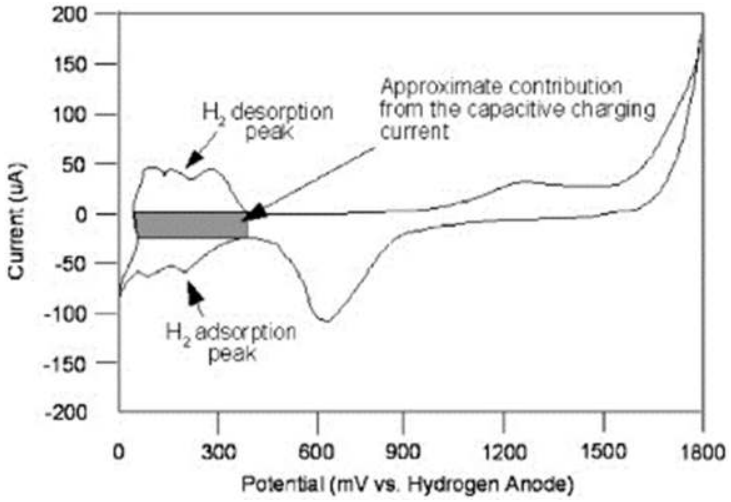

Figure 2.13. A typical CV for a Pt/C electrocatalyst, obtained at 0.5 mv/s sweep rate. Adapted from Wu et al. (2008).

Since the HOR has a negligible overpotential, the anode can act as both the reference electrode and counter-electrode (Zhang, 2008). Before the start of the scan, the working electrode is held at a potential that will not result in an electrochemical reaction. After the scan begins, the potential starts to slowly increase or decrease from a higher/lower potential to a potential high/low enough to cause oxidation/reduction. Oxidation occurs on the forward sweep which results in a positive (cathodic) current and reduction occurs on the backward sweep leading to a negative (anodic) current. The two peaks identified in Figure 2.13 correspond to the Hydrogen adsorption and Hydrogen desorption peaks on the Pt surface. The ECSA can be determined by integrating the hydrogen adsorption peak area.

2.8.3. Electrochemical Impedance Spectroscopy

The resistance of the cell is often a complex function of many parameters e.g., temperature, current density, hydration, etc. The four methods generally used for measuring internal cell resistances in single cells are current interrupt (iR), AC resistance, electrochemical impedance spectroscopy (EIS), and high-frequency resistance (HFR). In this study, the EIS technique will be used to evaluate the internal resistances of single MEAs. EIS applies a small ac voltage or current perturbation/signal (of known amplitude and frequency) to the cell, and the amplitude and phase of the resulting signal are measured as a function of frequency. The resulting EIS spectrum is shown in Figure 2.14 (b).

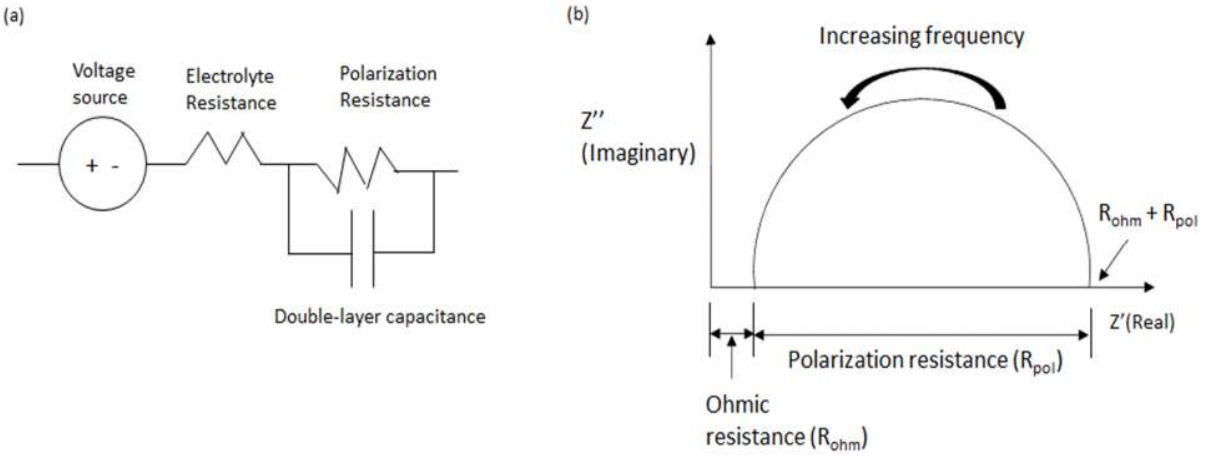

Figure 2.14. (a) Simplified Randles equivalent circuit for a H_2/Air PEMFC; (b) Nyquist plot of the impedance of the equivalent circuit shown in (a). Redrawn from Cooper & Smith (2006).

The fuel cell can be modeled by the Randles equivalent circuit shown in Figure 2.14 (a). By performing a complex capacitance analysis using the Randles equivalent circuit model, the interfacial capacitances, and ionic resistances of PEMFC MEAs can be experimentally obtained at various relative humidity conditions.

The polarization resistance of the cathode is much larger than the anode and is therefore considered in circuit elements. Polarization resistance is the reaction resistance equivalent, double-layer capacitance is the interfacial capacitance of the cathode, and the ohmic resistance is the resistive component of the fuel cell (Cooper & Smith, 2006). The voltage source element is an ideal direct current voltage source (zero internal impedance and constant voltage) with a potential equal to the open circuit voltage of the fuel cell. At high frequencies, only the bulk ionic and electronic ohmic resistance and contact resistances are observed. The magnitude of these resistances is determined by the high frequency intercept with Z'(Real). Factors contributing to the ohmic resistance include membrane resistance; GDL, bipolar plate, and contact resistances; bulk electronic and ionic resistance. At intermediate frequencies, charge transfer resistances dominate and can be determined by the diameter of the arc. Charge transfer is dependent on the interfacial reaction kinetics, a consequence of the three-phase reaction zone. At low frequencies, mass transport limitations are dominant. These are due to mass transport resistance in the GDL, catalyst layer, and the membrane (Gomadam & Weidner, 2005; Wu et al., 2008; Jang et al., 2009).

2.8.4. Carbon corrosion accelerated stress test

Carbon corrosion plays a major part in PEMFC performance degradation. Several Accelerated Stress Tests (ASTs) for PEMFC components (e.g., electrocatalyst, catalyst support, membrane) have been developed

by the U.S. Department of Energy (DOE), the U.S. DRIVE Fuel Cell Tech Team (FCTT), and the Japan Automobile Research Institute (JARI) to evaluate the durability of materials (Garland et al., 2007). Primarily, two types of carbon corrosion ASTs that been recommended by the U.S. DRIVE FCTT: 1.2 V cathode potential hold and cycling from 1–1.5 V at 500 mV/sec (Garland et al., 2007). The carbon lost at potentials greater than 1.2 V_{RHE} reduces the ECSA and kinetic performance and weakens the CL structure. Using CV, the ECSA degradation during potential cycling is evaluated. Figure 2.15 shows a schematic of a Pt/C agglomerate before and after the AST test.

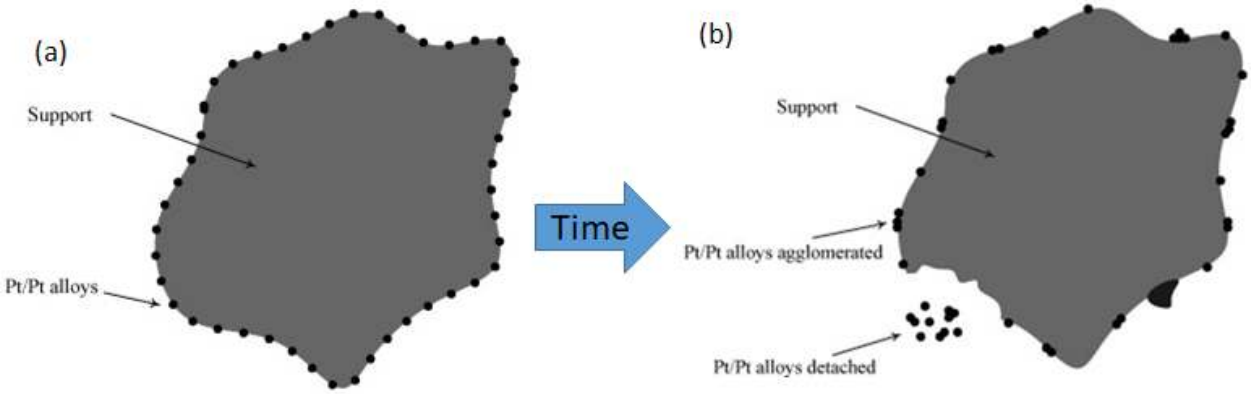

Figure 2.15. Schematic representation showing Pt supported on carbon support agglomerate (a) before and (b) after carbon degradation.

2.9. Physical characterization techniques

To understand the performance characteristics of an MEA it is important to understand its physical characteristics. The quality and utility of solid-phase materials are mostly affected by the surface area and porosity. Any changes in these physical properties can significantly affect MEA performance. The performance of a porous material is often measured in terms of the internal surface area per unit weight or volume, which is conventionally characterized by gas-adsorption (Tian & Wu, 2018). The Brunauer-Emmett-Teller method and Scanning electron microscopy analysis were used as physical characterization techniques.

2.9.1. Brunauer-Emmett-Teller (BET)

The Brunauer, Emmett, and Teller (BET) technique is the most popular method used for determining the surface area of powders and porous materials (Sing, 2015). This method is based on the adsorption of gas onto the investigated solid surface. The BET theory uses probing inert gases as adsorbates to quantify the

surface area. Nitrogen is the commonly employed gaseous adsorbate or probe molecule (Sing, 2001). The surface area is measured by exposing nitrogen to the surface of the solid and by calculating the amount of adsorbate gas corresponding to the monomolecular layer on the surface. Physical adsorption results from van der Waals forces between the adsorbate gas and the solid surface area (Thommes, et al., 2015).

2.9.2. Scanning Electron Microscope (SEM) Analysis

A scanning electron microscope (SEM) produces images by scanning the surface of the studied material with a beam of finely focused electrons (Nanakoudis, 2019). Electrons interact with the atoms in the sample to produce various signals that give information about the topography of the sample surface as well as the composition of the sample.

CHAPTER 3

3. EXPERIMENTAL PROCEDURE

The experimental procedure describes the preparation method of the MEAs as well as the electrochemical and physical characterization techniques used to study the MEAs.

3.1. MEA fabrication

The chemicals used in the formulation of the ink which is sprayed to manufacture the MEAs are listed in Table 3.1.

Table 3.1. Chemicals, catalysts, and gases in MEA ink preparation, physical & electrochemical characterization.

Chemical formula	Chemical name	Supplier	Purity grade (%)
C_3H_7OH	Iso-Propanol	Kimix	99.9
-	Aquivion	Solvay	26 wt.% solids
-	Hysa-K40	Mintek	40 wt.% Pt
H_2	Hydrogen	Syngas	99.999
N_2	Nitrogen	Air products	99.999
-	Synthetic air	Air products	--
H_2O	Deionized water		18.2 µm/cm^2

The catalyst ink was prepared by dispersing HySA-K40 platinum on carbon (Pt/C) in 99.9 % iso-propanol, de-ionized water with 26 wt.% solids Aquivion solution, under magnetic stirring. The ink slurry was then high shear stirred into a finer homogeneous solution. The catalyst slurry was coated on a 50 cm^2 M820.15 gore membrane using the ultrasonic spray method. The CCM was coated at a constant speed under vacuum until a target platinum loading of 0.4 mg_{Pt}/cm^2 for the cathode and 0.1 mg_{Pt}/cm^2 anode was achieved.

After coating, the CCM was gasketed using a 43 µm commercial gasketing material. The importance of gasketing is to provide sealing between the active area and the GDLs to prevent gases from leaking when the CCM is under compression. The gasketed CCM was hot-pressed at 90°C, 10 000 kPa for 1 min using a hot-pressing machine to ensure complete sealing. The gasketed CCM was sandwiched between two

double-layer commercially available gas diffusion layer (GDL) material (Avcarb MB30) to form an MEA shown in Figure 3.1.

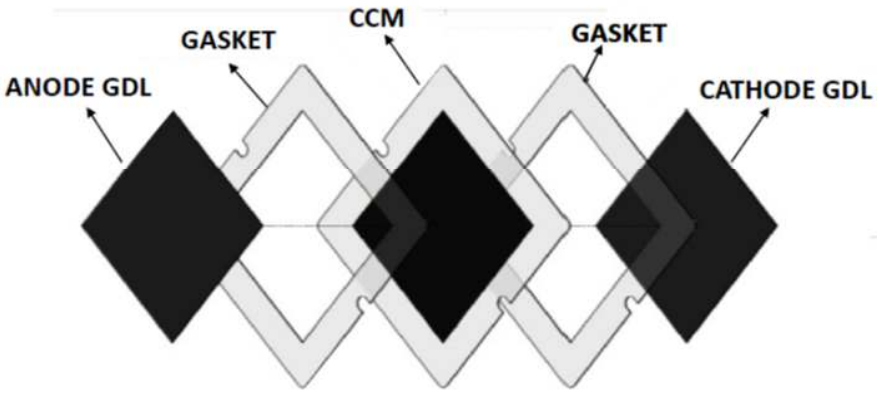

Figure 3.1. Illustration of a membrane electrode assembly. Catalyst is coated onto an M820.15 gore membrane making a 50 cm^2 active area.

Various ionomer loading MEAs were produced to determine the optimal ionomer concentration as shown in Table 3.2 below.

Table 3.2. A summary of the MEAs manufactured with increasing ionomer compositions.

MEA No.	Ionomer Content (wt.%)		Pt loading ($mgPt/cm^2$)	
	Inner layer	Outer layer	Anode	Cathode
MEA #1	20	0	0.1	0.4
MEA #2	24	0	0.1	0.4
MEA #3	28	0	0.1	0.4
MEA #4	32	0	0.1	0.4
MEA #5	35	0	0.1	0.4
MEA #12	24	0	0.1	0.35

3.1.1. Preparation of a stratified CCL MEA design

For a stratified CCL design, two catalyst inks containing varying ionomer contents were prepared. The first ink slurry containing a higher ionomer content (28 wt.% I) was sprayed onto the cathode of the membrane

to form the first layer until a targeted Pt loading was reached. The second ink mixture was then deposited onto the first layer of catalyst to form the outer layer. As shown in Table 3.3, the total platinum loading was fixed at 0.4 mg_{Pt}/cm^2 and 0.1 mg_{Pt}/cm^2 for the cathode and anode respectively (MEA #6 & #7). Thereafter the cathode Pt loading was reduced by 0.05 mg_{Pt}/cm^2, while maintaining the anode Pt loading at 0.1 mg_{Pt}/cm^2, to achieve a total MEA PGM loading of 0.35 mg_{Pt}/cm^2, (MEA#8- #10).

Table 3.3: Stratified CCL MEA designs

	Cathode Pt loading (mg_{Pt}/cm^2)		**Overall Cathode PGM loading (mg_{Pt}/cm^2)**	**Ionomer Content (wt.%)**	
	Inner layer	Outer layer		Inner layer	Outer layer
MEA #6	0.10	0.30	0.40	28	24
MEA #7	0.20	0.20	0.40	28	24
MEA #8	0.05	0.30	0.35	28	24
MEA #9	0.10	0.25	0.35	28	24
MEA #10	0.15	0.20	0.35	28	24
MEA #11	0.20	0.15	0.35	28	24

3.2. Electrochemical characterization

The MEA was placed in a fuel cell hardware consisting of two graphite bipolar plates with parallel flow field channels, two copper current collectors, and two end plates for the anode and cathode respectively (Figure 3.2). The assembly was compressed to a torque of 5 N.m.

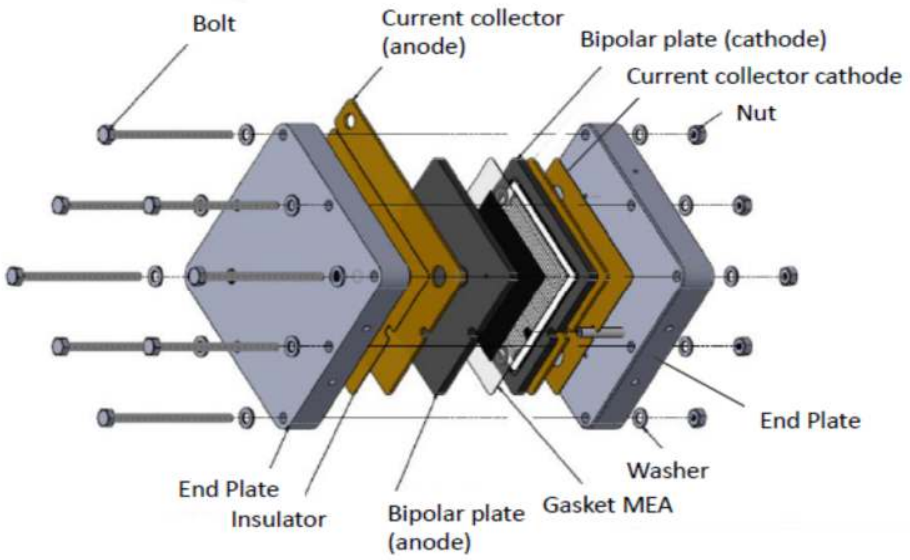

Figure 3.2. MEA components in a low-temperature fuel cell.

All single-cell tests were conducted with a fully automated FuelCon fuel cell test station. The station has a reactant feeding system, mass flow controllers to control the flow of reactants through the system, a thermocouple inserted into the test cell to measure the temperature, and a cooling fan to cool down the cell. Figure 3.3 shows the overall scheme of the fuel cell system used.

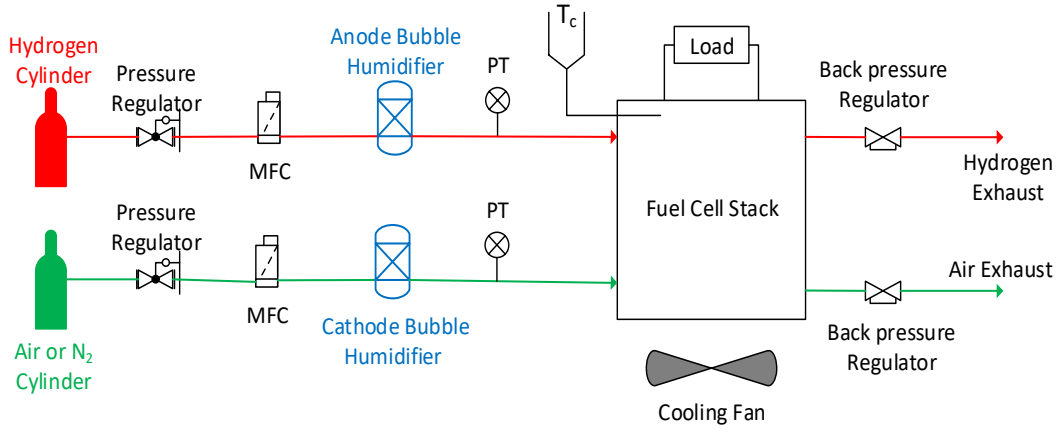

Figure 3.3. An overall scheme of a fuel cell system used for in-situ electrochemical characterization. Redrawn from Migliardini & Corbo (2013).

Pure hydrogen was used as fuel and air as an oxidant for the anode and cathode compartments, respectively. The MEA was conditioned before polarization measurements: the cell was heated up to 80

°C at 100 % RH, with hydrogen and air flow in the potential range between 0.3 V and 1 V with 0.05 V steps. Pure H_2 gas was supplied at 1.11 Nl/min to the anode and Air at 2.65 Nl/min to the cathode compartment. The conditioning cycle was repeated 12 times for a 2-hr period. The single-cell was activated at 0.3 V using hydrogen and air at 80 % relative humidity (RH), 74.6 °C operating temperature and 2 bar back pressure for both anode and cathode. The stoichiometric ratios for H_2 and air were 1.5 and 2.0, respectively.

All MEAs (stratified and non-stratified) were tested in the humidity range 20 - 100 % RH, starting from dry conditions (20% RH) and moving to more humidified conditions:

- 20 % RH- anode and cathode bubblers humidified at 45 °C
- 60 % RH- gases humidified at 67.5 °C
- 100% RH- gases were humified at 80 °C

3.2.1. Polarization curve measurements

Polarization measurements were conducted periodically at all humidity conditions to determine MEA performance. The polarization is split into two regions, the low-density region and the high-density region, allowing smaller steps to be taken in the low-load densities and larger steps to be taken in the higher load density region. Constant current was maintained while the output voltage was recorded as an average of 3 measurements taken within a 3 min period after 1 minute of stabilization. In the low-load density region, the current was increased from 4 mA/cm^2 by a step of 1 until it reaches the final low load density (100 mA/cm^2). In the higher-load density region, current was increased by increments of 5 until the final load density was reached (1600 mA/cm^2). I-V curves were recorded from dry to fully humidified conditions (20 % RH- 100 % RH). The operating temperature was 74.6 °C, and back pressure was 2 bar for both anode and cathode. The stoichiometric ratios for H_2 and air were 1.5 and 2.0, respectively.

3.2.2. Cyclic Voltammetry (CV)

Cyclic voltammetry was used to characterize the electrochemically active surface area (ECSA) and double layer capacitance (CDL) of the CLs in the 20 – 100% RH range. Before measuring the CV, the cell was conditioned using evaporation-condensation cycles: the cell was heated up to 80 °C at 100% RH. N_2 was purged through the cell for 30 mins to remove all oxygen.

The cell was then cooled to ~ 45.6 °C for another hour, while gases were kept at 80 °C to allow sufficient water condensation in the CL. The bubblers were heated to establish the required humidity and the cell was then set to 80 °C. The CV was performed using a Potentiostat with the anode employed as a reference

electrode. H_2 was purged through the cell for 2 mins: gas flow rates of 0.5 Nl/min on the anode and 0 Nl/min cathode. Thereafter, pure hydrogen flowed through the anode at 0.5 Nl/min, while the cathode, the working electrode, was fed with nitrogen at 30 Nl/min. The electrode potential was scanned between 0.04 and 0.09 V with a scan rate of 50 mv/s; a potential step from 0.04 to 0.4 V with a potential hold (double layer region) at 0.4 V for a period of 120 s and then scanned from 0.04 to 0.9 V. The current limit was set to 10 A/cm^2. Data was collected over 2 mins at 200 ms intervals. The cycle was repeated 5 times until no change in the CV shape was observed. The 5th CV cycle was used for data analysis.

H_2 adsorption and desorption currents on Pt were measured in the H_2/N_2 atmosphere to avoid the contribution from faradaic reactions at 1atm (abs).

During reduction, hydrogen ions stick to the surface (adsorb) of the metal due to electrostatic attraction with the surface of an electrode (Monk, 2001). During oxidation, these hydrogen ions leave (desorb) the surface of the electrode according to the following electrochemical reaction (Anon., 2005):

$$\mathrm{H_{ads} \rightarrow H^+ + e^-} \qquad (3\text{-}1)$$

Figure 3.4 shows an image of a typical CV obtained for a Pt electrode in an electrolytic cell.

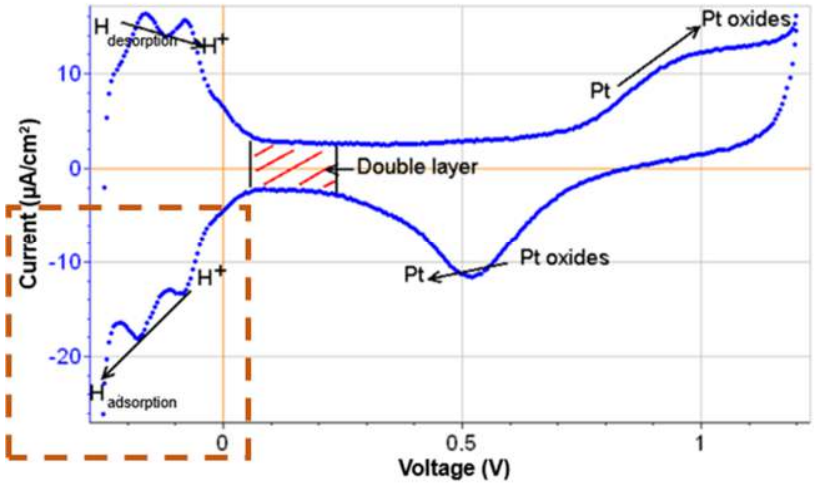

Figure 3.4. Current vs. Voltage curve obtained by cyclic voltammetry. Adapted from Calculation of the platinum's active surface (2005).

The measure of the number of electrons released during the oxidation of platinum at low potentials is equivalent to the number of hydrogen atoms desorbed from the electrode surface. Thus, evaluates

the number of adsorption sites present on the electrode's surface. This defines the active surface of the electrode. The ECSA can then be determined using the following equation (Wu et al., 2008):

$$\mathrm{ECSA} = \frac{\mathrm{Q\ (\mu C/cm^2)}}{\mathrm{210\ (\mu C/cm^2 Pt)\ x\ Pt\ loading\ (gPt/cm^2)}} \qquad (3\text{-}2)$$

Where 210 $\mu C/cm^2 Pt$ is the average current density of Pt atoms in Pt (100), Pt (110), and Pt (111) crystallite faces, and Q is the total charge of ions.

The total charge of ions, Q, corresponding to the hydrogen adsorption can be calculated through the integration of the hydrogen adsorption area. The area of the curve is presented in Figure 3.5.

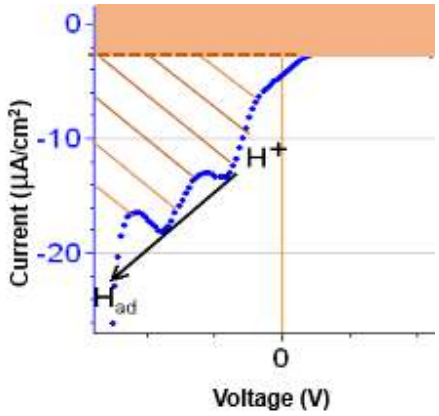

Figure 3.5. A close-up image of the hydrogen adsorption area presented in Figure 3.4. The orange lines represent the area of hydrogen adsorption, the solid block corresponds to the capacitive current (double layer capacitance).

The total charge, Q, can be calculated using the following equation (Anon., 2005):

$$Q = \int_{t1}^{t2} Id\tau = \frac{1}{v_b}\int_{E1}^{E2} IdE \qquad (3\text{-}3)$$

Where V_b is the scan rate, I is the current, and E is the electrode potential. The integral was calculated using the integration tool on Excel. To avoid overestimating the total charge density attributed to the electrocatalytic activity of the Pt surface, the area due to double layer charging and the hydrogen crossover currents are subtracted from the area of hydrogen adsorption. The validity of the method implies that the point where hydrogen adsorption is complete can be exactly identified and that the coverage is completed before the rate of hydrogen evolution becomes significant (Li & Lane, 2011).

3.2.3. Hydrogen cross-over current

Hydrogen cross over was measured using linear sweep voltammetry. The linear sweep voltammetry is like CV, but only performs a forward or a backward scan. Humidified gases, H_2 and N_2 were supplied at the anode and cathode respectively and H_2 current densities were measured at a scan rate of 50 mV/s and a step potential step of 1 mV in the potential range of 0-1 V.

3.2.4. Electrochemical Impedance Spectroscopy

EIS was used to evaluate the ohmic and charge transfer resistance of a single MEAs. The in-situ EIS was obtained using Fuelcon True Data EIS. The True Data EIS carried out alternative current (AC) impedance measurements. The frequency sweep was performed from 20 kHz to 0.1 Hz at 0.1 mA/cm^2 and 0.5 mA/cm^2. The sweeps were performed 3 times at each current density for reproducibility. Oxygen fed as air was used at the cathode (working electrode) and hydrogen at the anode (counter/reference electrode).

3.2.5. Carbon corrosion test

A carbon corrosion test was run to study the rate of MEA degradation. The cell was first conditioned at the standard conditions listed in Table 3.4.

Table 3.4. Operating conditions for the standard fuel cell operation and carbon corrosion test

	Cell Temperature	**Gas flow rates**	**Feed gas temperature**	**Back pressures (bar)**	**RH (%)**
Standard conditions	80℃	1.11 Nl/min H_2 (anode) 2.65 Nl/min air (cathode)	50℃ anode (H_2) 50℃ cathode (air)	2	100 (anode) 80 (cathode)
Carbon corrosion test conditions	80℃	0.2 Nl/min H_2 (anode) 30 Nl/h N_2 (cathode)	83℃ anode (H_2) 83℃ cathode (N_2)	1	100 (anode) 100 (cathode)

During the carbon corrosion test, carbon and water oxidation are incurred by cycling voltage across the MEA. The potential was cycled repeatedly between 0 and 1.2 V at 50 mv/s. The process was repeated for

up to 6000 cycles. The experimental cycles were divided into the following segments: beginning of life cycle, 20 cycles, 180 cycles, 200 cycles, 600 cycles, 1000 cycles, 2000 cycles, and 6000 cycles. Polarization curve, hydrogen crossover and CV were 160 measured in each segment.

3.3. Physical characterization

3.3.1. Scanning Electron Microscope (SEM) Analysis

Scanning electron microscopy (SEM) was conducted to investigate the structural changes of the catalyst layers after the 48-h carbon corrosion test. SEM was performed at the University of Cape Town Electron Microscope Unit using an FEI Nova NanoSEM 230. The SEM images were taken using a backscatter detector at 2000, 5000 & 10 000 x magnification, and 20.0 keV.

3.3.2. Brunauer-Emmett-Teller (BET) surface area analysis

BET was used to determine the surface area, pore size, and cumulative pore volume of the CLs. During BET analysis, the sample was cooled to liquid nitrogen temperature, followed by physical absorption (based on van der Waals interactions) of N_2 molecules from a known amount of gas onto the surface of the sample. The surface area was measured by exposing nitrogen to the surface of the solid and by calculating the amount of adsorbate gas corresponding to the monomolecular layer on the surface.

CHAPTER 4

4. Ionomer Optimization Study

This chapter presents the results and discussion for the optimization of the ionomer content in the membrane electrode assembly (MEA) with a uniform Pt loading of 0.4 mg/cm^2 on the cathode and 0.1 mg/cm^2 on the anode. The MEA performance, electrochemical surface area (ECSA), and Electrochemical Impedance (EIS) were determined and compared at a high and low relative humidity (RH).

4.1. Effect of ionomer content on CL surface area

BET analysis was performed to determine the surface area and cumulative pore volume of the different ionomer loaded MEAs. Before conducting the BET analysis, the average thicknesses of the MEAs were measured using a thickness gauge to determine the volume and bulk density of the samples. Table 4.1 shows the average thicknesses of the various ionomer loaded MEAs.

Table 4.1. Average thickness of the MEAs with varying ionomer weight.

Electrodes	Ionomer content (wt.%)	Thickness (mm)
MEA #1	20	0.0514
MEA #2	24	0.0518
MEA #3	28	0.0524
MEA #4	32	0.0540
MEA #5	35	0.0624

The thickness of the MEA increased with increasing ionomer content. Ionomer forms a thick skin layer around Pt/C aggregates to form Pt/C-ionomer agglomerates. Increasing ionomer content increases ionomer coverage around the Pt/C aggregates, thus increasing the Pt/C-ionomer agglomerate size (Shukla et al., 2015). A schematic diagram showing the effect of ionomer content on the CL is shown in Figure 4.1.

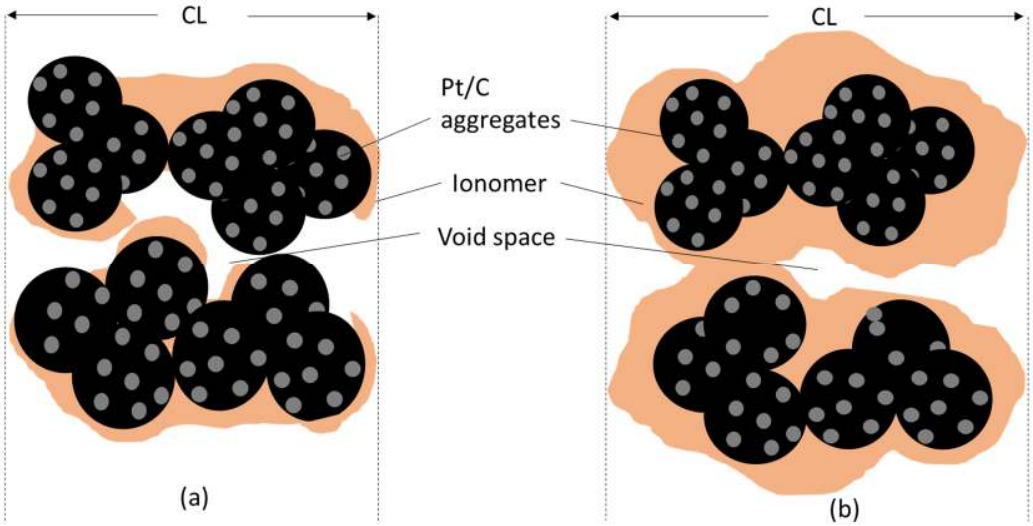

Figure 4.1. A schematic diagram showing the effect of ionomer on CL thickness and microstructure: (a) Lower ionomer loading CL; (b) high ionomer loading CL. When the I/C ratio was changed: agglomerate size and CL thickness increased with ionomer loading (Modified from Shukla et al., 2015).

The ionomer/supported catalyst ratio was changed by increasing ionomer content while keeping the Pt loading constant. A consequent increase in CL thickness was observed. The BET results are shown in Table 2. The dry Pt/C catalyst has a high surface area of 356,2 m^2/g. After the catalyst/ionomer ink was coated and dried in the MEAs, the surface area was reduced 5-fold. The surface area is reduced significantly due to coverage of the Pt by ionomer.

Table 4.2. The BET surface area, cumulative pore volume and porosity of the MEAs loaded with ionomer ranging from 20 wt% to 35wt. % I.

Electrodes	Bulk density (g/cm^3)	Cumulative pore Volume (cm^3/g)	BET surface area (m^2/g)	Total porosity (%)
MEA #1	0.7529	0.1653	91.50	12.44
MEA #2	0.8157	0.1443	70.18	11.78
MEA #3	0.8379	0.1851	65.16	15.51
MEA #4	0.7917	0.05876	72.56	4.520
MEA #5	0.7332	0.1686	60.23	12.36
K40			356.2	

The density of the CLs increased with ionomer addition up to 28 wt.% I (MEA #3). Thereafter, a further increase in ionomer loading resulted in a less dense CL, with the highest ionomer loading MEA (MEA #5) being the least dense. MEA #5 had the lowest BET surface area likely due to larger agglomerates and higher ionomer coverage of the Pt/C particles. Bigger particles have a low surface area and pack together less densely (Ghassemi & Pak, 2011), while smaller particles have a high surface area and can be compacted together more densely. Pores inside the agglomerate (primary pores) can be blocked by the ionomer as its loading increases, assuming that the ionomer is mainly distributed to the agglomerate surface (Hannach et al., 2011; Hannach et al., 2014). This suggests that the BET surface area generally decreased with increasing ionomer content due to an increase in agglomerate size.

The cumulative pore volume and porosity of the CL varied with ionomer addition. There is less than 4% difference in porosity between 20-28 wt.% I loaded MEAs (MEA #1-3). A significant reduction in cumulative volume and porosity was observed with 32 wt.% I loading (MEA #4) due to increased ionomer thickness in the CL. A study by Soboleva et al. (2010) found that the ionomer coverage for Ketjen black carbon supports increases with ionomer content until 30 wt.%. A further increase in ionomer content increases ionomer thickness rather than ionomer coverage, decreasing void spaces between agglomerates. However, at 35 wt.%I loading (MEA #5), the cumulative pore volume and porosity of the CL were similar to that of 20 wt.% I (MEA #1). The excessive ionomer addition possibly resulted in the formation of ionomer agglomerates and reduced coverage of Pt/C particles as reported by Andersen & Grahl-Madsen (2016). The extent of ionomer agglomerate did not form part of the current study but is suggested for future investigation.

4.2. Effect of ionomer content on the electrochemical surface area (ECSA)

The ECSA was determined by integration of the hydrogen adsorption peak area in the determined CV profile after correction for hydrogen crossover. Figure 4.2 compares the ECSAs of different ionomer loading MEAs (MEA #1- #5), under various RH conditions.

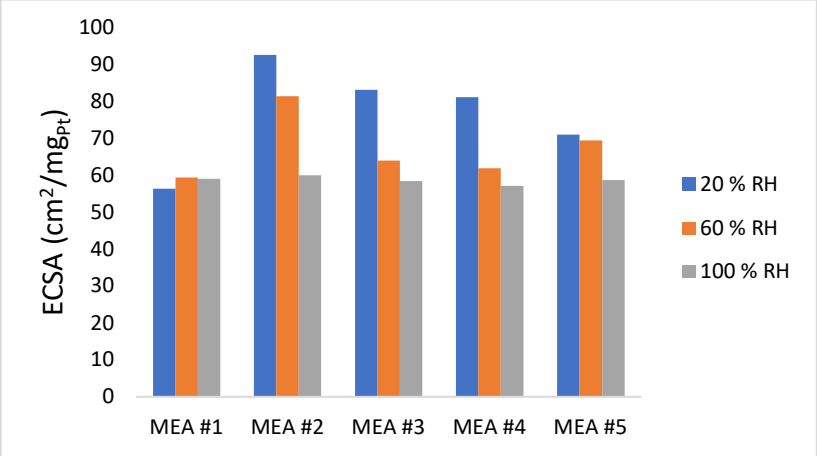

Figure 4.2. ECSA for MEA #1 to MEA #5 with increasing ionomer content (20 -35 wt.%) determined with cyclic voltammetry.

The ECSA decreased as the RH was increased to fully humidified conditions, except for MEA #1. This decreasing trend is in accord with the findings of Song et al., (2007) and Xu et al., (2005) who attributed this change in ECSA to water in the reaction zone which covered active sites, impacting on ORR pathways. MEA #1 ECSA was relatively independent of the RH. In low ionomer loading MEA (MEA #1), ionomer coverage around Pt/C aggregates is likely insufficient and electrocatalyst sites are therefore ionically isolated. These sites are therefore so isolated from proton transportable ionomer that they cannot contribute to the ECSA (Wei et al., 2005; Shukla et al., 2015) even at 100% RH.

The ECSA increased for a 24 wt.% I MEA (MEA #2), which indicates an increase of the triple-phase boundary (TPB) layer and the connection of ionic channels at the CL surface (Lee, et al., 1998). Increasing ionomer content in the CL results in an extension of the triple-phase reaction zone and a consequent decrease in charge transfer and ionic resistances (Lee, et al., 1998). For 20 % RH, the ECSA decreased as the ionomer increased due to the coverage of active sites by the ionomer (Zhao et al., 2010; Seo et al., 2010); Martin et al., 2010; Passalacqua et al., 2001). For 100 % RH, the ECSAs were low and relatively independent of ionomer loading. At fully humidified conditions, the secondary pores (pores between agglomerates) are blocked with water and gas cannot fully access active sites.

4.3. Analysis of MEA Performance

Polarization curves show the performance and characterize voltage losses of an MEA in a single test cell. Polarization curves presented in Figure 4.3 shows the relationship between the output voltage and the current density of a single cell. In this study, polarization curve measurements were determined for

different ionomer loaded MEAs for increasing RH. The RH of the anode and cathode feed gases was increased from 20-100 %RH.

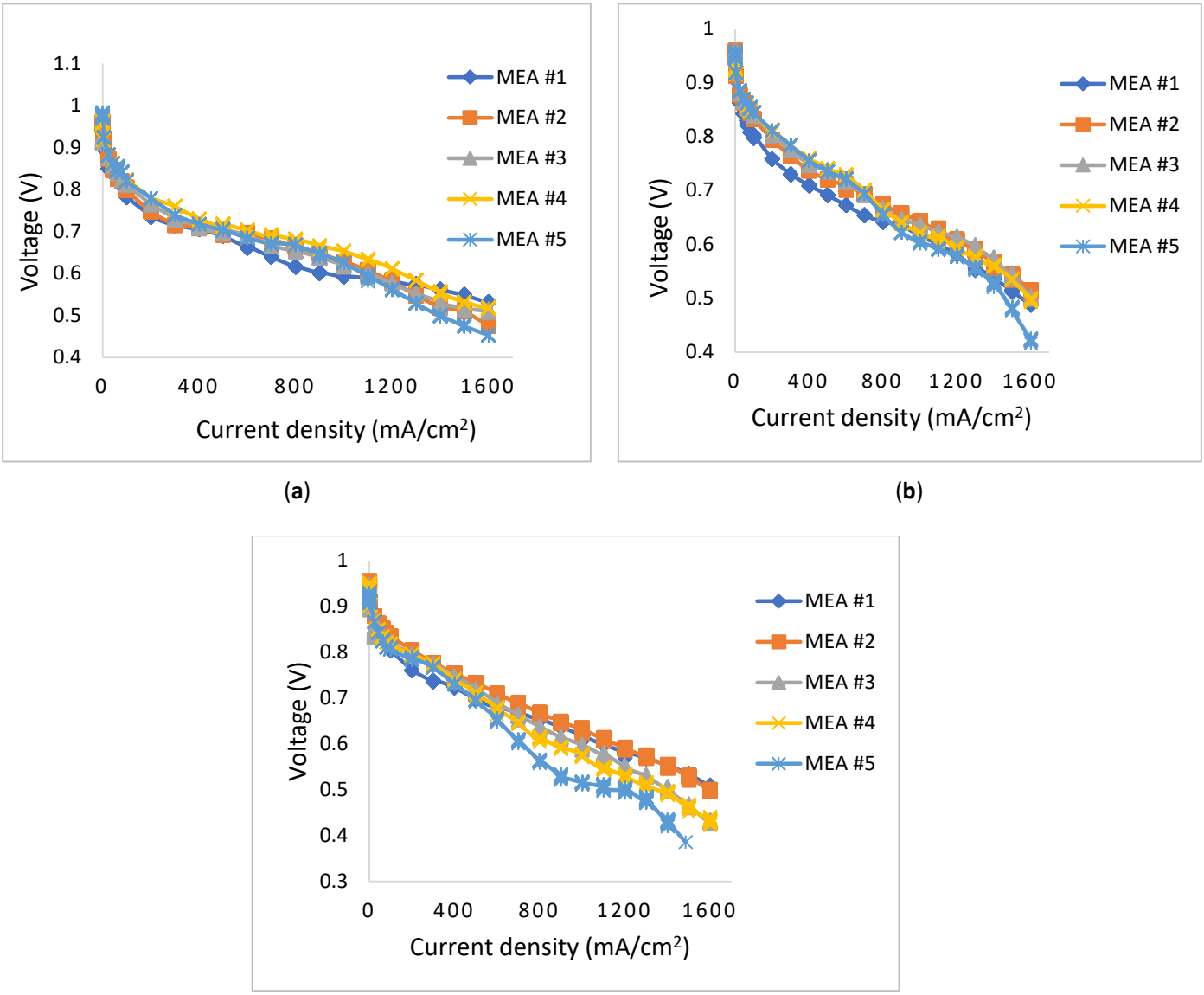

Figure 4.3. Polarization curves representing the I-V relationship for MEAs with increasing ionomer content, under: (a) 20 %; (b) 60 %; (c) 100% RH.

The polarization curves in Figure 4.3 show that the output voltage decreased as the amount of current drawn from the fuel cell was increased. The output voltage is lowered by various resistances experienced through the MEA with increasing current density. At low current densities, a sharp decrease in output voltage is observed due to activation losses. To initiate electron transfer reactions, an energy barrier must

be overcome. This activation energy initiates the chemical reactions, at the cost of activation voltage losses. The cathode oxygen reduction reaction (ORR) kinetics are much slower compared to the anode hydrogen oxidation reaction (HOR) and is the largest contributor to these losses (Marr & Li, 1999). Depending on the microstructure of the CL, any of the transport steps in the TPB layer: the transport of protons, oxygen, and electrons to and from the catalyst active sites, can limit the rate of the ORR (Zhao et al., 2012). The lower ionomer content MEA (MEA #1) demonstrated the highest activation losses at 200 mA/cm^2: 0.73 V at 20 % RH & 0.76 V from 60-100 % RH, due to its weakened ability to conduct protons from electrochemical active sites. Increasing ionomer content resulted in improved activation polarization characteristics due to decreased charge transfer and internal ionic resistances (Lee et al., 1998).

The intermediate region is the ohmic loss region and the high current density region is the mass transport loss region. Ohmic losses represent a combination of ionic and electronic resistances, membrane resistances, and contact resistances. Mass transport losses in the high current density region are associated with gas diffusion limitations from the supply channels to the CL active sites where electrochemical reactions occur (Yousfi-Steiner et al., 2008). At lower RH (20-60 %), MEA #1 demonstrated the largest ohmic losses due to poor proton conductivity. However, at fully humidified conditions the voltage dropped dramatically for the highest ionomer loading MEAs (MEA #4 & #5) in the ohmic region while lower loading MEAs (MEA #1 & #2) showed fewer losses. Ionomer has hydrophobic and hydrophilic properties: its water uptake ability increases with an increase in RH (Xu et al., 2005). At high RH, ionomer films are fully hydrated and therefore thicker- elongating proton and electron pathways hence the increase in charge transfer resistance was observed. This is most likely with the high ionomer content MEAs which retain more water.

The MEA with the highest ionomer loading (MEA #5) experienced higher mass transport losses in all RH conditions due to its higher water uptake ability. This was demonstrated by the sudden drop of potential at high densities. Ineffective removal of water from the cathode blocks the active sites resulting in a voltage drop. The thicker ionomer film in higher ionomer content CLs has been found to reduce the catalyst contact area and impede oxygen diffusion, thus increasing charge transfer and mass transport resistances (Ma et al., 2009; Sciboh et al., 2008).

The maximum voltage produced by an MEA when no current is drawn is expressed by the open circuit voltage (OCV). In this study, the open circuit voltages (OCVs) were found to be RH dependent with increasing ionomer content, and always less than the thermodynamic value for oxygen (1.23V versus NHE

at 25℃). The OCVs ranged between 0.9 - 1V. Low OCVs (0.9-1 V versus NHE) have been investigated in previous studies and the OCV losses were attributed to cathode mixed potentials, hydrogen crossover, and oxygen impurities (Parthasaraty et al.,1992; Zhang et al., 2006; Francia et al., 2011). The OCVs obtained for each MEA (MEA #1- #5) under different RH conditions are shown in Figure 4.4.

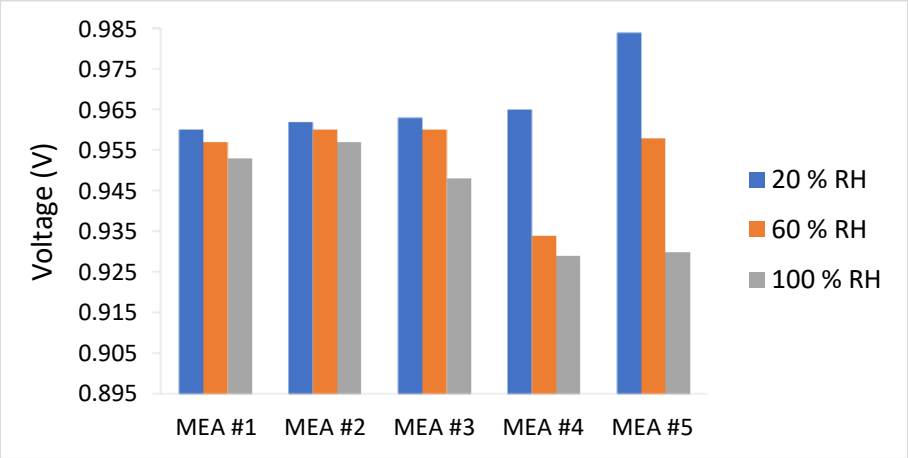

Figure 4.4. Open circuit voltage of the MEAs with increasing ionomer content (20 -35 wt.%) under various RH conditions.

The OCV decreased with an increase in RH from 20-100 %. Hydrogen crossover increases when the temperature and RH of a cell increase, and consequently decreases the OCV (Francia et al., 2011; Bail et al., 2013). The variation was insignificant (2%) for lower loading MEAs (MEA #1- #3) indicating the hydrogen crossover and catalyst loadings were consistent. However, higher ionomer loadings (MEA #4-#5) showed about 5% variation in OCV from 20-100 % RH which indicates that the hydrogen crossover significantly increased for these MEAs. This change is related to ionomer content and its ability to absorb water. More hydrogen gas is likely to crossover with very high-water content in the MEA. A decrease in OCV could also be attributed to a loss in catalytic activity as active sites are increasingly covered by water molecules with increasing RH.

Figure 4.5 summarizes the current densities of the loaded MEAs under increasing RH conditions, measured at 0.65 V. This represents the voltage at which benchmark performance for automotive design systems from ambient to saturated conditions (0-100 % RH) is determined (Debe, 2012).

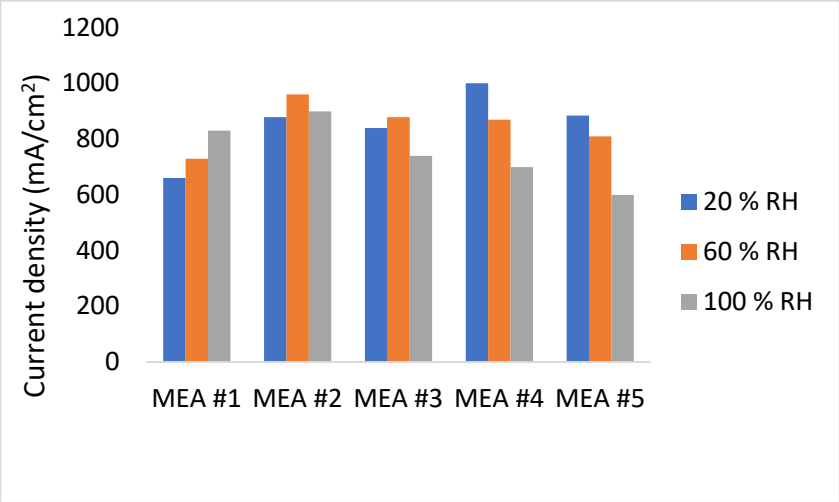

Figure 4.5. Current density at 0.65 V determined for the MEAs with increasing ionomer content under varied RH (20 % to 100 %).

At dry conditions, the MEA performance (current density) increased with increasing ionomer loading. At low humidity, higher ionomer conductivity is crucial to increase membrane moisture as well as increasing proton conductivity. When membranes dehydrate, the size of water clusters within the polymer structure decreases and thus narrow the interconnecting channels. The mobility of protons through the membrane becomes restricted leading to a drop in the membrane conductivity (Beattie et al., 2001; Yan et al., 2006). An increase in ionomer content increases proton conductivity and Pt utilization as more protons are transported to the active sites (Antolini et al., 1998; Martin et al., 2010). However, the H_2/Air performance shows an optimum ionomer loading of 32 wt.%. A further increase in ionomer loading (35 wt.% I) was observed to decrease performance due to electronic resistance imposed by the presence of thicker ionomer films. A similar result was also reported by Andersen & Grahl-Madsen (2016) who observed ionomer coverage to increase linearly with ionomer loading up to 30 wt.%. They concluded that a further increase in ionomer loading triggers ionomer agglomerates, causing lower coverage of the catalyst, poor Pt/C-ionomer bonds and thus leads to poor proton conductivity. Uchida et al. (1995) also reported that adding ionomer beyond optimum value results in the formation of ionomer films on the external surface of the electrode which lowers performance.

The performance of the 20 wt.% I MEA (MEA #1) increased with increasing RH. Low ionomer content MEAs have lower hydration levels at the electrode surface which can lead to higher charge and mass diffusion limitations (Zhiani & Majidi, 2013). Increasing RH increases the hydration of the membrane and hence improves membrane conductivity. Proton conductivity in the CL also increases with RH due to increasing

water channels for proton transportation, leading to improved MEA performance. Under fully humidified conditions, a decrease in performance was observed for higher loading MEAs (MEA #3- #5) due to increased charge transfer resistances. The observed performance losses are possibly due to increased water-infused ionomer film thickness around Pt/C agglomerates. These films result in significant mass transfer resistances, poor proton and electron conductivity. This trend was also reported by Jeon et al. (2010); Zhao et al. (2012) and Kim et al., (2001).

4.4. Electron transport resistance in the CCL using EIS

EIS was used to identify electronic resistances that limit the performance of the different ionomer loaded MEAs over the RH range. The corresponding EIS analysis was performed at 0.5 mA/cm^2 current density in a H_2/Air and a frequency sweep from 20 kHz – 0.1 Hz at steps of 50. The resulting Nyquist plots are presented in Figure 6 showing the imaginary impedance (Z'') as a function of real impedance (Z'). The plots highlight the impedance spectrum from 20 kHz- 0.1 Hz with an arc evident within a frequency range. The Nyquist plot is useful for identifying resistances in the cell at both the high frequency >10 kHz (to the left of the curve) and low frequency <1 Hz (to the right of the curve) intercepts on the real impedance (Z') axis (Jalani et al., 2006). At high frequency range, ohmic resistances dominate while the intermediate frequency region is dominated by kinetic and charge transfer resistances (R_{ct}). Charge transfer resistances depend on interfacial reaction kinetics resulting from the three-phase boundary zone. The magnitude of total ohmic resistances (R_Ω) of the cell, being mainly the resistive contribution of the electrolyte and the two electrodes, is determined by the intercept of the high frequency curve with the Z' real axis. The resistance of the current collectors and platinum wires are considered negligible. At low frequencies, diffusional resistances are dominant (R_{mt}). The low frequency intercept gives the total resistances of the half-cells which is a sum of ohmic and polarization resistances ($R_\Omega + R_p$) (Taillades et al., 2009).

The EIS spectrum generally shows two distinctive arcs, representing the charge transfer resistance (R_{ct}) and the mass transport resistance (R_{mt}), respectively. Depending at which current density the frequency sweep is performed, charge transfer resistances can be greater than mass transfer resistances and only one arc would be visible. Figure 4.6 shows the Nyquist plots obtained for the ionomer loaded MEAs (MEA #1-#5). The mass transfer resistance arc is reasonably small to insignificant in the Nyquist plots because the study was conducted at low current density (0.5 mA/cm^2) where charge transfer resistances dominate.

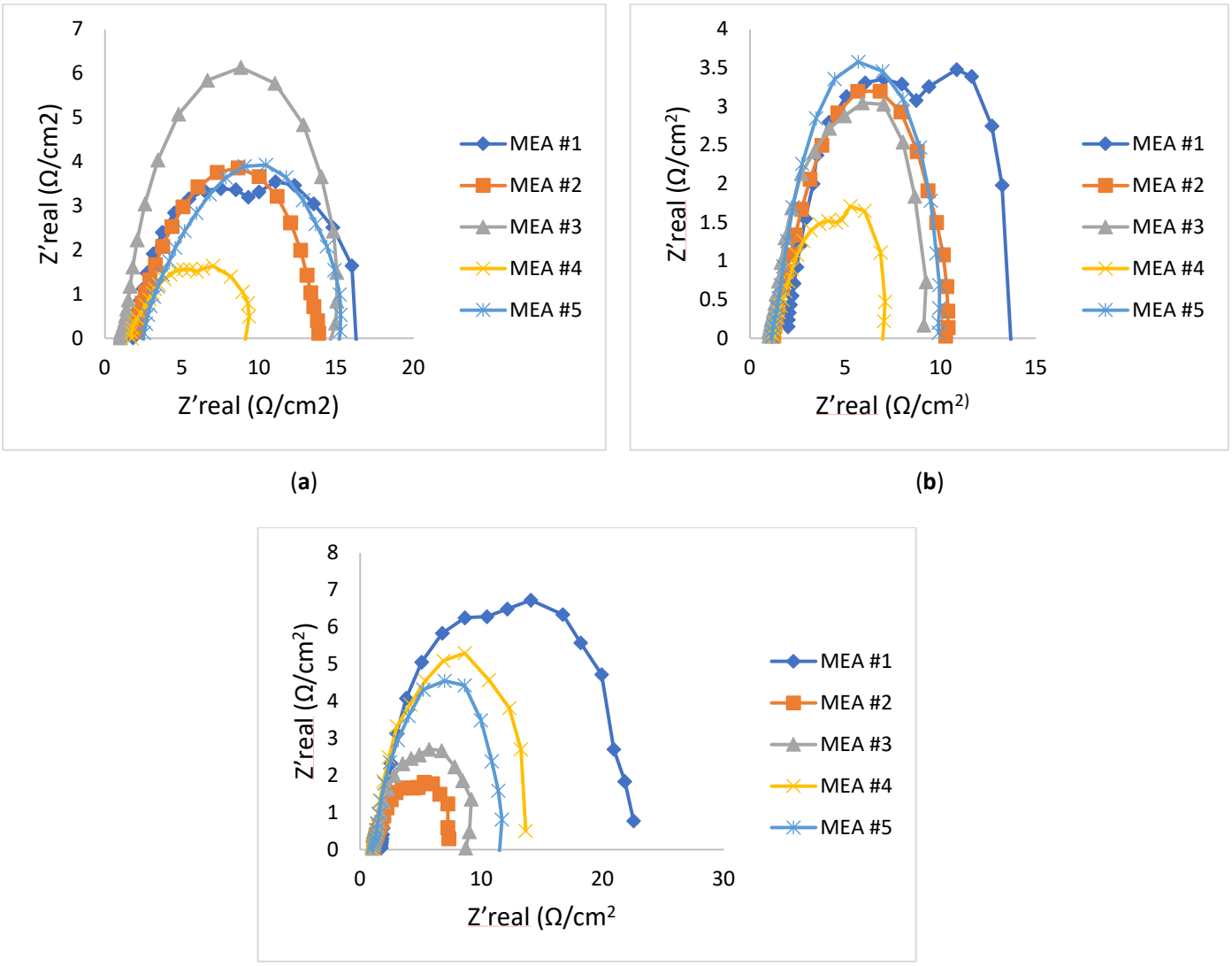

Figure 4.6. Nyquist plots of MEA# 1-5 in H_2/Air determined for: (a) 20 % RH; (b) 60 % RH; (c) 100 % RH.

Charge transfer resistances decreased when the RH was increased to 60 %. However, at fully humidified conditions the charge transfer resistances only decreased for MEAs with moderate ionomer loadings (MEA# 2 & #3) and increased for MEAs with low (MEA #2) and high ionomer loadings (MEA #4 & #5). Meanwhile, the ohmic resistances were observed to decrease with increasing RH for all MEAs.

In all cases, impedance diagrams were analyzed and fitted using Z-View software. This equivalent circuit model in Figure 4.7 represents a Randles cell circuit model, commonly used to model the Nyquist plots for layer-by-layer fully covered electrode surfaces (Lee et al., 2008; Uygun & Sezgintürk, 2011; Uygun &

Uygun, 2014). It represents the ohmic resistance as the in-series resistance, R1, and the diameter of the semi-circle (charge transfer resistances) is modeled by R2. The Warburg impedance (Ws1) represents the mass transfer towards the electrode surface and CPE1 is the capacitance of the electrode surface. A summary of results is reported in Table 4.3.

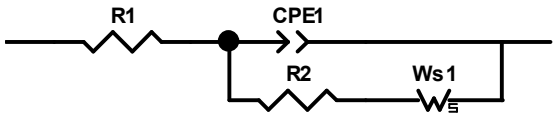

Figure 4.7. The Randles Equivalent circuit design applied for modeling the EIS of MEAs with different ionomer loading. R1 is the ohmic resistance; CPE (constant phase element) is associated with the double layer capacitance; R2 the electron transfer resistance and Ws1 is the Warburg impedance.

Table 4.3. Summary of fitting parameters determined with the Randles equivalent circuit.

		MEA #1	MEA #2	MEA #3	MEA#4	MEA #5
R1 (Ωcm^2)	20 % RH	1.635	2.019	1.087	1.459	2.534
	60 % RH	1.774	1.325	0.9901	1.218	1.247
	100 % RH	1.659	1.115	1.220	1.085	1.110
R2 (Ωcm^2)	20 % RH	14.16	10.56	9.667	8.470	11.88
	60 % RH	10.64	5.873	6.608	4.972	5.436
	100 % RH	18.72	6.004	7.427	11.22	9.581

Ohmic resistances (R1)- The largest ohmic resistances were observed in dry conditions for all MEAs (MEA #1-#5), mostly influenced by poor membrane proton conductivity. At higher RH, MEA #1 experienced higher ionic transport resistances compared to other MEAs (MEA #2- #5) due to the smaller number of ionic conducting sites. At low ionomer contents, there is not enough ionomer coverage of the Pt/C- I particles and are therefore ionically isolated. Protons therefore cannot be transported to the active sites which results in high ionic resistances and low Pt utilization. At high RH (60- 100 %) the ionic resistances of higher loading MEAs (MEA #2- #5) are in the same range and are approximately 1 Ωcm^2. However, MEA #5 ionic resistances decreased more rapidly compared to other MEAs (MEA #1- #4) when RH was increased to 60 %, showing a 51 % decrease. This is a coupled effect of moisture in the CL and higher ionomer content in the CCL leading to higher proton conductivity.

Charge transfer resistances (R2)- the charge transfer resistances decreased for all MEAs (MEA #1-#5) at 60% RH. According to Lee et al. (1998), at high RH, proton transport through the membrane becomes significant enough to affect the ORR kinetics and decrease charge transfer and ionic resistances. Under dry conditions, the charge transfer and mass transport resistances decreased with ionomer loading until

32 wt.% I (MEA #4), then increased again at 35 wt.% I (MEA #5). Increasing ionomer content results in extension of the triple-phase reaction zone and consequently decreases charge transfer and internal ionic resistances (Lee et al., 1998). However, excess ionomer loading results in increased charge transfer resistances due to thicker ionomer films covering the electro-conductive area. MEAs with higher ionomer content (MEA #4) had the least charge transfer resistances at 20 % RH due to increased moisture in the CL and thus increased proton conductivity. The low electronic resistances likely added to the good performance observed for MEA #4 under dry conditions.

Charge transfer resistances were significantly larger for MEA #1 under all RH conditions due to lower Pt utilization caused by weaker Pt/C-I bonds. Adding excess water (with higher humidity) to a lower ionomer loading MEA (MEA#1) led to even larger charge transfer resistances as observed in Figure 7 (c). Under fully humidified conditions, an increase in mass transfer and charge transfer resistances was also observed for higher ionomer loading MEAs (MEA #4 & #5). At high RH, thick ionomer films absorb more water and swell which increases the conductive pathway, increasing charge transfer resistances.

4.5. MEA ionomer content optimization

Radar charts were used to compare to what extent each of the different ionomer loading MEAs (MEA #1-#5) meets the desired electrochemical MEA benchmark targets, at different RH conditions. The analysis has been confined to the following parameters and corresponding benchmarks:

1) Based on the current data, the charge transfer ohmic resistances were set to potential targets of 4 Ωcm^2 and 0.8 Ωcm^2, respectively.
2) ECSA, 100 $mgPt/cm^2$
3) OCV, 1 V
4) Performance at 0.65 V, 1.5 A/cm^2 (minimum target for automotive fuel cells (Debe, 2012)).

The comparative radar charts in Figure 4.8 illustrate how each of the MEAs meets the desired benchmark targets. The radial scale indicates individual dimensions in terms of percentage, with each benchmark target at 100 %.

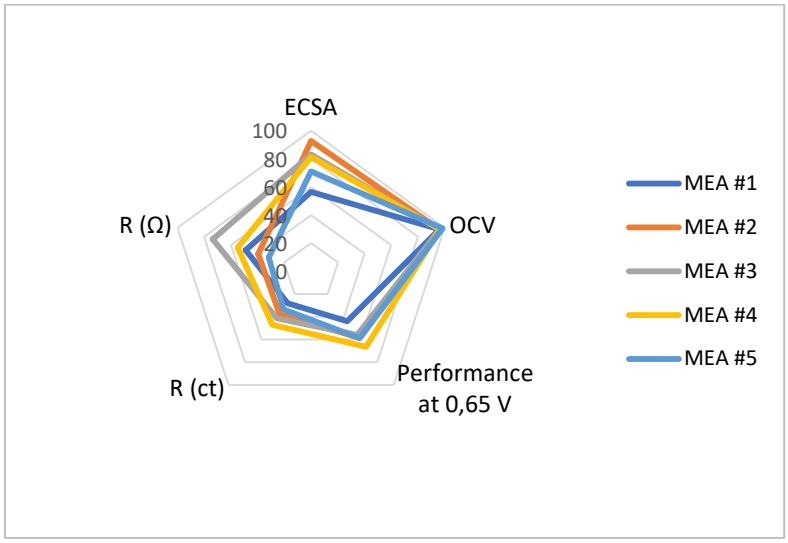

(a)

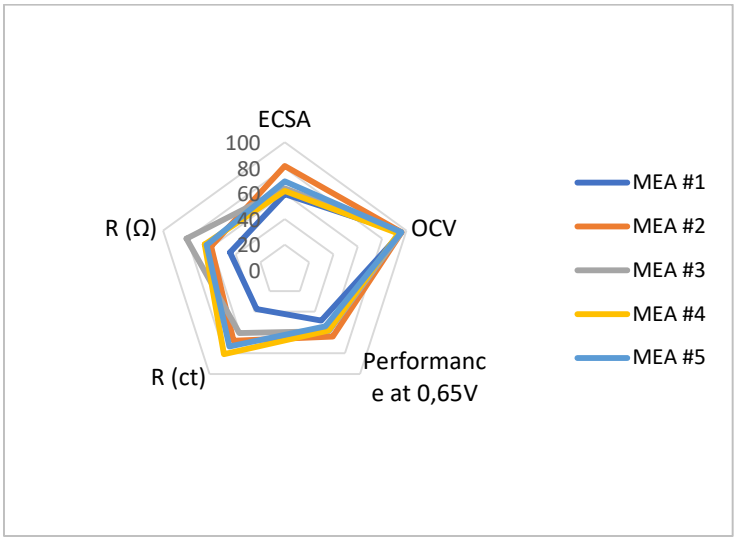

(b)

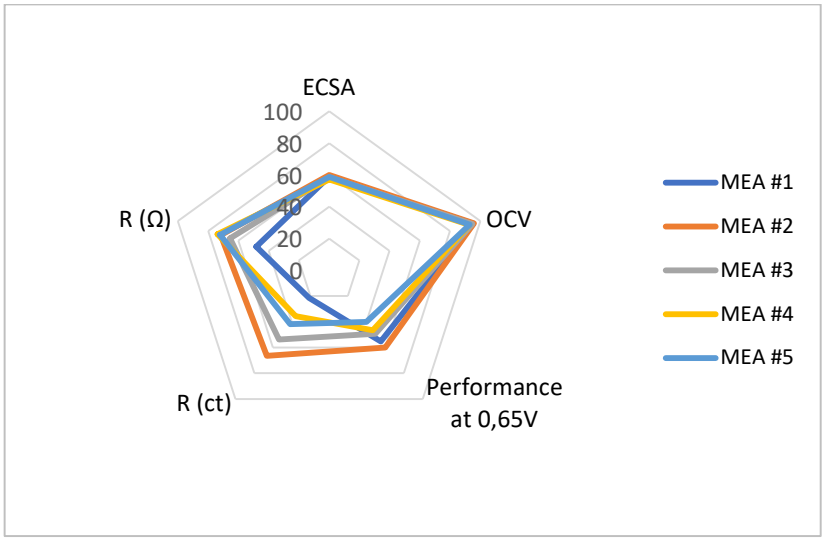

(c)

Figure 4.8. A radar chart analysis showing the performance of different ionomer content MEAs at: (20 %); (b) 60 %;(c) 100 % RH.

The OCV is within the same range for all MEAs (MEA #1- #5) and only <7 % to the target. At all RH conditions, the pentagon of MEA #1 is significantly narrowed compared to other MEAs (MEA #2- #5) which signifies the least capability for this MEA (MEA #1) to reach targets. The highest performance at 0.65 V was achieved by MEA #4 (1000 mA/cm^2) under 20 % RH conditions. Looking at ionic resistances (R_Ω), the optimum ionomer loading is 28 wt.%- a further increase in ionomer loading results in a decrease in proton conductivity.

From the radar charts comparing of ECSA, R_{ct}, R_{Ω}, and performance at 0.65 V, the MEA with 24 wt.% I (MEA #2) demonstrated the highest level of meeting relevant targets. This MEA was selected as the benchmark MEA for comparison purposes in the following chapter. A similar value to this optimal ionomer content has been reported by Li et al. (2010) who found the optimal ionomer content of 25 wt. % I in the CCL to exhibit the best performance. The highest current density achieved by this MEA (960 mA/cm^2) at 0.65 V is 36 % less than the performance benchmark target.

4.6. A summary of observations and findings

Analysis of the voltage loss at 0.65 V in state-of-art MEAs showed the performance to be highly dependent on ionomer loading and RH of the feed gases in fuel cell operation. This is supported by previous studies (Yan et al., 2006). Low ionomer loading MEAs demonstrated high performance under high RH conditions while high ionomer loading MEAs performed better at low RH conditions. The change in performance was associated with the change in ohmic and charge transfer resistances of the different ionomer loadings under varying RH conditions. At dry conditions, high ionomer loading MEAs were favourable because of their high proton conductivity. However, as RH increased their increased water uptake resulted in more ionomer swelling, increased ionic pathways, and the MEAs became susceptible to flooding, consequently decreasing performance. Meanwhile, lower ionomer loading MEAs were desirable for higher humidity conditions. Therefore, for 20 % RH conditions, the optimal ionomer content would be 32 wt.% I and for wet conditions, the optimal ionomer content would be 24 wt.% I.

CHAPTER 5

5. Stratification of cathode catalyst layers

This chapter describes the design of an ionomer-gradient cathode catalyst layer (CCL) for low-temperature PEMFCs. Two stratified CCL MEAs (MEA#6 and MEA #7) were fabricated consisting of two layers of varying ionomer content adding to the same Pt loading (0.4 mg_{Pt}/cm^2 on the cathode). The electrochemical characterization, physical characterization, and carbon corrosion tests for these MEAs were performed and their results were compared to the benchmark MEA selected in Chapter 4 (24 wt.% I MEA #2).

5.1. Design of a stratified cathode CL

The performance of an MEA can be improved by optimizing the design and structure of the cathode catalyst layer (CCL) to facilitate ideal water and reactant transport in the CL (Shahgaldia et al., 2018). In this study, the CCL transport properties were optimized by introducing two sublayers consisting of different ionomer contents. The total Pt loading was kept constant at 0.4 mg_{Pt}/cm^2 for the cathode and 0.1 mg_{Pt}/cm^2 for the anode, respectively. Previous performance studies of PEMFC MEAs have shown that the performance of the MEA is improved when the ionomer content decreases moving away from the membrane (Xie et al., 2005; Roshandel & Farhaneih, 2007; Chen et al., 2017). Based on these previous findings, the CCL was stratified to have a higher ionomer loading in the first layer coated onto the membrane and a lower loading in the second layer. The optimal ionomer contents for stratification were based on the results presented in Chapter 4. MEAs with ionomer loading of 24 wt.% and 28 wt. % were chosen as the optimum loadings for the sublayers owing to their good performance and higher ECSA compared to the other monolayer MEAs studied.

Two stratified MEAs of different CL compositions were designed. Each of the MEA CCLs consisted of varying ionomer content in the sublayers while keeping the total cathode Pt loading constant at 0.4 mg_{Pt}/cm^2. The ionomer content was gradually decreased from the first layer to the second layer: with 28 % I in the first and 24 wt.% I in the second layer. The first stratified MEA (MEA #6) was designed to have a ratio of 1:3 Pt loading, i.e. the membrane was coated with 0.1 mg_{Pt}/cm^2 Pt in the first layer and 0.3 mg_{Pt}/cm^2 in the second layer. The second stratified MEA design had a 1:1 Pt loading ratio, with each layer consisting of 0.2 mg_{Pt}/cm^2 Pt loading. A schematic diagram of the two stratified CCL designs is shown in Figure 5.1.

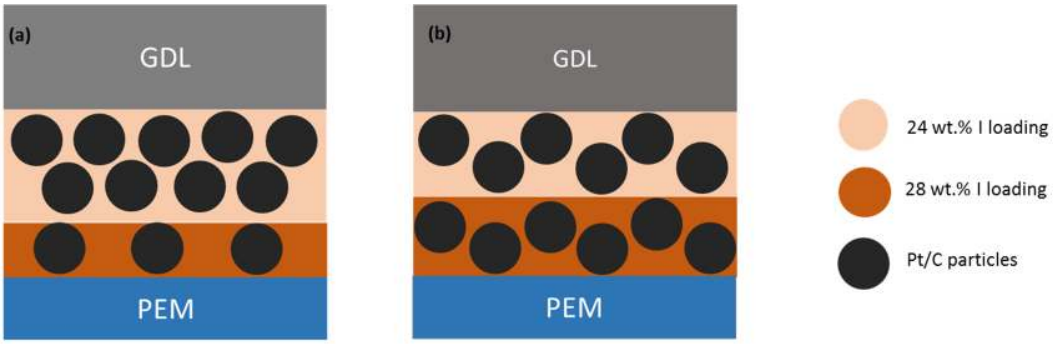

Figure 5.1. A schematic diagram of ionomer loading-gradient CCL designs consisting of: (a) 1:3 Pt loading ratio (MEA #6); (b) 1:1 Pt loading ratio (MEA #7), in the respective layers.

5.2. Catalyst layer thickness

SEM analysis was conducted to determine the thicknesses of the stratified and non-stratified CCLs. Figure 5.2 shows the cross-sectional images of the MEAs. The PEM is sandwiched between the cathode (top) and the anode (bottom) CL.

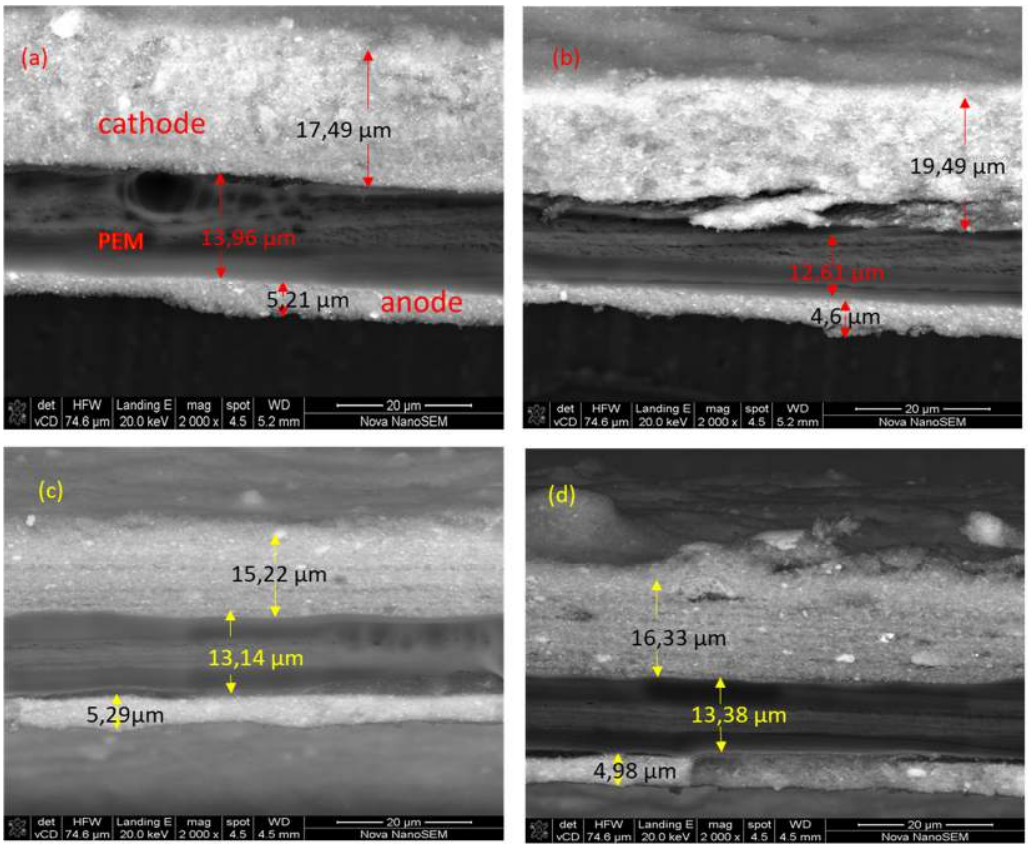

Figure 5.2. SEM image of the stratified and non-stratified MEA cross-sectional area: (a) MEA #2; (b) MEA #3; (c) MEA #6; (d) MEA #7.

The average catalyst layer thicknesses were determined and are summarized in Table 5.1. The MEA thickness was measured using a thickness gauge. Stratified MEAs (MEA #6 & #7) were approximately 8 % thinner than monolayer MEAs (MEA # 2 & # 3). The MEA PEM and anode CL were consistent with a less than 1% variation in their thickness.

Table 5.1. Catalyst layer thicknesses of the monolayer and stratified CCL MEAs.

MEA	MEA Thickness (mm)	Cathode CL thickness (µm)	Anode CL thickness (µm)
MEA #2	0.05180	17.49	5.210
MEA #3	0.05240	19.49	4.600
MEA #6	0.04200	15.22	5.290
MEA #7	0.04400	16.33	4.980

MEA #7 is 6.8 % thicker than MEA #6, likely due to its higher total ionomer load (more 28 wt.% I). From SEM imaging no structural changes were observed between the stratified and non-stratified CCL structures.

5.3. BET analysis

BET analysis was conducted to determine the porosity and surface area in the CL microstructure resulting from the thinner stratified CL. The results are summarized in Table 5.2. The bulk density of the samples was calculated using the mass and volume of the samples.

Table 5.2. Pore characteristics of the monolayer and stratified cathode layers in the MEAs.

MEA	Bulk density (g/cm^3)	Ionomer wt.%1st sublayer	Ionomer wt.% 2nd sublayer	Cumulative pore volume (cm^3/g)	BET surface area (m^2/g)	Porosity (%)
MEA #2	0.8157	24	--	0.1443	70.91	11.78
MEA #3	0.8379	28	--	0.1851	65.16	15.50
MEA #6	0.9847	28	24	0.03762	48.11	4.680
MEA #7	1.000	28	24	0.05280	60.14	6.550

The bulk density shows that the stratified CCL MEAs (MEA #6 and #7) have a denser layer compared to the non-stratified MEAs (MEA #2 and MEA #3). The denser layer is likely due to the arrangement of

agglomerates in the stratified CCL MEAs. Monolayer MEAs (MEA #2 and MEA #3) have monodisperse agglomerates (same size agglomerates) while the stratified MEAs comprise polydisperse agglomerates (different size agglomerates). Polydisperse agglomerates pack together more closely than monodisperse agglomerates. Also, stratified MEAs (MEA #6 and MEA #7) have a lower BET surface area, cumulative pore volume and porosity compared to monolayer MEAs. This result differs from findings reported by Shaghaldi et al. (2018) who found the ionomer-gradient CCL MEA to have a higher total pore volume, and surface area than the monolayer MEA design with the same overall Pt and ionomer loading. In their study, Shaghaldi et al. (2018) applied an ionomer gradient CCL MEA consisting of 30 wt.%I in the 1st layer and 23 wt.% I in the 2nd layer. They found that the monolayer MEA had a more compact cathode CL comprised of Pt/C-ionomer agglomerates with fewer macropores. However, Shaghaldi et al. (2018) also used a different type of supported catalyst and ionomer, both posing a significant impact on the Pt/C-ionomer agglomeration in the CCL.

5.4. Determination of ECSA

The electrochemical surface area (ECSA) of the ionomer gradient MEAs was measured and compared to the benchmark monolayers. Figure 5.3 compares the ECSAs of stratified and non-stratified MEAs under different RH conditions.

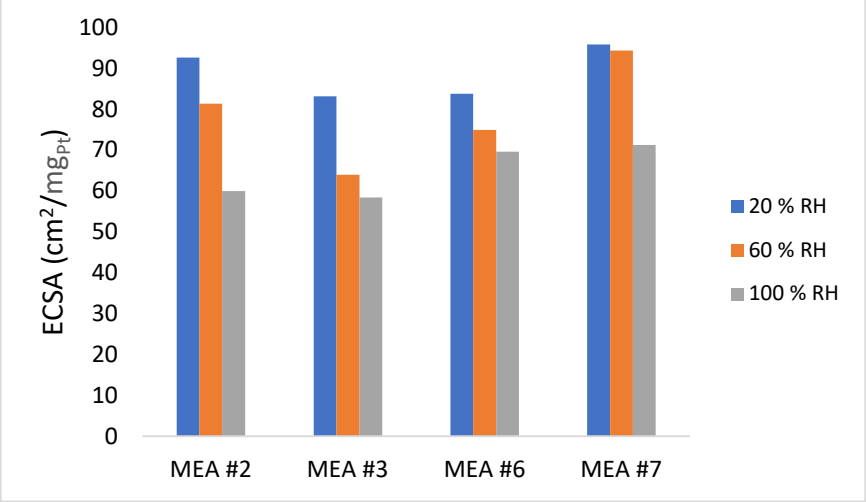

Figure 5.3. ECSAs of the stratified CCL MEAs, compared to the benchmark monolayer MEAs.

The ECSA decreased as the RH was increased to fully humidified conditions, as observed from the various ionomer loading MEAs studied in Chapter 4. At 100 % RH, stratified MEAs (MEA #6 & #7) had higher ECSAs

than monolayer MEAs (MEA #2 & #3). A similar result was obtained by Shaghaldi et al. (2018), and the higher ECSAs for the ionomer gradient MEAs were ascribed to the trade-off between gas reactant access and electrolytic conductivity. The higher ionomer content adjacent to the membrane extended the triple-phase zone in the first layer, while the lower ionomer content in the second layer allowed more gas reactant access to the active sites. This becomes more favorable at high RH where the access to active sites becomes restricted by water. For similar reasoning, MEA #7 which had a higher Pt/C -ionomer ratio in the first layer had the highest ECSA under all studied RH conditions. The inner layer had a higher ionomer loading which provided increased triple-phase boundary sites (Lee et al., 1998; Kim et al., 2008). A lower ionomer content in the second layer increased gas access to Pt sites.

5.5. Performance analysis

Polarization measurements were performed for the stratified MEAs and compared to the benchmark non-stratified MEA (MEA #2). The polarization curves in Figure 5.4 demonstrate slightly lower activation losses for the stratified MEAs, under all studied RH conditions: 0.73-0.77 V at 400 mA/cm^2 while MEA #2 attained 0.7-0.75 V. This indicates improved ORR activity in the stratified CCL MEAs (MEA #6 & #7). The thinner CLs (MEA #6 & #7) had shorter conductive pathways reducing charge transfer resistance. MEA #2 activation losses increased with decreasing RH, due to increasing charge transfer resistances.

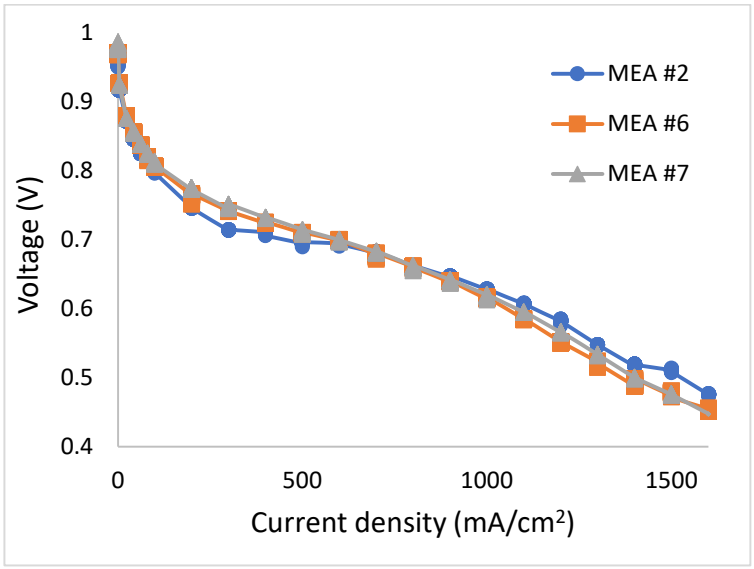

(a)

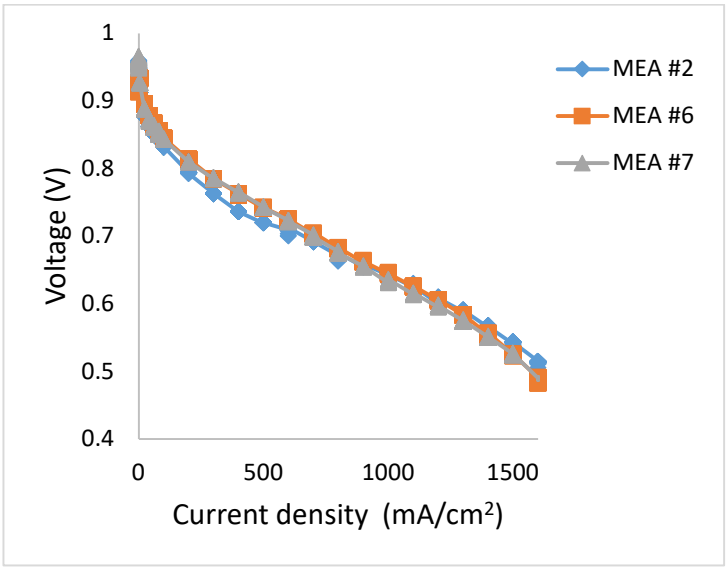

(b)

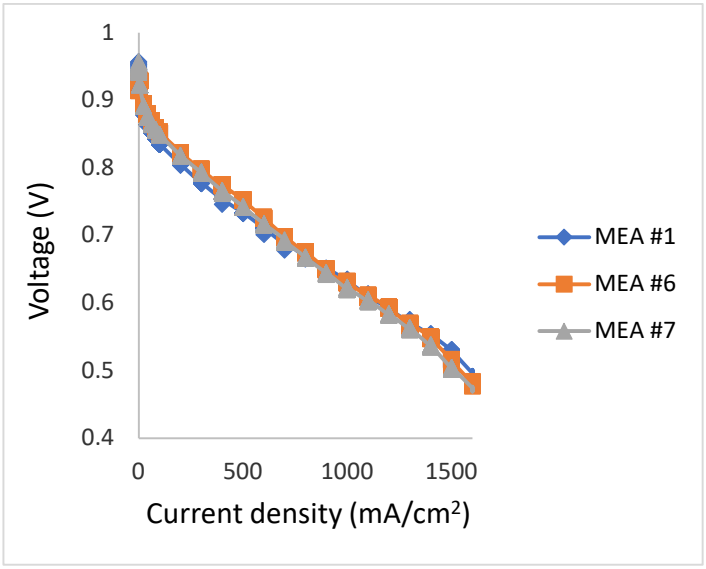

(c)

Figure 5.4. Performance curves obtained for ionomer stratified cathode CL MEAs (MEA #6 and MEA #7) and monolayer MEA #2 under (a)20 %, (b) 60 % & (c) 100 % RH conditions.

The stratified CCL MEAs experienced higher mass transport losses than the monolayer MEA (MEA #2) under the various RH conditions. This could be due to an increase in the CL density observed for the stratified CCLs which increased water retention and blocked reactant access closer to the membrane. MEA #2 demonstrated lower mass transport losses likely due to its higher pore volume and porosity.

Figure 5.5 compares the open circuit voltage (OCV) of the stratified MEAs to the non-stratified MEA (MEA #2). The OCV decreased with increasing RH for all MEAs, with the difference increasing for the stratified layers.

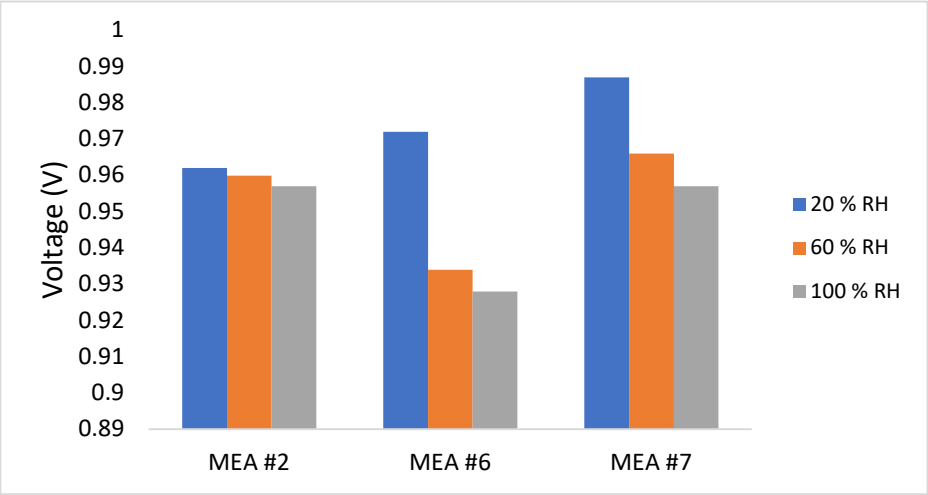

Figure 5.5. Open circuit voltages (OCV) for the stratified and non-stratified MEAs under 20 %, 60 %, and 100% RH conditions.

The results of this study show a relationship between the OCV and ECSA which is related to ORR kinetics, as reported by Vilekar & Datta (2010). OCVs were higher for the higher ECSA MEA (MEA #7), which is likely due to increased Pt availability and shorter conductive pathways in the CL. Notably, the OCVs of stratified MEAs are much more RH dependent compared to MEA #2 due to the higher ionomer loading in the CL. The same result was seen in Chapter 4 for higher ionomer loading MEAs and it was attributed to the ability of high ionomer loading CLs to absorb water. A summary of the current densities obtained for each MEA (MEA #2, MEA #6 and MEA #7) at 0.65 V is shown in Figure 5.6.

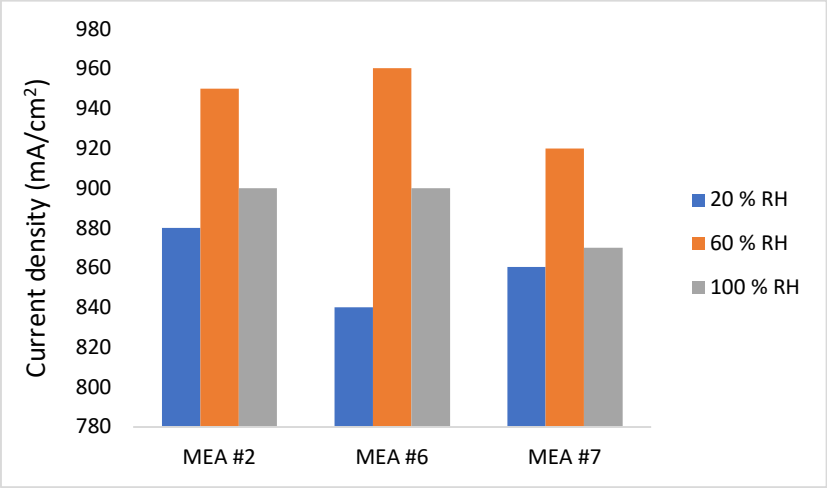

Figure 5.6. Current density of the stratified CCL MEAs and monolayer MEA #2 are compared at 0.65 V, with feed gases humidified from 20 %-100% RH.

The performance of the monolayer MEA #2 at dry conditions surpassed that of the stratified MEAs. MEA #7 had higher performance than MEA #6 under dry conditions. MEA #7 has a higher ionomer loading than MEA #6, therefore has better water uptake ability which facilitates proton conductivity.

At higher RH conditions (60-100 % RH), the membrane is already well hydrated, and the proton conductivity improves, hence the increase in performance observed for all MEAs. MEA #6 which has a lower ECSA, demonstrated higher performance than MEA #7. High performance of ionomer-gradient MEAs with low ECSA has been reported by previous studies and mainly attributed to the ease of reactant transport through the CL, which promotes electrochemical reactions (Chen et al., 2017; Su et al., 2010; Kim et al., 2008). Similar results were observed in this study in which the thinner stratified CCL MEA #6 has a lower ionomer loading than MEA #7.

5.6. EIS under H_2/Air conditions

The internal resistances of the stratified MEAs were characterized using EIS measured at 0.5 mA/cm^2 in a H_2/Air. The resulting ohmic resistances, charge transfer, and mass transfer resistances of the monolayer MEA#2 and stratified MEAs evaluated under different RH conditions are shown in Nyquist plots in Figure 5.7. The results show that the ohmic resistance increased as the RH of feed gases was decreased (Yan et al., 2006). It has been well established that an increase in RH of feed gases results in a decrease in internal resistances (Malevich et al., 2008; Kim et al., 2009; Jeon et al., 2012). An increase in ionomer loading in stratified MEAs resulted in an increase in charge transfer and mass transport resistances. This is caused by thicker ionomer films which elongate transport paths in the CL. Under dry conditions, monolayer MEA

#2 demonstrated smaller charge transfer and mass transport resistance, which corresponds to its higher performance at these conditions. At 60 % RH, MEA #6 demonstrated smaller charge transfer and mass transport resistances, which contributed to its slightly high performance compared to MEA #2 and #7. The charge transfer resistance of MEA #2 is significantly smaller at fully humidified conditions compared to the stratified MEAs. This is owed to its lower ionomer loading and thus less water retention in the CL.

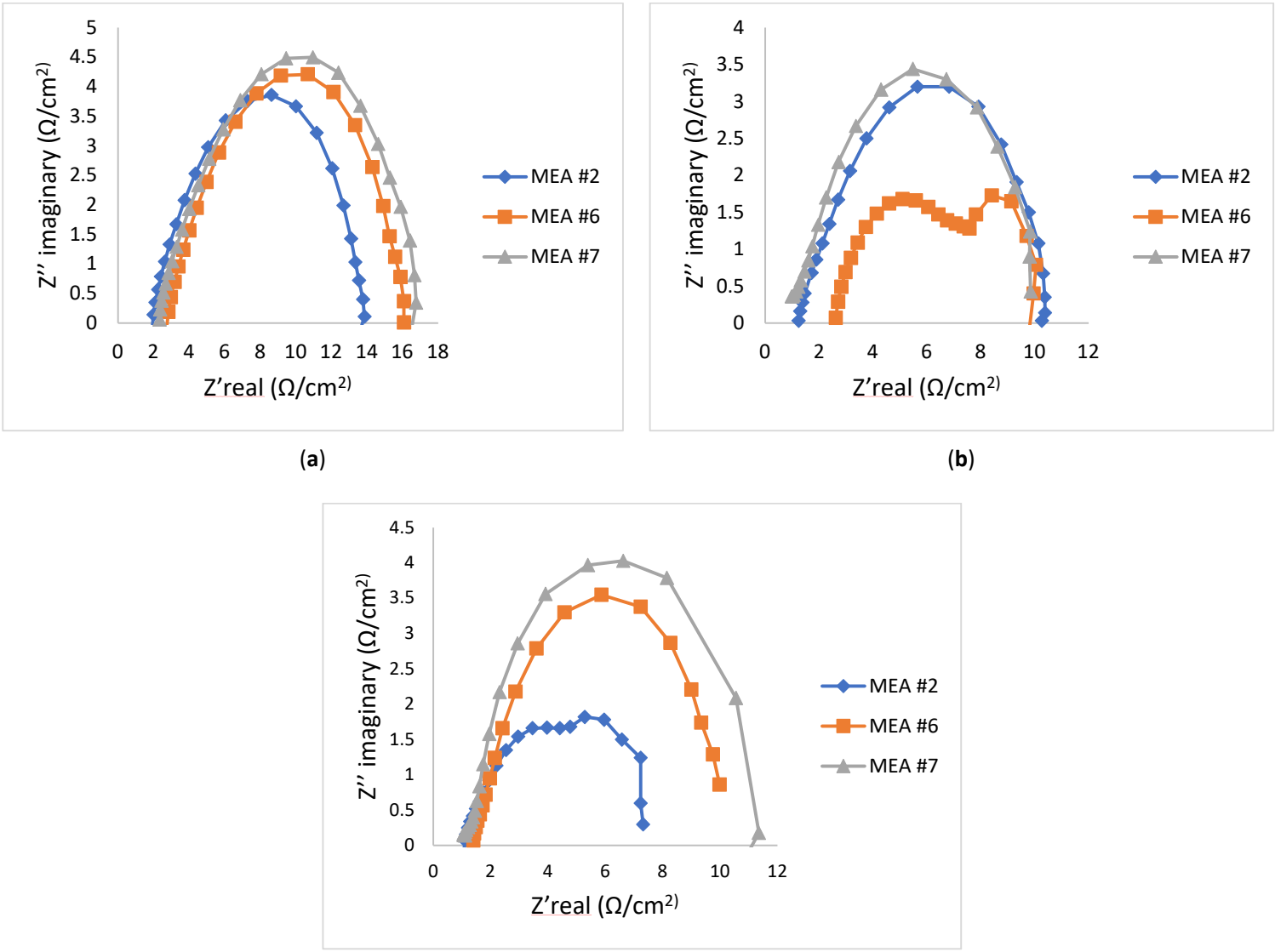

Figure 5.7: Nyquist plots of stratified cathode CL MEAs and monolayer MEA #2 determined at: (a) 20 % RH; (b) 60 % RH; (c) 100 % RH.

The Nyquist plots were fitted with a Randles equivalent circuit model shown in Chapter 4: Figure 4.7, and the results are shown in Table 5.3. The ohmic resistance was modeled by R1 and electron transfer resistance by R2; the mass transfer resistance was modeled by the Warburg impedance (Ws1); and a constant phase element (CPE) was associated with the double layer capacitance on the electrode surface.

Table 5.3. Summary of fitting parameters using the Randles equivalent circuit for modelling the EIS.

		MEA #2	MEA #6	MEA #7
R1 (Ωcm^2)	20 % RH	2.019	2.360	2.510
	60 % RH	1.325	1.560	1.263
	100 % RH	1.115	1.328	1.336
R2 (Ωcm^2)	20 % RH	10.56	13.96	14.06
	60 % RH	5.873	5.775	7.339
	100 % RH	6.004	7.146	7.177

Ohmic resistances R1- The ohmic resistances decreased with increasing RH due to ionomer hydration in the CL, decreased membrane, and proton transfer resistance at wetter conditions. Generally, stratified MEAs had higher ohmic resistances than the monolayer MEA #2 under the various RH conditions. This can be attributed to the decreased porosity of the electrode in stratified CCLs, which narrowed the pathways for ionic transport, potentially increasing the resistance to ionic transport (Beattie et al., 2001; Yan et al., 2006).

Charge transfer resistances R2- The fitted charge transfer resistances are in good agreement with the electrode performance data. At 20 % RH, MEA #2 had significantly lower charge transfer resistances likely resulting in its higher performance at 0.65 V. However, as the RH was increased to 60 %, MEA #6 showed lower charge transfer resistances which subsequent higher performance under 60 % RH conditions. At fully humidified conditions the stratified MEAs demonstrated slightly larger charge transfer resistances than the monolayer MEA #2. This increase in charge transfer resistances can be associated with the ability of thicker ionomer films to absorb water. At high RH, thicker ionomer films swell which increases the conductive pathway, increasing charge transfer resistances. This phenomenon was also observed in Chapter 4 for higher ionomer loading MEAs. MEA #7 had larger charge transfer resistances at all RH conditions. The increasing ionomer content of MEA #7 increased proton conductivity as well as the charge transfer resistances due to thicker ionomer coverage.

The results show that there exists an optimum combination of design parameters for each catalyst layer which can improve MEA performance significantly. It has been reported that an optimal ionomer-gradient can be achieved when the difference in ionomer loading between the two sublayers is 10 wt.% I (Chen et al.,

2017; Xie et al., 2005; Song et al., 2005). In this study, the stratified CCL design was based on a 4 % ionomer gradient selected based on the performance of the 28 wt.% and 24 wt.% monolayer MEAs which also presented larger ECSAs, BET surface areas and higher porosities. There was only ± 1 % performance improvement observed when the same ionomer loadings were used in the stratified CCL layers because the MEA structure was denser, less porous, and presented a lower BET surface area.

5.7. Durability comparison of a stratified and monolayer MEAs

While many studies have investigated the effect of stratification on performance (Xie et al., 2005; Cetinbas et al., 2015; Chen et al., 2017; Shahgaldi et al., 2018), none of the studies have investigated the effect of stratification on MEA durability. In this study, the structural degradation of the MEA due to carbon corrosion was investigated to compare the durability of a stratified and non-stratified MEA. Carbon support corrosion of cathode catalysts in PEMFCs is a major contributor to the degradation of cathode catalysts (Yu & Ye, 2007). Cyclic voltammetry, scanning electron microscopy (SEM), and polarization analysis were performed to correlate the structural changes of the MEA to the performance during cyclic degradation. During the carbon corrosion test, carbon and water oxidation are incurred by cycling voltage across the MEA. The potential was cycled repeatedly between 0 and 1.2 V at 50 mv/s. The changes in the ECSA and the polarization curves were recorded intermittently as described in Chapter 3. For the degradation study, the stratified MEA #6 was selected for its superior performance compared to MEA #7 (at 0.65V). The degradation of MEA#6 was compared to that of monolayer MEA #2.

5.7.1. Catalyst layer degradation

SEM images were taken to observe the structural changes of the catalyst layers in the respective MEAs after the 30-h carbon corrosion test. Figure 5.8 shows the cross-sectional images of the stratified and non-stratified MEAs before and after the degradation test.

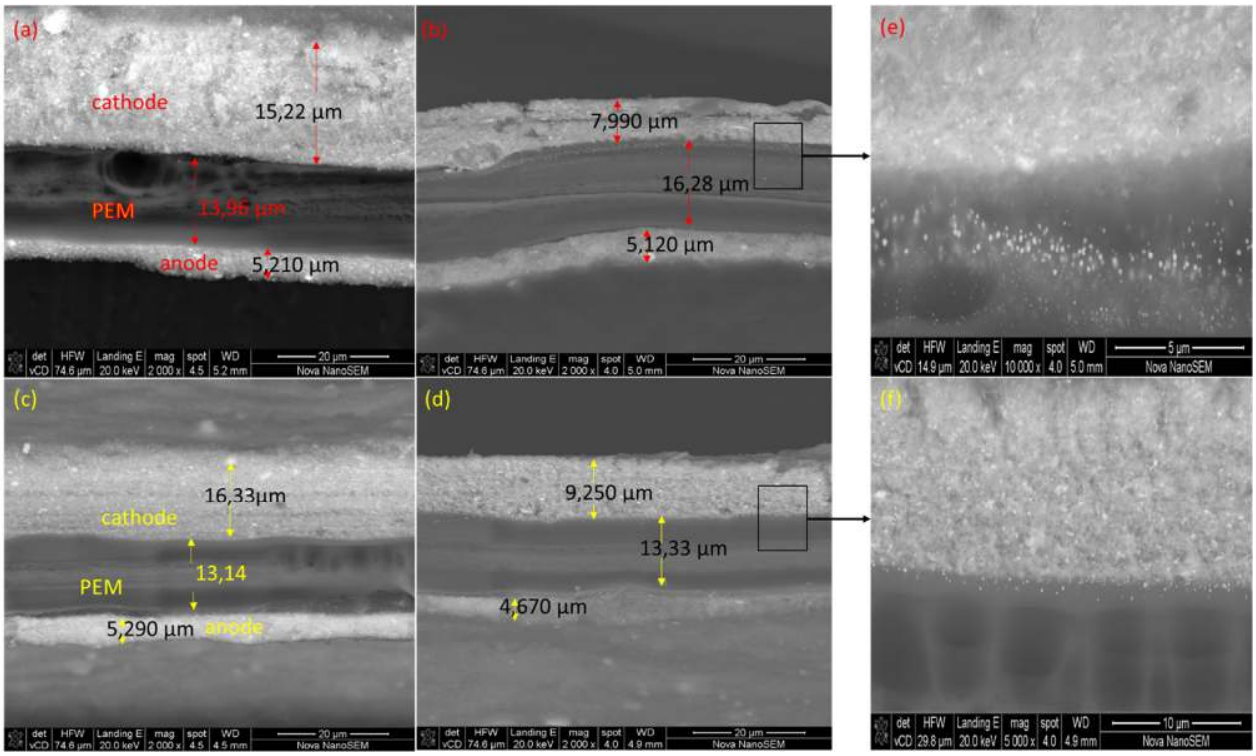

Figure 5.8. A cross-sectional image of: (a) unused stratified MEA#2; (b) MEA #2 after carbon degradation; (c) unused MEA #6; (d) MEA #6 after carbon degradation. A magnified image of the degraded PEM showing Pt migrated from the CL into the PEM in: (e) monolayer MEA #2; (f) stratified MEA #6. The magnified images were captured at 10 000 x magnification.

Thinning of the cathode CL due to carbon support oxidation is observed for both MEAs. After the degradation test, the thickness of the stratified CCL was reduced by 39,22 %, while the monolayer CCL thickness was reduced by 54,32 %. The MEA thicknesses are summarized in Table 5.4.

Table 5.4. Thickness of MEAs before and after the carbon degradation test.

		Before degradation thickness (µm)	After degradation thickness (µm)
MEA #2	Anode CL	5,210	5,120
	Membrane	13,96	16,28
	Cathode CL	17,49	7,990
MEA #6	Anode CL	5,290	4,670
	Membrane	13,14	13,33
	Cathode CL	15,22	9,250

There was no significant change in the anode thickness over the degradation period. In both the stratified and monolayer MEA the PEM expands during the carbon corrosion test. The expansion is caused by plastic deformation due to isotropic and anisotropic swelling (Kusoglu et al., 2007). More membrane swelling was observed in the thicker CCL MEA (MEA #2) which was 12,98 % thicker than MEA #6. This indicates high water retention MEA #2 as thicker CLs retain more water. The water content in the membrane imposes swelling/hydration and results in high mechanical stresses in the membrane which could lead to membrane failure and gas cross over (Yuan et al., 2011; Norin et al., 2002; Solasi et al., 2007). Therefore, the membrane water uptake is critical for reducing the adverse effects of membrane swelling and degradation. Pt migration was also observed for both MEAs, but it was considerably less for MEA #6 (Figure 5.8 (f)) compared to MEA#2 (Figure 5.8 (e)). As the carbon support degrades, Pt particles dissolve and migrate and precipitate onto the membrane surface resulting in loss of electrochemical activity in the CL. Pt migration onto the membrane drastically decreases its stability and conductivity (Yuan et al., 2011). Ionomer coverage around the Pt/C aggregates has been shown to inhibit Pt dissolution and sintering (Curnick et al., 2010). The 28 wt. % ionomer loading (more ionomer coverage) on the Pt/C aggregates adjacent to the membrane of MEA #6 possibly played a role in inhibiting Pt migration.

The change in CL surface due to carbon degradation is shown by the SEM images presented in Figure 5.9.

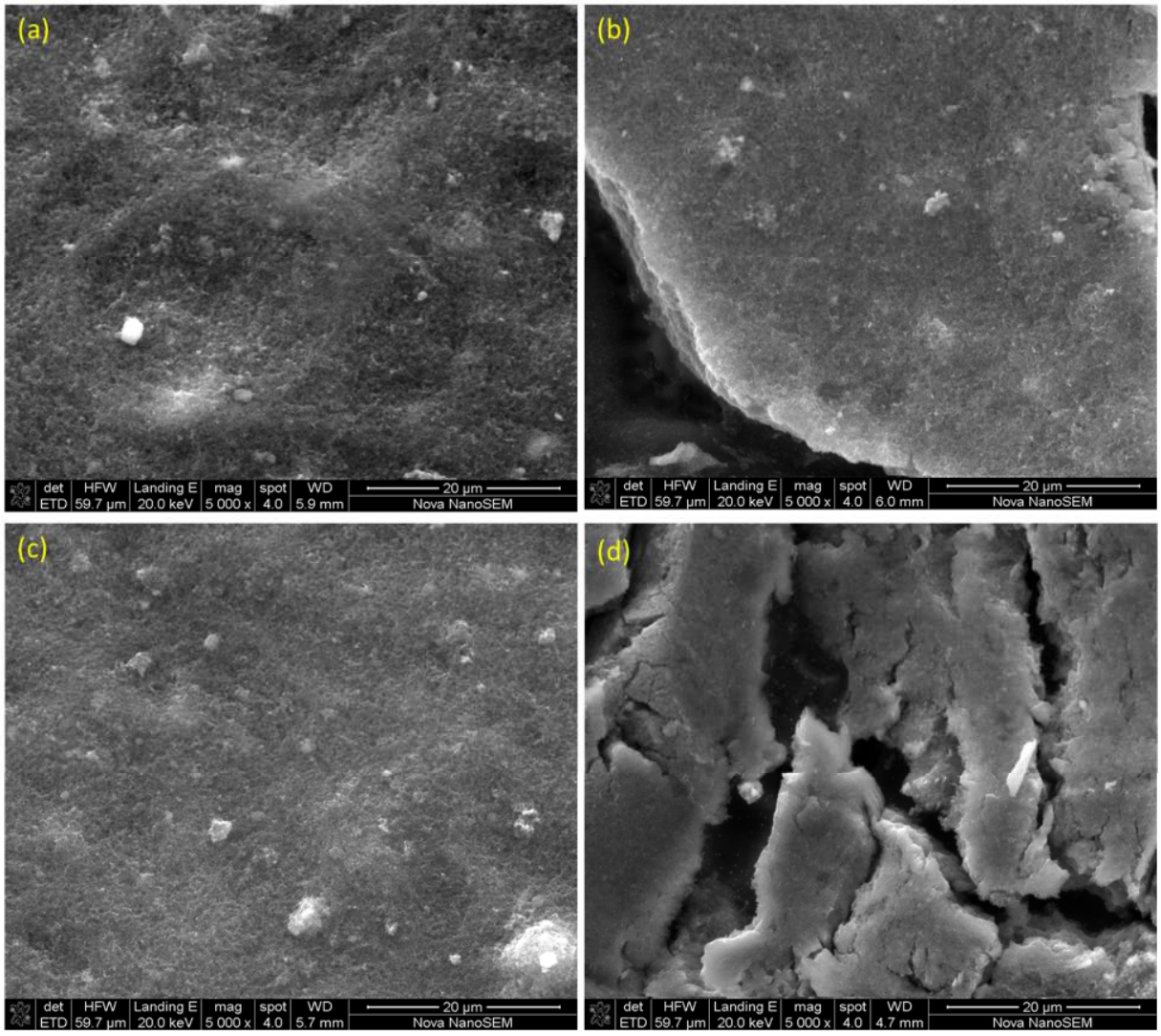

Figure 5.9. SEM images of the surface morphology for: (a) stratified MEA #6; (b) degraded stratified MEA #6; (c) monolayer MEA #2; (d) degraded non-stratified MEA #2. The images were taken at 5000 x magnification.

The appearance of cracks on MEA#2 in Figure 9 (d) is likely due to mechanical stresses imposed by membrane swelling (Kreitmeier et al., 2012; Solasi et al., 2007) which likely contributed to the decreased long-term durability of MEA#2.

5.7.2. Change in ECSA after carbon degradation

To examine the effect of electrochemical carbon corrosion on electrochemical surface area (ECSA), cyclic voltammetry was performed before and after the carbon corrosion test. The CVs showed a decrease in ECSA with progressive cycle number (Appendix: Figure 8.2). To compare the ECSA losses obtained in each MEA, the ECSA losses were normalized to its beginning-of-life (BoL) ECSA and the following equation was used:

$$\% \, ECSA \, loss = -\frac{ECSA_{BoL} - ECSA_{n-th\ cycle}}{ECSA_{BoL}} x\ 100 \quad (5\text{-}1)$$

Where $ECSA_{BoL}$ is the ECSA at Beginning of life, and $ECSA_{n\text{-}th\ cycle}$ is the measured ECSA after the n-th cycle. Figure 5.10 presents the percentage ECSA loss of each MEA versus the cycling period.

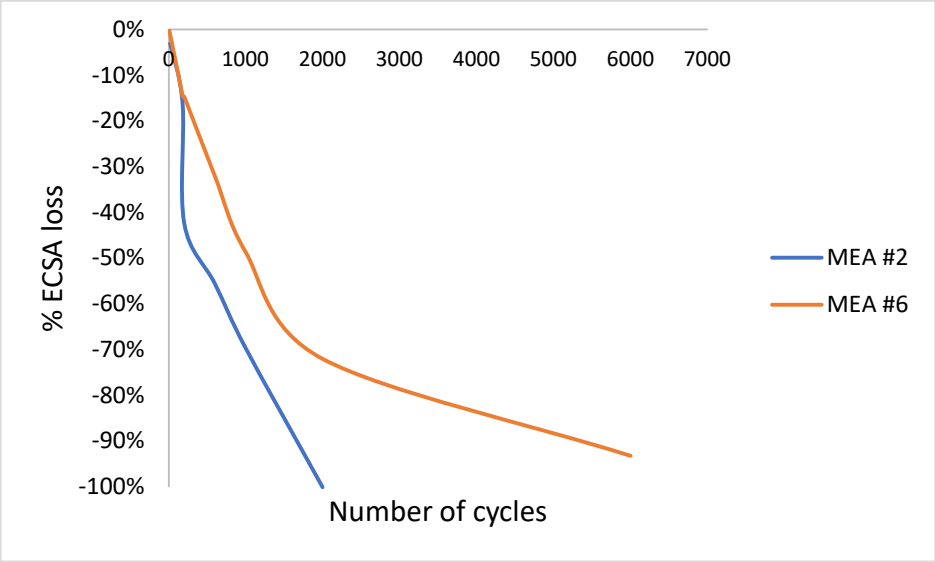

Figure 5.10. Degradation of the ECSA over time for a stratified MEA #6 and monolayer MEA #2, demonstrated as percentage ECSA loss during cycling.

The ECSA decreased over the degradation period due to carbon support corrosion and Pt dissolution. During electrochemical carbon corrosion, carbon is converted to CO_2 gas. As a result of the reduced carbon support area, Pt particles agglomerate or dislodge, leading to a decrease in Pt surface area (Oh et al., 2012). The MEAs experience similar losses from the 20-180 cycles and a drastic decrease (-42 %) is observed for MEA #2 after 200 cycles. The ECSA loss was 70 % for MEA #2 after 1000 cycles and only 49 % for MEA #6. After 2000 cycles, the ECSA could no longer be determined for MEA #2 due to severe CL degradation which resulted in high hydrogen crossover. This indicates that there was a higher platinum loss and level of degradation in MEA #2 compared to MEA #6.

5.7.3. Decrease in electrochemical performance

Air and hydrogen polarization curves were performed with 59 % RH on both anode and cathode, at periodic intervals during the degradation period. Figure 5.11 shows the performance curves of the stratified MEA #6 and monolayer MEA #2 over the degradation period. The initial performance of the

MEAs is comparable but their performance degradation is distinctive. The performance curves show a decrease in cell potential during potential cycling.

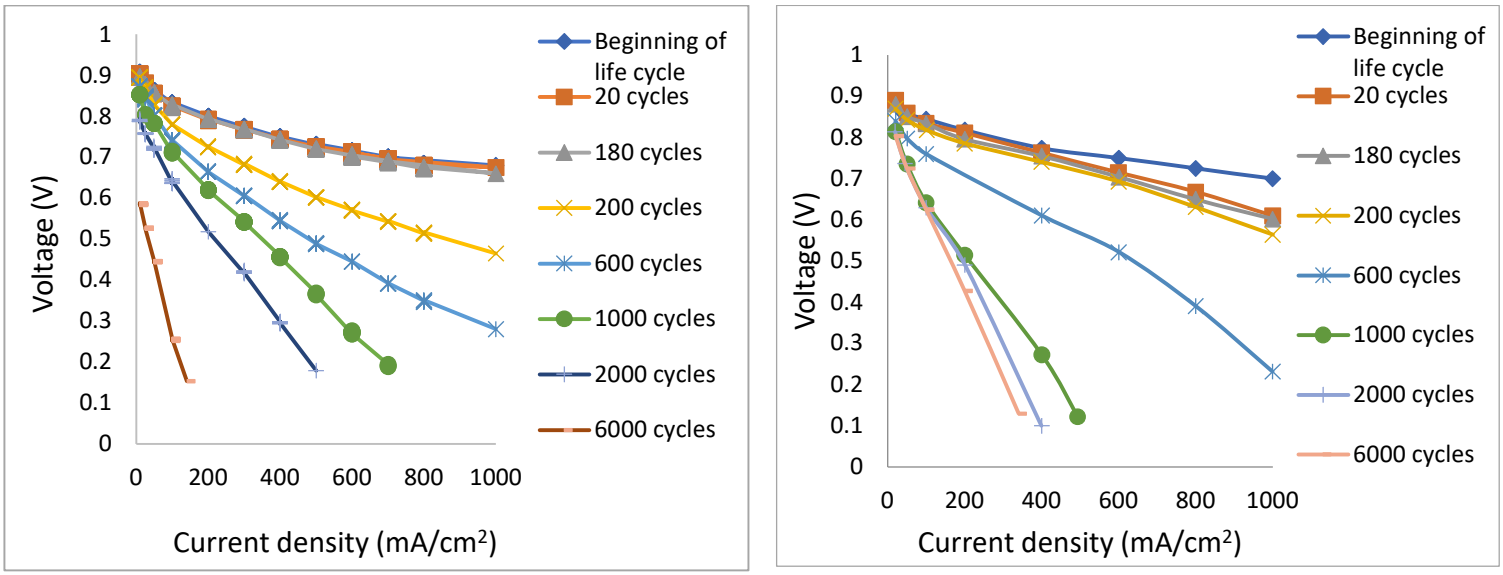

Figure 5.11. The change of I-V characteristics of: (a) monolayer MEA #2; (b) stratified MEA #6 during the carbon corrosion test.

MEA #2 experienced significant activation polarization losses after potential cycling compared to MEA #6. The OCV of MEA #6 decreased from 0.89-0.83 V and for MEA #2 from 0.89-0.585 V. These OCV losses can be correlated to increased hydrogen cross overs with membrane swelling (Vielstich et al., 2003) and Pt surface area losses during potential cycling. Figure 5.12 shows the change in potential measured at 400 mA/cm^2, for the stratified and non-stratified MEA. The decrease in output voltage is apparent with increasing current densities. The decrease in performance is due to the loss of Pt active area because of carbon corrosion. MEA #2 shows a significant drop in voltage on the 200th cycle while MEA #6 potential showed a significant decrease on the 600th cycle. Both MEAs exhibited a slow gradual decline of cell voltage in the last segments of potential cycles. After 6000 cycles, the maximum current density reached by MEA #6 was 580 mA/cm^2 while MEA #2 reached 380 mA/cm^2 which suggests more severe degradation of MEA #2.

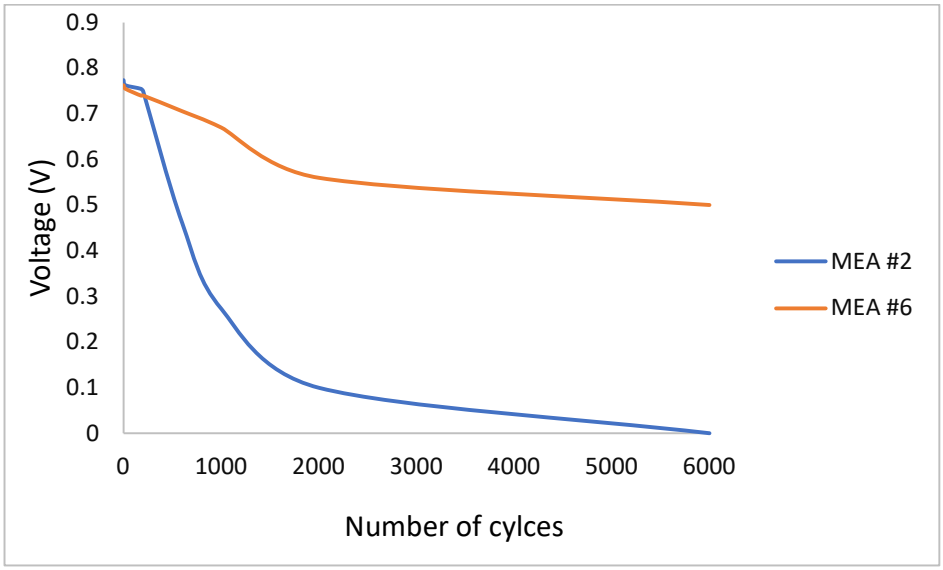

Figure 5.12. Voltage decay on MEAs during potential cycling determined at 400 mA/cm^2.

A sudden drop in potential was observed for MEA #2 after 200 cycles while MEA #6 voltage gradually decreased over time. Performance losses resulted from the mechanical degradation- CL surface cracking and delamination from the membrane. The performance degradation of MEA #2 suggests that the MEA suffered from severe physical degradation as observed in Figure 5.12, leading to voltage decay after 200 cycles.

The results of CL degradation, membrane cracking, reduced hydrogen adsorption loss, and performance loss show that MEA #2 suffered more severe degradation than MEA #6. This can be owed to the denser microstructure of the stratified MEA #6 and the higher ionomer content adjacent to the membrane which retained moisture closer to the membrane; superior heat dissipation which prevented membrane swelling and decreased mechanical stresses. The reduced ionomer coverage in the outer layer might have played a significant role in enhancing the durability of the MEA by improving mass transport. Comparing the durability of the MEAs (MEA #2& #6) after the carbon corrosion test, stratification increased the durability of the MEA CCL thickness by 15.51 %; ECSA degradation by 26.63 %; OCV by 27.53 %; and improved performance @0.4 mA/cm^2 by 50 %.

5.8. A summary of observations and findings

Stratified MEAs presented a significantly lower BET surface area and were less porous than monolayer MEAs with a denser catalyst layer (CL) structure. The polarization analysis demonstrated lower activation losses for the stratified MEAs under all RH conditions but higher mass transport losses owing to the

decreased CL porosity. The EIS fitting results demonstrated that stratified MEAs had significantly larger ohmic and charge transfer resistances compared to the benchmark 24 wt.% I at dry conditions which contributed to their low performance at these conditions. The largest ohmic and charge transfer resistances were experienced by the stratified MEA with 2:2 Pt loading ratio because it had increased 28 wt.% I thickness and thus elongated ionic transport pathways. This MEA demonstrated lower performance at higher RH conditions (60 – 100 %) compared to the benchmark MEA. The stratified MEA with 1:3 Pt loading ratio demonstrated (± 1 %) performance change at higher RH (60 - 100 %) compared to the benchmark monolayer MEA. The decreased BET surface area and porosity in stratified CCL MEAs are believed to have played a major role in increasing internal resistances, which in turn affected performance. To achieve the best ionomer gradient cathode catalyst layer (CCL), it is recommended that different ionomer gradients be evaluated for stratification.

CHAPTER 6

6. Reduction of Pt loading in the cathode catalyst layer for PEMFC

In this chapter, MEAs were prepared using a lower PGM loading (0.35 mg_{Pt}/cm^2) in the cathode catalyst layer (CCL). The CCL was prepared in a monolayer as well as a series of stratified ionomer layers. The various MEAs were physically characterized and their electrochemical performance was evaluated at various RH conditions (20-100 % RH) and compared to the benchmark monolayer MEA (MEA #2). A carbon corrosion study was carried out to compare the durability of the best performing low PGM stratified MEA to the low PGM monolayer MEA (MEA #12).

6.1. Design of the lower PGM MEAs with stratified ionomer layers

The Pt content was reduced in stratified cathode catalyst layers (CCLs). The Pt loading of the CCL was reduced from 0.4 mg_{Pt}/cm^2 to 0.35 mg_{Pt}/cm^2, while the anode Pt loading was kept constant at 0.1 mg_{Pt}/cm^2. For the stratified CCL MEAs, Pt loading was reduced by 0.05 mg_{Pt}/cm^2 either in the first or second layer of the stratified MEAs. Table 6.1 shows the Pt loading and varying ionomer contents of the lower PGM loading MEAs.

Table 6.1. Platinum loadings and ionomer contents of the reduced Pt and benchmark MEAs.

	Cathode Pt loading (mg_{Pt}/cm^2)		**Overall Cathode PGM loading (mg_{Pt}/cm^2)**	**Ionomer Content (wt.%)**	
	1st layer	2nd layer		1st layer	2nd layer
MEA #2	0.40	--	0.40	24	--
MEA #8	0.050	0.30	0.35	28	24
MEA #9	0.10	0.25	0.35	28	24
MEA #10	0.15	0.20	0.35	28	24
MEA #11	0.20	0.15	0.35	28	24
MEA #12	0.35	--	0.35	24	--

The thickness of the MEAs was measured using a thickness gauge before BET analysis and are given in Table 6.2.

Table 6.2. Average thicknesses of reduced Pt loading MEAs.

MEA	Thickness (mm)
MEA #2	0.05180
MEA #8	0.04200
MEA #9	0.04330
MEA #10	0.03700
MEA #11	0.03800
MEA #12	0.03067

The reduced Pt loading MEAs (MEA #8 -#12) were 16 - 40 % thinner than the monolayer MEA #2, due to decreased Pt loading. The stratified CCLs had different Pt/C-ionomer agglomerates due to their varying Pt/C to ionomer ratios- MEAs with more 28 wt.% I loading (MEA #10 & #11) were thinner than those with more 24 wt.% I (MEA #8 & #9). Likely, the agglomerates of the 28wt% ionomer content MEAs were closely packed together and yielded a dense, thin CL structure.

6.2. Bet analysis

Table 6.3 shows that the BET surface area varies with ionomer loading. The stratified MEAs yielded a lower BET surface area and porosity than the monolayer MEA #12, as previously observed in Chapter 5. Although MEA #2 and #12 had the same ionomer loading, MEA #12 had a significantly larger porosity than MEA #2 because of its decreased Pt loading. Decreasing the Pt loading causes the void fraction and solid ionomer contact to decrease (Srinivasarao et al., 2010), and therefore increases the surface area. The BET surface area of the stratified MEAs decreased with the thickness of the first layer containing 28wt% ionomer or with decreasing thickness of the second layer containing 24wt% ionomer. Increasing the size of the 28wt% ionomer layer, increased the overall ionomer coverage and formation of larger agglomerates, subsequently decreasing the surface area in the CL.

Table 6.3. Pore characteristics of the lower PGM loading MEAs.

MEA	Bulk density (g/cm^3)	Cumulative pore volume (cm^3/g)	BET surface area (m^2/g)	% Porosity
MEA #2	0.8157	0.1443	70.18	11.77
MEA #8	1.002	0.09620	67.27	9.640
MEA #9	0.9566	0.1867	57.77	17.89
MEA #10	1.141	0.04209	54.50	4.800
MEA #11	1.111	0.09623	47.22	10.68
MEA #12	1.413	0.2331	70.43	32.94

6.3. Electrochemical surface area

The electrochemical surface areas (ECSAs) of the lower Pt MEAs were calculated from the hydrogen adsorption peaks in the cycling voltammograms for increasing RH. Figure 6.1. presents the ECSAs of the reduced Pt loading MEAs which are compared to the benchmark monolayer MEA #2.

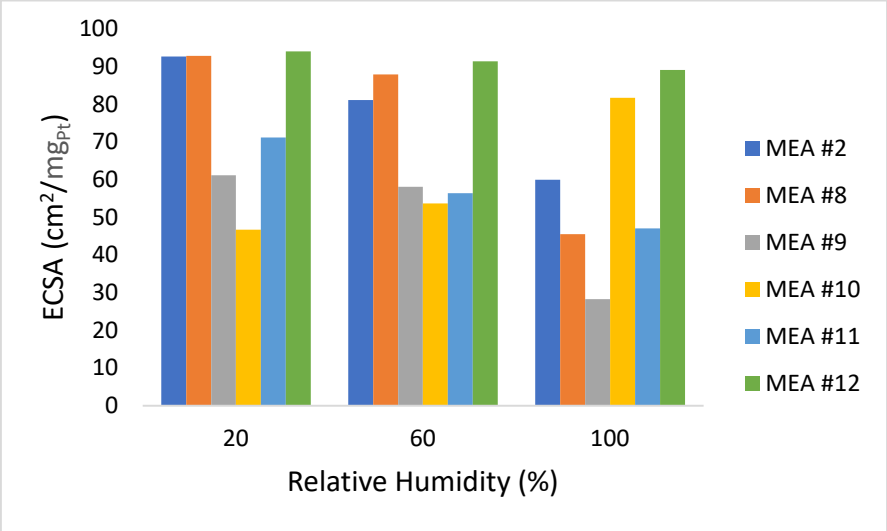

Figure 6.1. The ECSAs for the reduced Pt MEAs and the benchmark MEA#2 determined at 20- 100 % RH.

The reduced CL monolayer MEA #12 demonstrated the largest and most consistent ECSAs under all RH conditions, owing to its highly porous agglomerate structure which exposed Pt active sites. For similar reasons, the stratified CCL MEA with the largest BET surface area and more 24 wt.% I loading (MEA #8) demonstrated larger ECSAs from 20-60 % RH conditions. The ECSA of the stratified MEAs decreased with

increasing thickness of the first layer. This is likely due to higher ionomer coverage also shown with decreasing BET surface area. However, at 100 % RH the ECSA was significantly larger for the low porosity MEA #10 compared to other stratified MEAs. Notably, only the ECSA of MEA #10 increased with RH while the others decreased with RH. The increase of ECSA with RH was also reported by Fan et al. (2019) who mainly attributed this trend to the improved contact area between Pt particles and water domains instead of the formation of new transport paths. The low porosity and denser agglomerate structure of MEA #10 could have played a role in increasing the contact area between water domains and Pt aggregates.

6.4. Performance curves

To investigate the influence of reducing Pt loading in stratified layers on the electrical performance of an MEA, the polarization curves obtained for the stratified reduced Pt loading MEAs were compared to the benchmark monolayer MEA #2. The polarization curves are presented in Figure 6.2. The stratified CCL reduced Pt loading MEAs performed better than the reduced Pt loading monolayer MEA #12. This performance improvement is attributed to the effect of the higher ionomer loading in the first layer which increased proton conductivity; and a lower ionomer loading in the second layer which reduced mass transport losses (Srinivasarao et al., 2010; Shahgaldi et al., 2018). At low current densities (200 mA/cm^2 and lower), the activation losses of monolayer MEA #12 were higher than stratified MEAs. Lower activation losses for stratified MEAs were also observed in Chapter 5 and it was attributed to higher ionomer content in the stratified MEAs. At intermediate current density (200-800 mA/cm^2), the ohmic losses of stratified MEAs were comparable to MEA #2.

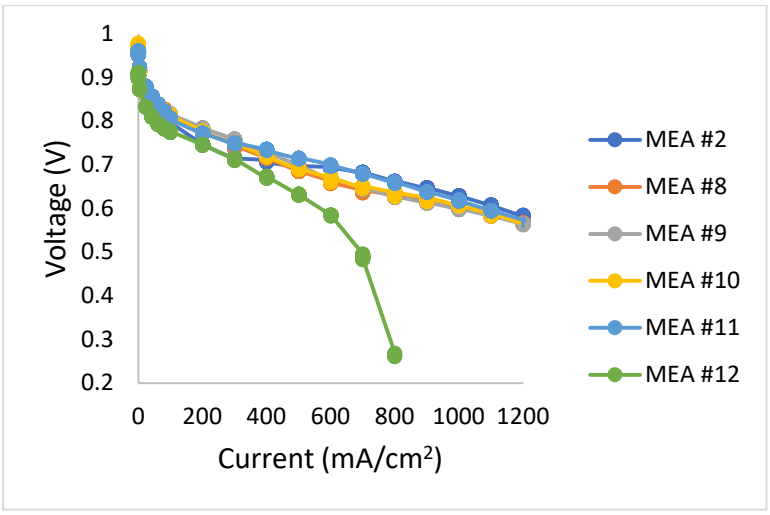

(**a**)

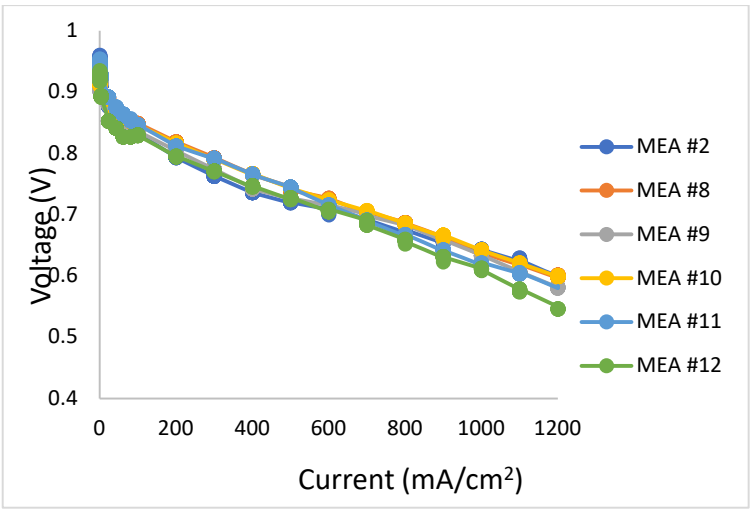

(**b**)

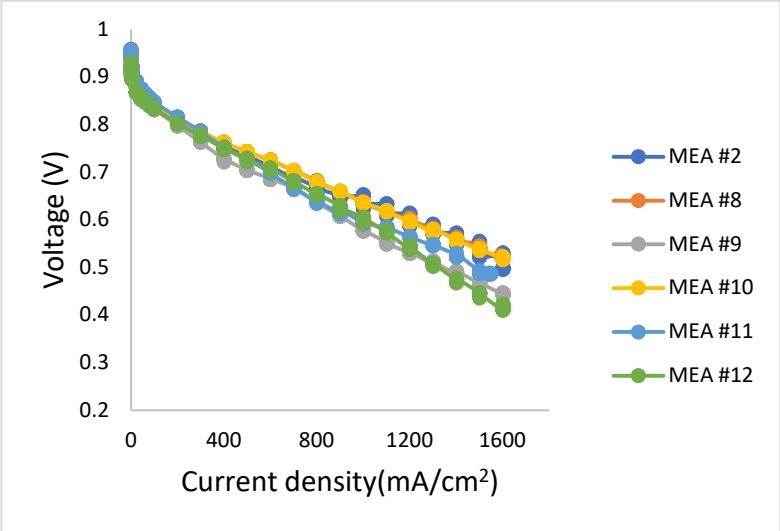

(c)

Figure 6.2. Polarization curves for stratified MEA with CCL loading fixed at 0,35 mg_{Pt}/cm^2 obtained for: (a) 20 % RH; (b) 60 % RH; (c) 100 % RH.

At dry conditions, the performance of stratified MEAs improved with increasing thickness of the 28 wt.% I layer. MEA #11, which had the thickest 28 wt.% I layer, demonstrated superior performance owing to its higher proton conductivity. MEA #8 and #10 performed better than MEA #9 and #11 under all studied RH conditions which could be related to their I/C ratio. From medium to high current densities, the voltage drop was greater for MEA #12 under all RH conditions due to increased ionic transport resistances, which limited its performance. At high current densities, MEA #9 and #11 experienced higher voltage losses. These MEAs do not have an optimized I/C ratio for optimal ionic and mass transport. Figure 6.3 compares the OCVs of the MEAs with reduced Pt loading.

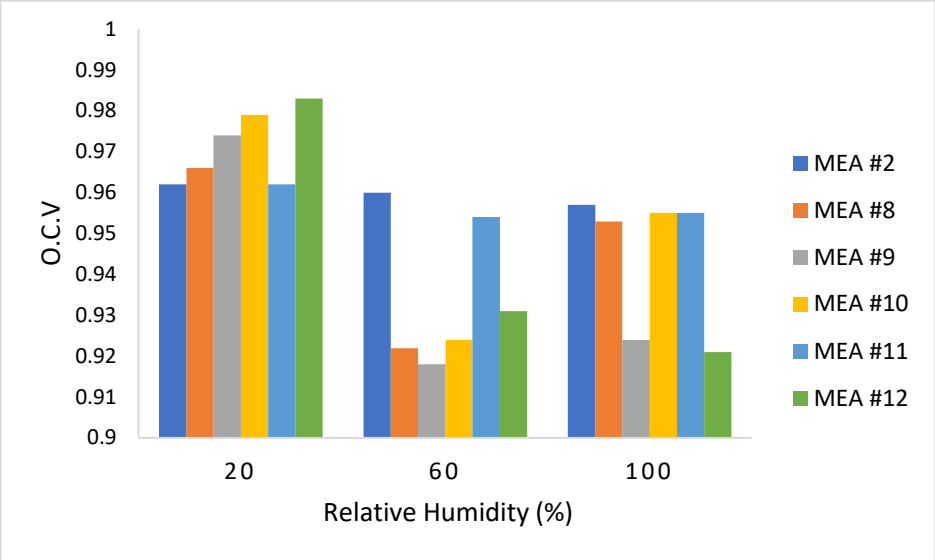

Figure 6.3. Open circuit voltages (OCV) for the reduced Pt loading MEAs (MEA #8- #12) and benchmark MEA #2, under 20 %, 60 % and 100% RH conditions.

A similar OCV trend was observed in Chapter 4 and 5 in which the highest OCVs were achieved at dry conditions due to lower hydrogen cross overs at low RH (Francia et al., 2011; Bail et al., 2013). From 60-100 % RH conditions, MEA #12 demonstrated lower OCVs than MEA #2. It had the same ionomer loading yet lower Pt loading and thus a reduced effective charge. MEA #11, with a thicker layer of 28 wt.% ionomer loading, had more stable OCVs throughout the different RH conditions. MEA #9 had the lowest OCVs which can be related to its low ECSAs. Figure 6.4 compares the performances of the lower Pt loading MEAs (MEA #8-#12) determined at 0.65V with the benchmark MEA (MEA #2) with 0.4 mg_{Pt}/cm^2 Pt loading.

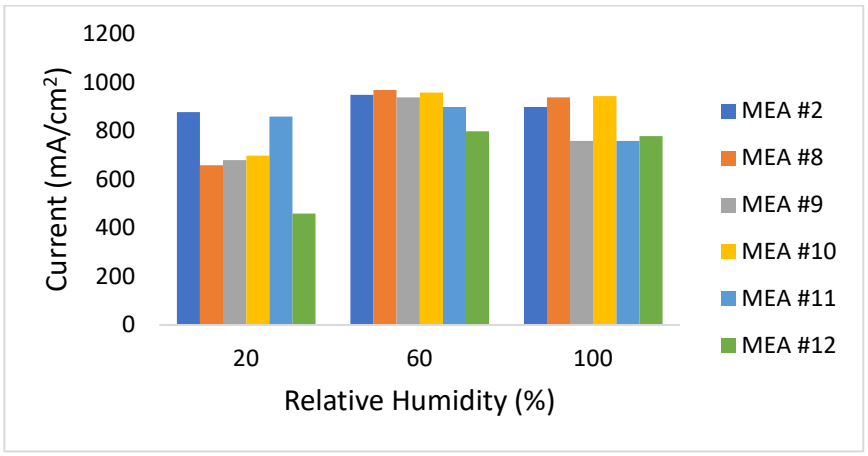

Figure 6.4. Current density of the reduced Pt loading MEAs (MEA # 8 - #12) and benchmark MEA #2 are compared at 0.65 V, with feed gases humidified from 20 %-100% RH.

The performance results displayed the same trend as Chapter 4 and 5, showing an increase in performance with increasing RH and a slight decrease at fully humidified conditions. At dry conditions, MEA #12 demonstrated very low performance, only achieving 52.27 % of MEA #2's performance. The Pt utilization may have dropped significantly for the low Pt content 24 wt.% MEA because the I/C ratio deviates from the optimum value (Wei et al., 2006). The performance of the stratified MEAs decreased with a decrease in the first layer thickness. Higher ionomer loading is crucial for decreasing ionic resistances at dry conditions. When the RH is increased, the ionomer absorbs moisture and elongate ionic paths. Higher ionomer loading means more hydrophilic zones and greater ionomer swelling, which increases charge transfer resistances at higher RH. As a result, when the RH increased, MEAs with more 24 wt.% I loading became favorable as they demonstrated better performance. Generally, the performance of the reduced Pt loading MEAs was comparable to the benchmark monolayer MEA #2. The performance data shows that it is possible to reduce Pt loading by 12% and still achieve similar benchmark performance under various RH conditions. Sasikumar et al. (2004) studied the dependence of ionomer content on Pt loading and it was found that that the optimal ionomer content depends on the Pt loading. This study confirmed that the performance depends on the I/C loading ratio. The MEA with Pt ratio= 1:6 (0.05 1st layer and 0.3 2nd layer) gave the best performance at higher RH and the one with 1:0.75 (0.15 1st layer and 0.2 2nd layer) ratio performed best at dry conditions.

Although there was no improvement observed for stratification in Chapter 5, in which the optimized ionomer contents established in Chapter 4 were used, stratification of a lower PGM CCL resulted in higher performance. This shows that stratification strongly depends on the Pt-C/I ratio between the layers of the CL.

6.5. EIS analysis

To understand the performance of the reduced Pt loading MEAs (MEA #8 - #11), EIS was used to evaluate the key resistances. The EIS study was conducted at 0.5 A/cm^2. Nyquist plots are presented in Figure 6.5. A significant difference in ohmic resistances was demonstrated under 20 % RH. As the RH increased, the ohmic resistances also decreased which is the same trend demonstrated in Chapter 4 and 5. As seen in Chapter 5, an increase in charge transfer resistances was observed for the stratified MEAs under the studied RH conditions. Increased mass transport and charge transfer resistances result from the thicker ionomer films hindering mass transport and elongating charge transfer pathways, in the high ionomer loading stratified MEAs. The performance losses demonstrated by mass transport and charge transfer

resistance arcs corelated with the polarization performance curves. Under dry conditions, MEA #11 demonstrated the least mass transport and charge transfer resistances which corelated to its higher performance under these conditions; MEA #8 and MEA #10 had similar resistances under all RH conditions and hence their similar performance; and the largest resistances were demonstrated by MEA #9 resulting in its poor performance under the studied RH conditions.

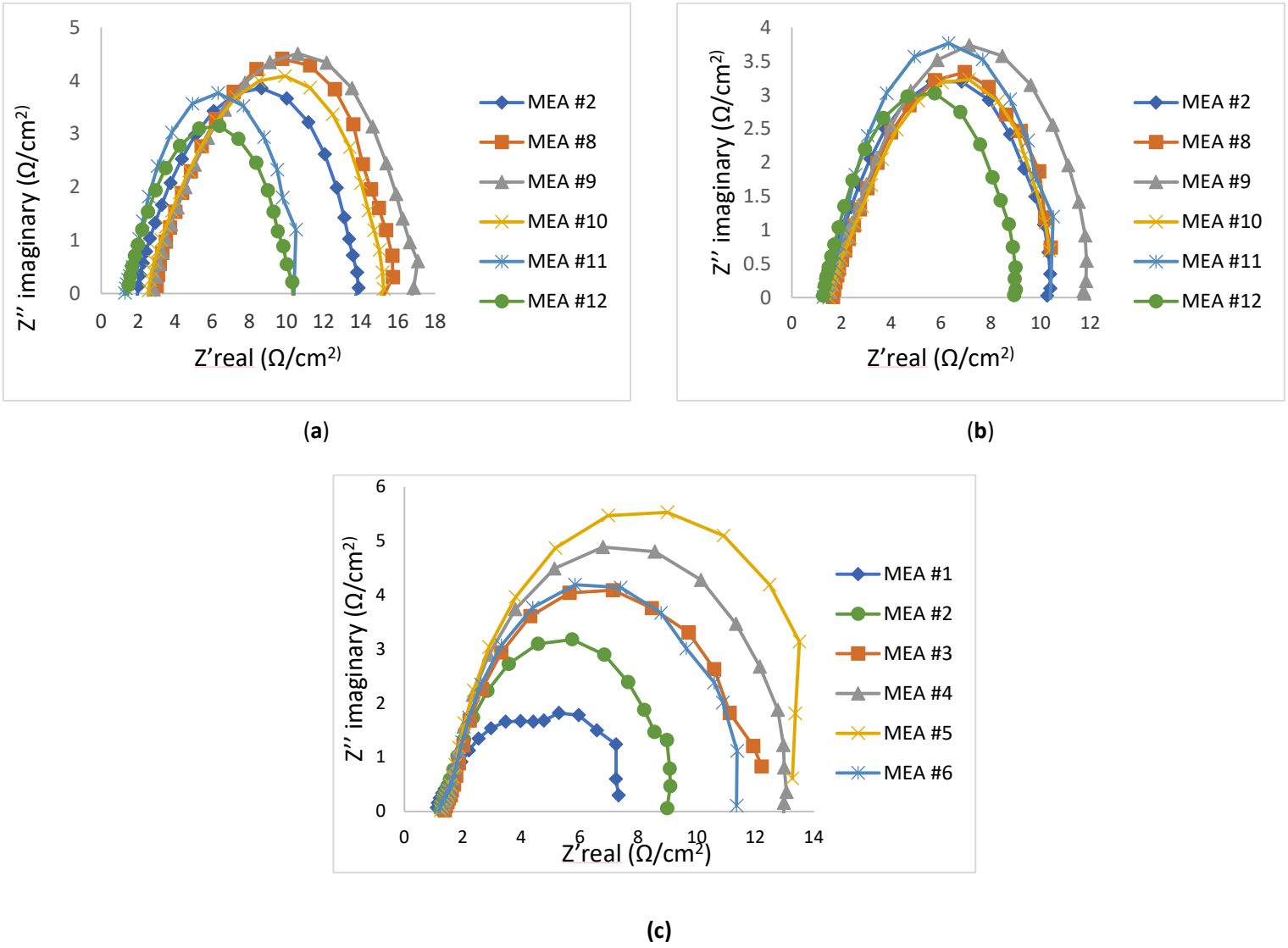

Figure 6.5. Nyquist plots of benchmark monolayer MEA (MEA #2) and reduced Pt loading MEAs (MEA #8- #12), under: (a) 20 %, (b) 60 % and (c) 100 % RH.

The Nyquist plots were fitted in the equivalent design circuit used in Chapter 4: Figure 4.7. The results of the Randles fitting parameters are shown in Table 6.4. R1 is the ohmic resistance, and R2 is the electron

transfer resistance; Warburg impedance (Ws1) represents the mass transfer resistance; and a constant phase element (CPE) was associated with the double layer capacitance on the electrode surface.

Table 6.4. Results of the fitting parameters obtained from the Randles equivalent circuit model.

		MEA #2	MEA #8	MEA#9	MEA #10	MEA #11	MEA #12
R1 (Ωcm^2)	20 % RH	2.019	2.748	2.854	2.683	1.328	1.759
	60 % RH	1.325	1.655	1.560	1.253	1.263	1.600
	100 % RH	1.115	1.438	1.334	1.320	1.336	1.560
R2 (Ωcm^2)	20 % RH	10.56	9.004	8.561	8.090	7.146	8.157
	60 % RH	5.873	6.712	6.503	7.274	7.339	6.278
	100 % RH	6.004	7.565	7.788	7.339	7.177	6.228

Ohmic resistances R1- The ohmic resistance decreased with increasing RH for all MEAs due to increasing proton conductivity in the CL at wetter conditions. In stratified MEAs, ohmic resistances decreased with increasing thickness of the first layer. Increasing the thickness of first layer increased proton conductivity and thus reduced ohmic resistances. MEA #12 exhibited larger ohmic resistances at 60-100 % RH contributing to its poor performance. This means that the 24 wt.% I loading is not sufficient for 0.35 mg_{Pt}/cm^2 loading; a higher ionomer loading is required.

Charge transfer resistances R2- The charge transfer resistances demonstrated the same trend as in Chapter 4 and 5: charge transfer resistances were largest at 20 % RH; decreasing with increased RH and slightly increased at fully humidified conditions. At 20 % RH, stratified MEAs demonstrated lower charge transfer resistances compared to the monolayer MEAs (MEA #2 & #12) due to increased ionomer loading in the first layer. However, as the RH was increased charge transfer resistances were significantly lower for the benchmark MEA #2 than reduced Pt content MEAs because it had a higher Pt loading which increased ORR kinetics. Increasing ionomer loading increases proton conductivity at the expense of electronic conductivity because it increases the electron path length- increasing charge transfer resistances. Notably, at dry conditions MEAs with more 28 wt.% I loading (MEA #10 and #11) demonstrated lower charge transfer resistances than those with more 24 wt.% I (MEA #8 and #9). High ionomer loading is beneficial for reducing charge transfer resistances at dry conditions as seen in Chapter 4. However, when RH was increased MEAs with more 24 wt.% I loading had lower charge transfer resistances. The same effect was observed in Chapter 4 for higher loading MEAs and it was attributed to the effect of ionomer swelling which increases with RH and covers electrochemical conductive areas- decreasing electron transport flux. Therefore, having a stratified MEA with more 28 wt.% I loading is

optimal for dry conditions and a stratified MEA with more 24 wt.% I loading is ideal for higher RH conditions.

6.6. Radar chart analysis

The radar charts in Figure 6.6 were used to compare the performance of reduced Pt loading MEAs (MEA #8- #12) to the benchmark MEA (MEA #2). The analysis was confined to the same parameters and benchmarks used in Chapter 4: (1) 4 Ωcm^2 and 0.8 Ωcm^2, charge transfer and ohmic resistances respectively; (2) ECSA, 100 mg_{Pt}/cm^2; (3) OCV, 1 V; (4) Performance at 0.65 V, 1.5 A/cm^2.

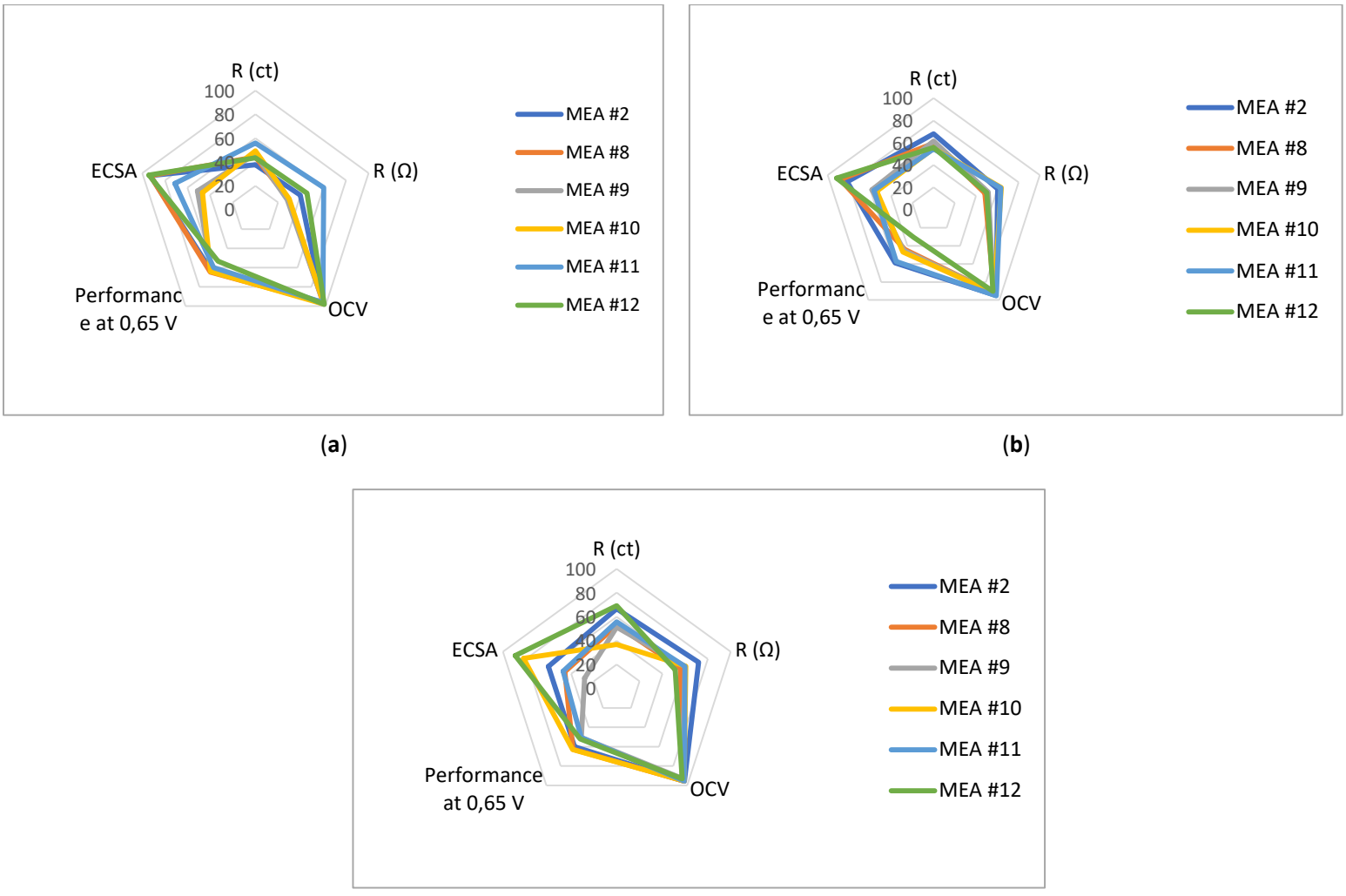

Figure 6.6. A radar chart analysis comparing the performance of benchmark monolayer MEA (MEA #2) to reduced Pt loading MEAs (MEA #8- #12) at: (a) 20 %; (b) 60 %; (c) 100 % RH.

The reduced Pt loading monolayer MEA (MEA #12) showed the least capability in meeting performance targets compared to the reduced Pt loading stratified CCL MEAs (MEA #8- #11). The reduced Pt loading stratified CCL MEAs were able to meet the performance standards of benchmark MEA #2. This shows that it is possible to reduce MEA Pt loading by 12 % and still achieve similar performance standards as the standard benchmark MEA #2. Among the reduced Pt loading MEAs, MEA #11 had a more consistent performance under different RH conditions, but MEA #8 was the closest to achieving the targets. This means that the I/C ratio of MEA #8 is optimal for increasing Pt utilization in the stratified CCLs and thus increasing performance.

6.7. Durability comparison of reduced Pt loading MEAs

While the stratified reduced Pt loading MEAs performed better than the monolayer MEA #12, the durability of these stratified MEAs needs to be established. Therefore, a carbon degradation test was performed to compare the durability of the reduced Pt loading stratified MEA with monolayer MEA #12. MEA #11, which was more consistent in reaching performance targets under the studied RH conditions, was selected for the degradation test. Figure 6.7 shows the SEM images of the MEAs before and after carbon degradation testing.

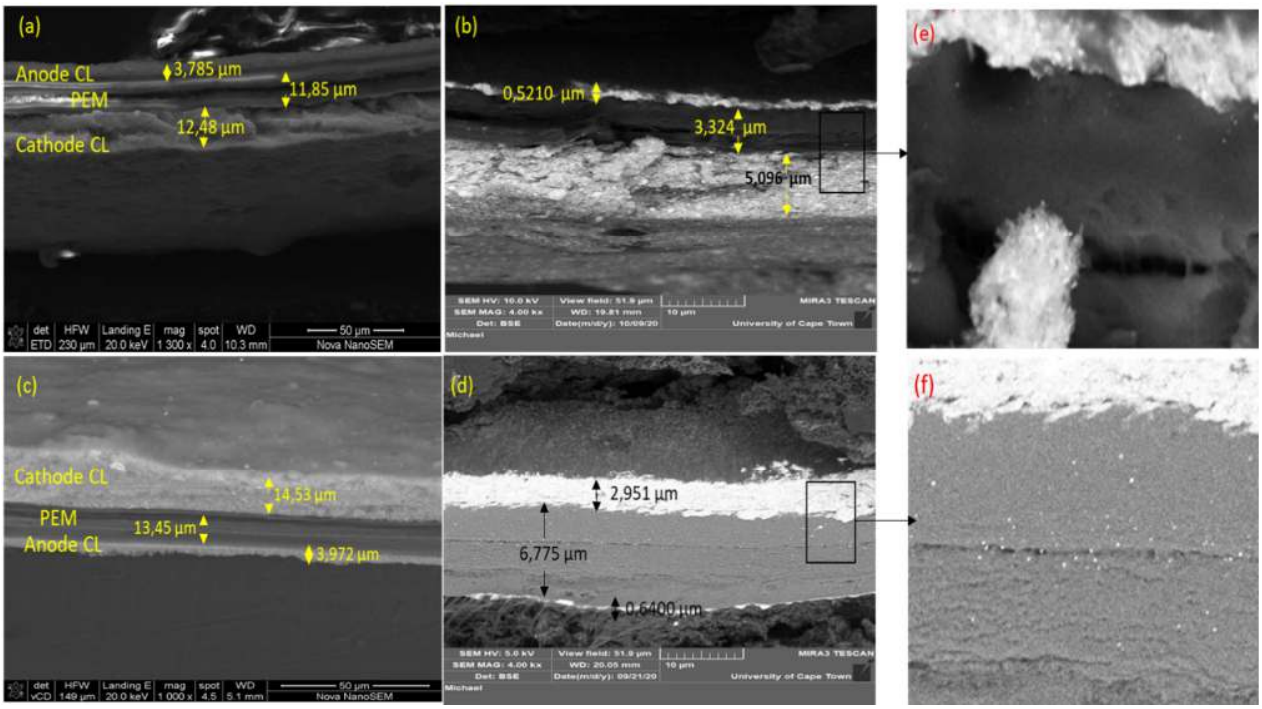

Figure 6.7. SEM cross-sectional imaging for: (a) MEA #12 before carbon degradation; (b) MEA #12 after carbon degradation; (c) MEA #11 before carbon degradation; (d) MEA #11 after carbon degradation. A magnified image of degraded PEM showing Pt dissolution from the CL to the PEM for: (e) MEA #12; (f) MEA #11.

MEA #12 CCL is 19.29 % thinner than MEA #11 before the degradation test. This is owing to the thick 28wt% ionomer layer on the inner layer of MEA #11. Thinning of both the anode and cathode CLs due to carbon support oxidation was observed for both MEAs. After the degradation test, the thickness of the stratified CCL was reduced by 79.69 %, while the monolayer CCL thickness was reduced by 59.16 %. The anode CL thinned by 83.88 % for the stratified MEA and 86.55 % for the monolayer MEA. Thinning of the PEM membrane resulting from thermal and chemical degradation of the membrane was observed for both MEAs after the degradation test which causes both gas crossover and electrical shortening (Sethuraman et al., 2008; Zhang et al; 2009; Jourdan et al., 2014). PEM thickness decreased by 49.61 % for MEA #11 and 71.93 % for MEA #12. Sethruman et al. (2008) showed that inadequate water content and high temperature accelerate membrane thinning. Therefore, the high ionomer loading adjacent to the membrane of the stratified MEA #11 is believed to have played a role in reducing PEM degradation by retaining moisture closer to the PEM and improving heat dissipation. The MEA thicknesses are summarized in Table 6.5. The pristine MEAs used for SEM imaging were not the same MEAs used for testing- the CL thicknesses might vary because of inconsistencies during manufacturing inherent to the

production process. Therefore, the difference in thicknesses of MEAs before and after degradation can only serve as an estimation of catalyst layer integrity.

Table 6.5. Thickness of lower Pt loading MEAs before and after the carbon degradation test.

		Thickness before degradation (µm)	Thickness after degradation (µm)
MEA #12	CCL	12.478	5.096
	Membrane	11.845	3.324
	Anode	3.875	0.5210
MEA #11	CCL	14.534	2.951
	Membrane	13.466	6.785
	Anode	3.972	0.6400

The Pt/C, ionomer, and PEM all comprise the mechanical strength of an MEA. Decreasing any of these materials decreases the mechanical strength of an MEA. Hence, the degradation of the CLs and PEM was greater for the reduced Pt loading MEAs compared to the higher Pt loading MEAs in Chapter 5. For the higher Pt loading MEAs in Chapter 5, monolayer MEA #2 showed a loss of 1.72 % and 54.32 % for the anode and cathode CLs, respectively. Meanwhile, the stratified CCL MEA #6 showed a loss of 11.72 % and 39.22 % for the respective anode and cathode CLs. Notably, after electrochemical carbon degradation low Pt loading MEAs (MEA #11 and #12) experienced membrane dehydration/thinning while higher Pt loading MEAs in Chapter 5 experienced membrane swelling. This suggests that the amount of Pt dissolution was higher for reduced Pt loading MEAs (MEA #11 and #12) during accelerated tests which caused the formation of Pt oxides, leading to chemical degradation of the PEM. Pt dissolution was only observed on the edges of the membrane on higher Pt loading MEAs but it can be seen across the membrane of MEA #11 in Figure 6.7 (e). Pt aggregates can be observed as white particles on the PEM shown in Figure 6.7 (e) and (f) which suggests that Pt detached from the carbon support due to corrosion. Pt dissolution appears greater for MEA #11 than MEA #12. Pt in the membrane is electronically and ionically isolated and cannot be accessed by gas reactants which leads to electrical performance degradation (Dubau et al., 2014). Figure 6.7 (c) and (d) show a thinner CL structure of MEA #11 and #12 which verifies collapsing of the CL structure because of severe carbon degradation.

6.7.1. Comparison of ECSA before and after potential cycling

The loss of Pt was evaluated periodically during the carbon degradation test, to examine the effect of electrochemical carbon corrosion on ECSA. Equation (5-1) was used to compare ECSA losses during potential cycling. The comparison of ECSA during potential cycling in Figure 6.8 shows that there was

accelerated decay in the ECSA of MEA #12 compared to MEA #11. ECSA decay in both MEAs was caused by Pt loss due to carbon support degradation. Electrochemical carbon corrosion decreased the amount of carbon available for Pt loading, which forced the Pt nanoparticles to migrate on the carbon surface and aggregate at relatively stable sites (Jang & Kim, 2010).

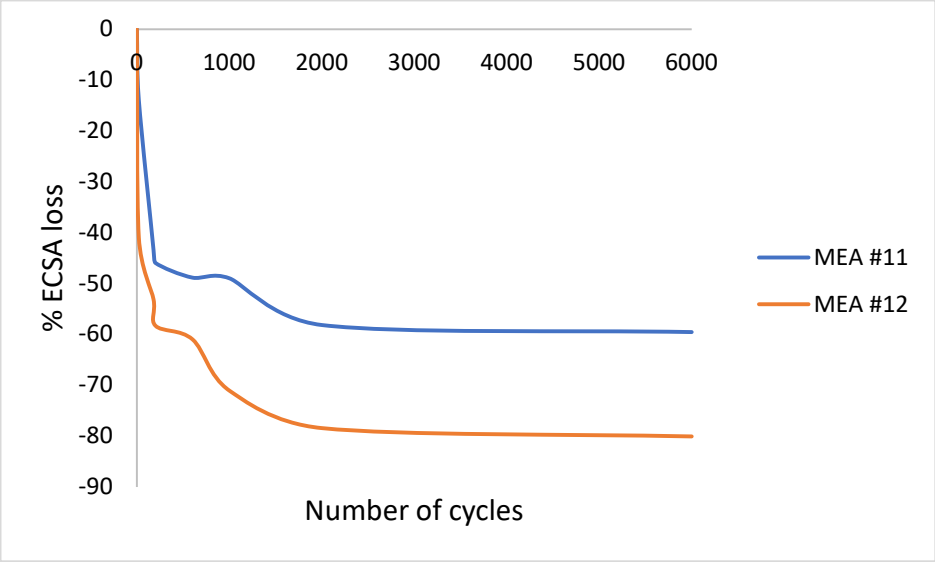

Figure 6.8. Percentage ECSA loss of MEA #11 and MEA #12 during potential cycling.

Although it appears in Figures 6.7 (d) and (e) that MEA #11 experienced more Pt dissolution and CCL disintegration, the ECSA of MEA #12 decreased significantly faster than MEA #11 having a total loss of 80 % after 6000 cycles compared to only 59 % for MEA #11. The extensive loss of ECSA in MEA #12 results from a drastic PEM degradation as observed in Figure 6.7 (b), which possibly increased hydrogen crossover. A study by Zhang et al. (2014) showed that hydrogen crossover increases with a decrease in membrane thickness. It is noteworthy that the ECSA loss of lower Pt loading MEAs (MEA #11 and #12) was less than high Pt loading MEAs (MEA #2 and #6) in Chapter 5. The increase in ECSA degradation with Pt loading was also reported by Speder et al. (2016). The high Pt loading monolayer MEA#2 in Chapter 5 reached a 100 % ECSA loss after only 2000 cycles while the high Pt loading stratified MEA #6 reached 93 % loss after 6000 cycles.

6.7.2. Performance loss over time

The change in electrochemical performance during potential cycling was studied. Air and hydrogen polarization curves were performed with 59 % RH on both anode and cathode, at periodic intervals during the degradation period. Figure 6.9 shows the performance curves of the reduced Pt loading stratified MEA

#11 and monolayer MEA #12 over the degradation period. The performance curves show a decrease in cell potential after every following potential cycling.

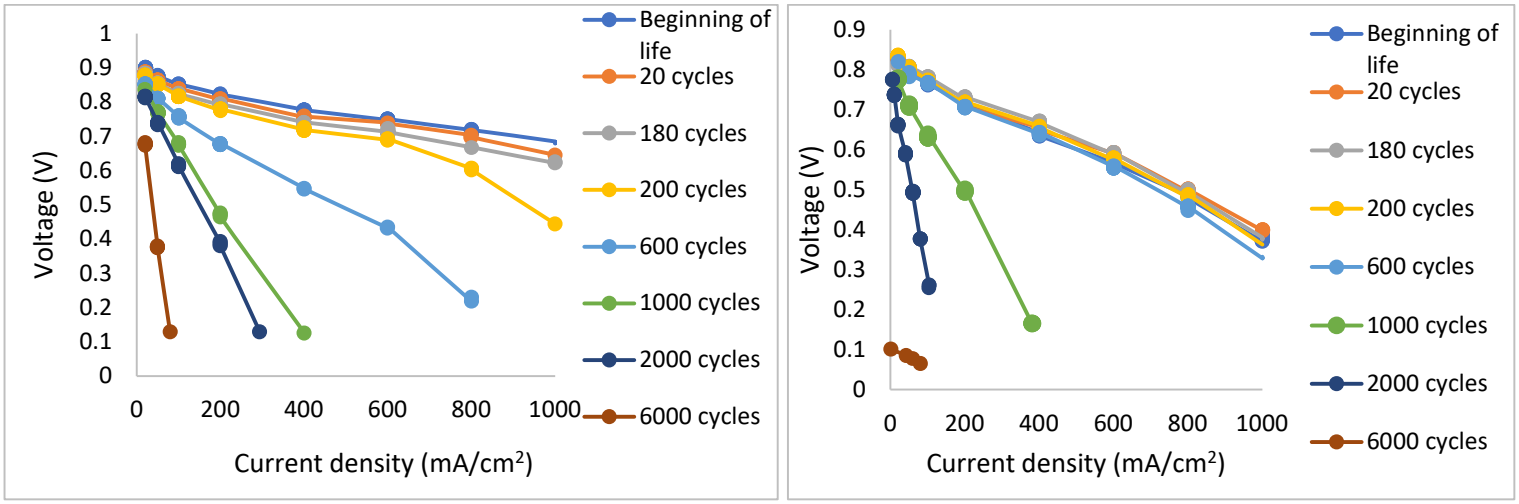

Figure 6.9. Performance curves taken during potential cycling for a reduced Pt loading: (a) monolayer MEA #12; (b) Stratified MEA #11.

The output voltage decreased from the low to the high current density region with progressive cycling due to CL morphology changes caused by carbon degradation, mainly ECSA loss due to particle agglomeration and CL thinning. The degradation of carbon and CL thinning reduces electron conduction in the Pt/C phase, contributing to ohmic losses. As the PEM degrades, it loses its proton conductivity and ionic transport resistances increase, limiting performance. Also, CL surface roughening due to carbon corrosion makes the CL hydrophilic and adds oxides groups resulting in oxygen diffusion and water management challenges, which drastically affects performance (Spernjak et al., 2012; Park et al., 2012). The OCV of MEA #12 drastically decreased after 6000 cycles from 0.83-0.101 V whereas MEA #11 OCV decreased from 0.910-0.680 V. This is mainly because MEA #12 had more Pt loss than MEA #12 which decreased its ECSA and consequently decreased the OCV.

To compare the performance losses obtained in each MEA, the voltage losses were normalized to its beginning-of-life (BoL) cell voltage and the following equation was used (Dhanushkodi et al., 2013):

$$\%\ Performance\ loss = \frac{V_{BoL} - V_{n-th\ cycle}}{V_{BoL}} x\ 100 \qquad (6\text{-}1)$$

Where V_{BoL} is the cell voltage at Beginning of life, and $V_{n\text{-th cycle}}$ is the voltage after the n-th cycle. Figure 6.10 presents the percentage performance loss of each MEA versus the cycling period. The voltage loss was measured at 200 mA/cm^2 and the corresponding results are shown in Figure 6.10.

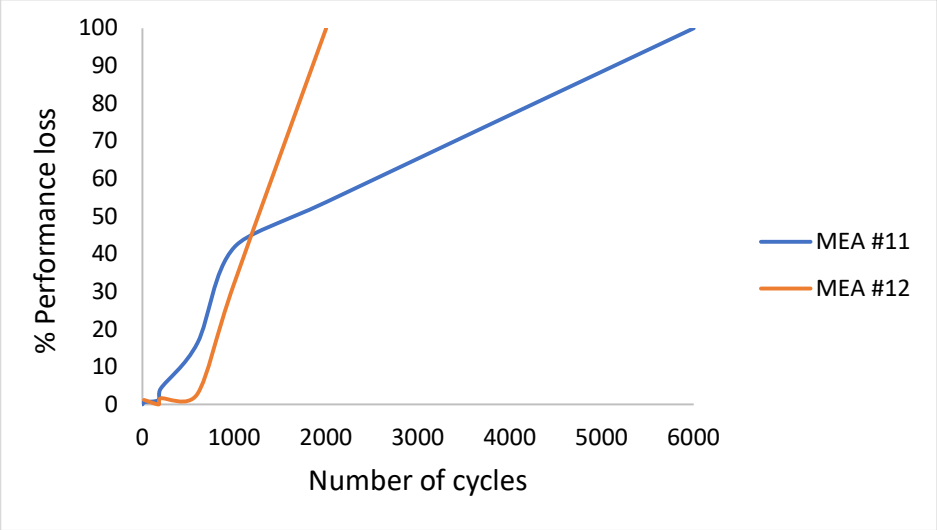

Figure 6.10. Percentage performance loss of MEAs after carbon degradation, measured at 200 mA/cm^2.

Performance loss begins to increase sharply after 1000 cycles for both MEAs. At 2000 cycles, MEA #12 had already reached a 100 % performance loss while MEA #11 demonstrated 48 % loss. The performance loss of MEA #12 can be attributed to its extensive ECSA loss. MEA #12 was considerably more stable during the first cycles, likely due to its low ionomer content which decreased the amount of water in the CL. However, as potential cycles progressed, MEA #12 experienced accelerated ECSA losses eventually leading to complete MEA failure.

Performance degradation was substantial for both the monolayer and stratified CCL MEA, but the degradation of CL after prolonged corrosion was lower in the MEA with stratified CCL. This was corroborated by higher ECSA; lower kinetic, ohmic, and OCV losses after carbon degradation. The high ionomer coverage in the first layer of MEA #11 appears to have reduced carbon corrosion by retaining moisture closer to the membrane, preventing severe membrane dryness which causes PEM degradation. The bilayer interface also played a role in enhancing the durability of the MEA by disrupting the rate of mass transport during carbon degradation test, reducing the carbon corrosion rate. MEA #11 showed an increased OCV of 62.55 %, ECSA of 20.55 % and performance loss @200 mA/cm^2 of 46.18 % compared to the monolayer MEA#12.

6.8. A summary of findings and observations

This study has proven that using ionomer stratification to decrease the Pt loading in an MEA yields better performance compared to the monolayer MEA approach. Compared to the benchmark MEA, reduced Pt loading stratified MEA showed ± 2 % performance change from 20- 60 % RH and about 13 % performance increase at fully humidified conditions. An improvement in mass transport losses was realized with the reduced Pt loading stratified CCL MEAs because they were more porous than the 0.4 mg_{Pt}/cm^2 loading stratified MEAs in Chapter 5. The polarization analysis results showed that high performance can be achieved in stratified CCL MEAs that have a lower Pt loading because they had lower ohmic losses than monolayer MEAs owing to the high ionomer loading content in the inner layer. As RH was increased, ohmic losses increased with increasing ionomer thickness in the inner layer of the stratified MEAs. The optimal two-layer design was achieved when Pt loading ratio between the layers was 1:6, because it presented a higher ECSA, demonstrated higher performance at 0.65 V, and improved mass transport losses.

The AST for all the MEAs saw a decrease in performance which was correlated to a decrease in CCL thickness, membrane degradation, and ECSA loss. Stratified MEAs were shown to be more durable than monolayer MEAs at equivalent Pt loadings. The high ionomer loading adjacent to the membrane of the stratified MEAs increases moisture in the CL, thus lowering the degradation process of the stratified CCLs. The bilayer interface in the stratified CCL MEA also played a role in disrupting mass transport during the fuel starvation process. Compared to the benchmark high Pt loading MEA, the reduced Pt loading stratified MEA increased the durability of an MEA by decreasing the ECSA loss by 41.83 % and OCV losses by 26.25 %. However, an increase of 18.82 % in kinetic losses was observed.

CHAPTER 7

7. Conclusions and Recommendations

More efforts are required in designing MEAs that are more durable and have high performance to achieve the desired low Pt loading in PEMFCs. This study has shown that reducing Pt loading depends on the ionomer loading but the type of catalyst, and the Pt content might also have an effect. Further studies need to be conducted to prove this.

It has been revealed by several studies that the ionomer network in the CL has a significant impact on the electrode structure and can either improve or impair catalyst utilization (Lee et al., 1998; Sasikumar et al., 2004; Passalacqua et al., 2001; Beattie et al., 2001). It would be valuable to determine the Pt utilization for each MEA to better understand the MEA performance. Also, determining Pt utilization would give a better insight of the relationship between the ionomer content, ECSA, and RH. This could lead to a better design of a stratified MEA design with higher performance.

The CL agglomerate structure influences the BET surface area and porosity which in turn influences performance. However, there was no observed correlation between the BET surface area and ECSA. MEA characterisation can also be enhanced by employing the use of alternative characterisation techniques such as X-ray diffraction (XRD), X-ray photoelectron spectroscopy (XPS), and Fourier-transform infrared spectroscopy (FTIR) techniques to give a full sight of the CL agglomerate structure.

Finding an optimal MEA design is dependent on both MEA materials and PEMFC operating conditions. Thus, increasing performance requires changing more than two variables and that would not be feasible in an experimental study. It would be plausible to first perform a numerical study to investigate the influence of changing the performance variables and then conduct an experimental study based on the results.

The AST results show that catalyst loading plays a major role in the durability of an MEA. Therefore, it is imperative to always consider the impact of reducing Pt loading on MEA durability. Stratified MEAs were also shown to improve MEA durability. These findings are anticipated to contribute to the development of more durable MEAs for low-temperature PEFCs.

With further investigations, one of the major challenges of PEMFCs, which is cost and durability, could be overcome. It is believed that finding the optimal ionomer gradient for stratification, which significantly

improves performance at higher loadings, will make it possible to reduce CCL Pt loading even further (to 0.3 mg_{Pt}/cm^2 and lower) without compromising the performance and durability of an MEA.

8. Appendix: Cyclic voltammograms

8.1 Ionomer loading effect on Cyclic Voltammograms

The CV profiles of different ionomer content MEAs and stratified MEAs were measured under different RH conditions and they are shown in the Figures below (Figure 8.1 and Figure 8.2).

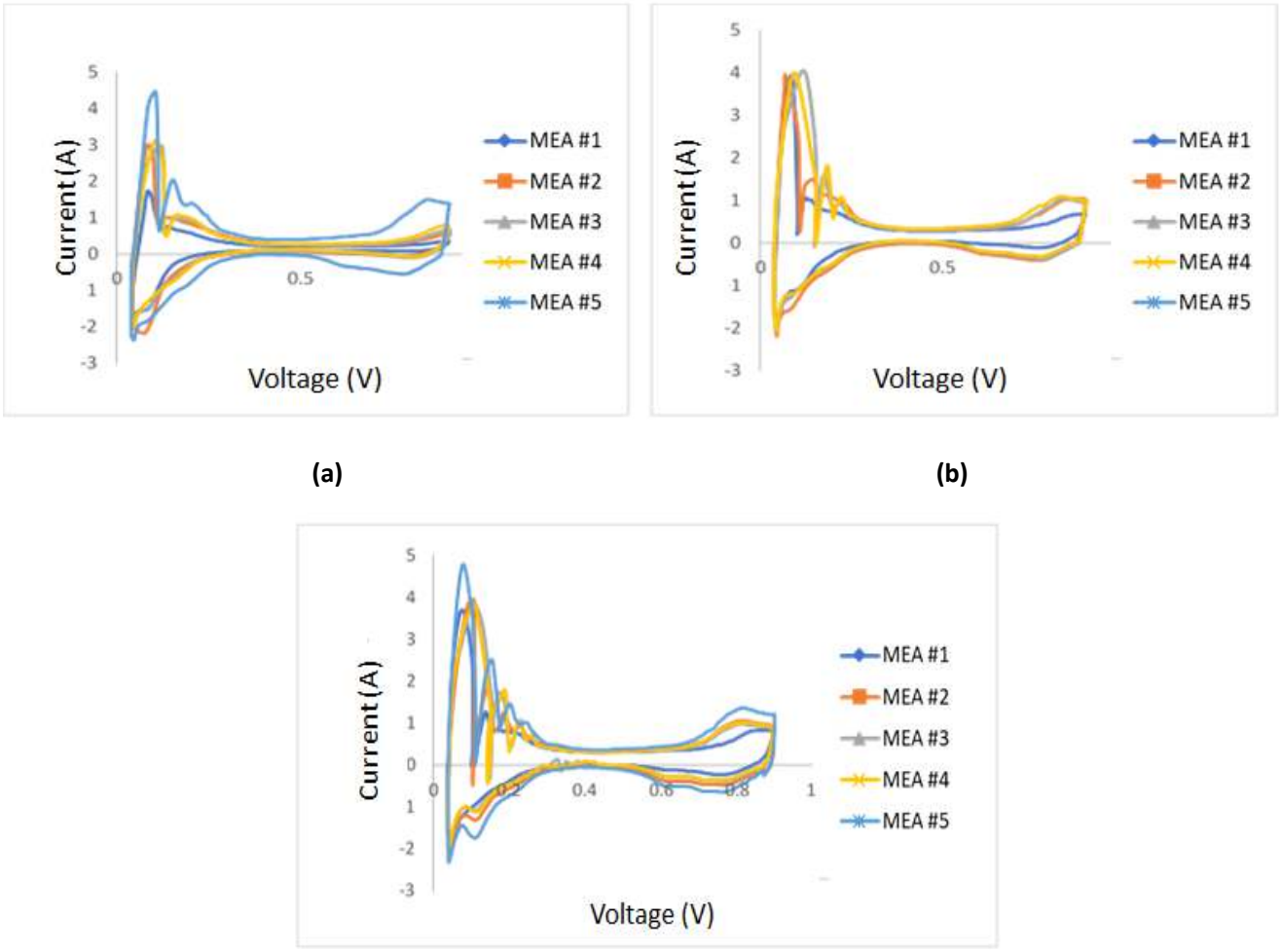

Figure 8.1.Cyclic voltammograms of different ionomer loading MEAs at: (a) 20 % RH; (b) 60 % RH; (c) 100 % RH.

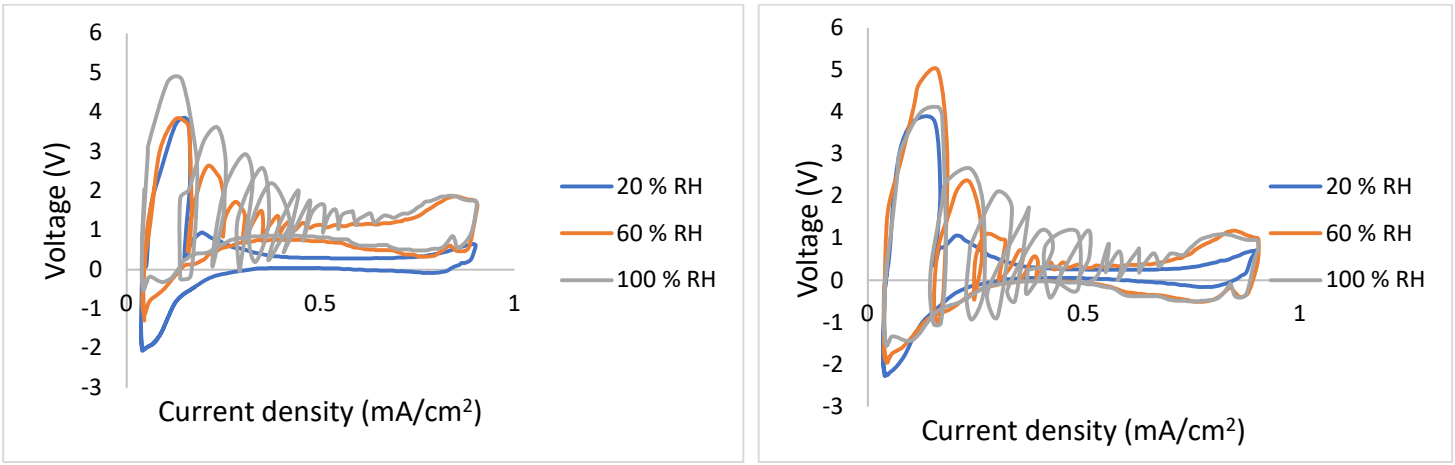

Figure 8.2. Cyclic voltammograms of stratified MEAs at different RH conditions: (a) MEA #6; (b) MEA #7.

8.2. Carbon degradation effect on cyclic voltammograms

Figure 8.3 and Figure 8.4 show the cyclic voltammograms measured during the carbon degradation test. The CVs were measured at 60 % RH conditions.

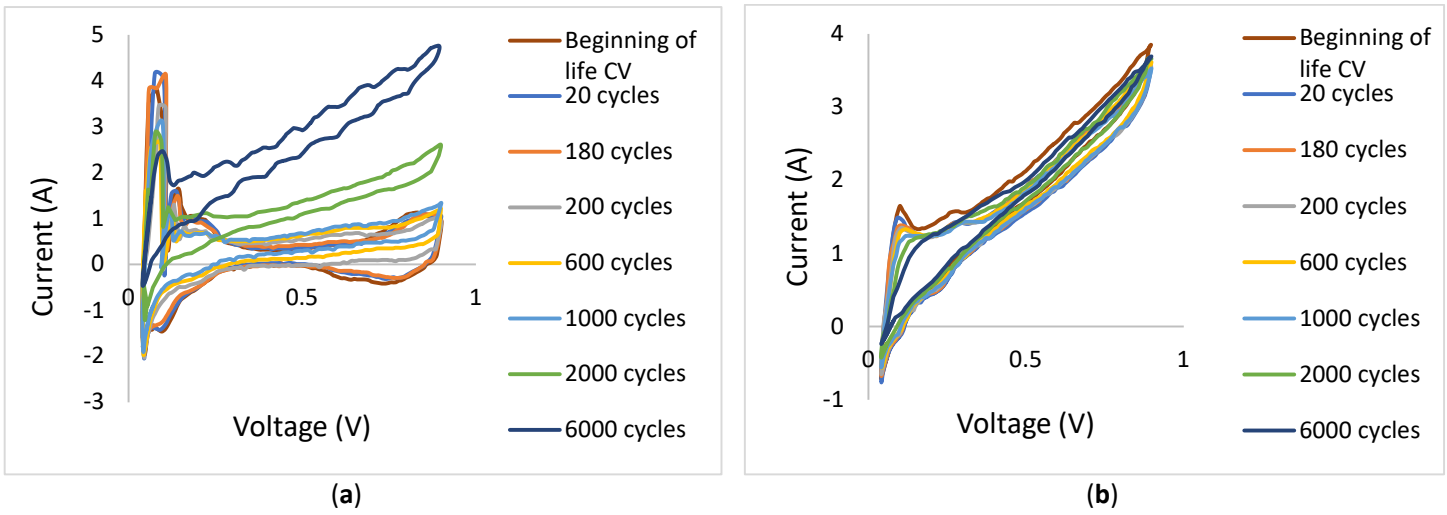

Figure 8.3. Cyclic voltammograms with progressive potential cycling for: (a) MEA #6; (b) MEA #2.

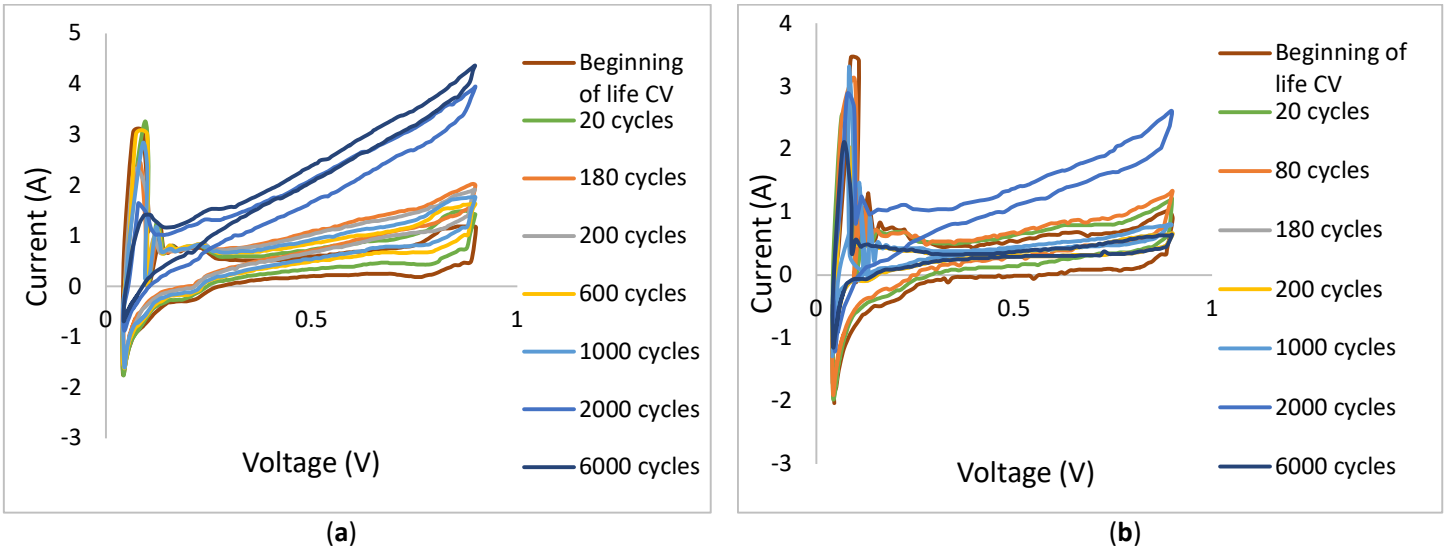

Figure 8.4. Cyclic voltammograms of reduced Pt loading MEAs with progressive cycling for: (a) MEA #11 and (b) MEA #12.

9. References

Alavi, F. et al., 2017. Fuel cell cars in a microgrid for synergies between hydrogen and electricity networks. *Applied Energy,* Volume 192, p. 296–304.

Allen, R. & Giallombardo, J., 2000. *Method of d of forming robust metal, metal oxide, and metal alloy layers on ion-conductive polymer membranes.* United States, Patent No. 6,077,621.

Andersen, S. & Grahl-Madsen, L., 2016. Interface contribution to the electrode performance of proton exchange membrane fuel cells- Impact of the ionomer. *Journal of Hydrogen Energy,* Volume 41, pp. 1892-1901.

Anon., 2003. Fundamentals, technology, applications. In: *Handbook of fuel cells.* Chichester: Wiley, p. 538.

Anon., 2005. *Calculation of the platinum's active surface.* [Online]
Available at: www.bio-logic.net

Anon., 2012. *Energy Efficiency and Renewable Energy.* [Online]
Available at: http://www.eere.energy.gov/hydrogenandfuelcells/mypp/pdfs/fuel_cells.pdf

Anon., 2015. *DOE Technical Targets for Polymer Electrolyte Membrane Fuel Cell Components.* [Online]
Available at: https://www.energy.gov/eere/fuelcells/doe-technical-targets-polymer-electrolyte-membrane-fuel-cell-components

Anon., 2018. World's first hydrogen-powered zero-emission combustion engine launched. *Governemnt europa*, 23 April.

Anon., 2019. *Home: Energy Transition Guide.* [Online]
Available at: https://www.woodmac.com/nslp/energy-transition-guide/

Anon., n.d. [Online]
Available at: https://za.pinterest.com/pin/132082201549329112/

Antoine, O. & Durand, R., 2001. In situ electrochemical deposition of Pt nanoparticles on carbon and inside Nafion. *Electrochemical and Solid-State Letters,* 4(5), pp. A55-A58.

Antolini, E., Giorgi, L., Pozio, A. & Passalacqua, E., 1998. Influence of Nafion loading in the catalyst layer of gas-diffusion electrodes for PEFC. *Journal of Power Sources,* Volume 77, pp. 136-142.

Aricò, A. et al., 2008. Performance and degradation of high temperature polymer electrolyte fuel cell catalysts. *Journal of Power Sources,* Volume 178, pp. 525-536.

Baik, K., Hong, B. & Kim, M., 2013. Effects of operating parameters on hydrogen crossover rate through Nafion® membranes in polymer electrolyte membrane fuel cells. *Renewable Energy,* Volume 57, pp. 234-239.

Bail, K. et al., 2013. Local measurements of hydrogen crossover rate in polymer electrolyte membrane fuel cells. *Applied Energy,* Volume 101, pp. 560-566.

Banham, D. & Ye, S., 2017. Current Status and Future Development of Catalyst Materials and Catalyst Layers for Proton Exchange Membrane Fuel Cells: An Industrial Perspective. *ACS Energy Letters,* pp. 1-8.

Barbir, F., 2005. *PEM Fuel Cells: Theory and Practice.* 1st ed. Storrs: Academic Press.

Beattie, P. et al., 2001. Ionic conductivity of proton exchange membranes. *Journal of Electroanalytical Chemistry,* 503(1-2), pp. 45-56.

Berg, P., Novruzi, A. & Promislow, K., 2006. Analysis of a cathode catalyst layer model for a polymer electrolyte fuel cell. *Chemical Engineering Science,* Volume 61, p. 4316 – 4331.

Bi, W., Sun, Q., Deng, Y. & Fuller, T., 2009. The effect of humidity and oxygen partial pressure on degradation of Pt/C catalyst in PEM fuel cell.. *Electrochemical Acta,* 54(6), pp. 1826-1833.

Borup, R. et al., 2007. Scientific aspects of polymer electrolyte fuel cell durability and degradation. *Chem Rev,* 107(10), p. 3904–3951.

Bose, S. et al., 2011. Polymer membranes for high temperature proton exchange membrane fuel cell: Recent advances and challenges. *Progress in Polymer Science,* 36(6), pp. 813-843.

Brancovik, S., Wang, J. & Adžić, R., 2001. Metal monolayer deposition by replacement of metal adlayers on electrode surfaces. *Surface Science,* 474(1-3), pp. L173-L179.

Broka, K. & Ekdunge, P., 1997. Modelling the PEM fuel cell cathode. *Journal of Applied Electrochemistry,* Volume 27, pp. 281-289.

Cetinbas, F., Advani, S. & Prasad, A., 2015. Optimization of polymer electrolyte membrane fuel cell catalyst layer with bidirectionally-graded composition. *Electrochimica Acta,* Volume 174, pp. 787-798.

Cetinbas, F., Ahluwalia, R., Kariuki, N. & Myers, D., 2018. Agglomerates in Polymer Electrolyte Fuel Cell Electrodes: Part I. Structural Characterization. *The Electrochemical Society,* 165(13), pp. F1051-F105.

Cha, S. & Lee, W., 1999. Performance of Proton Exchange Membrane Fuel Cell Electrodes Prepared by Direct Deposition of Ultrathin Platinum on the Membrane Surface. *Journal of The Electrochemical Society,* 146(11), pp. 4055-4060.

Cheng, C., Malek, K., Sui, P. & Djilali, N., 2010. *Effect of particle nano-particle Size on the microstructure of PEM fuel cell catalyst layers: Insight from. Electrochemica Acta,* Volume 5, pp. 1588-1597.

Chen, G. et al., 2017. Gradient design of Pt/C ratio and Nafion content in cathode catalyst layer of PEMFCs. *International Journal of Hydrogen Energy,* Volume 42, pp. 29960-299652.

Choi, K.-H.et al., 2000. Water transport in polymer membranes for PEMFC. *Journal of Power Sources,* 86(1-2), pp. 197-201.

Chun, J. et al., 2013. Development of a porosity-graded micro porous layer using thermal expandable graphite for proton exchange membrane fuel cells. *Renewable Energy,* Volume 58, pp. 28-33.

Cimenti, M., Bessarabov, D., Tam, M. & Stumper, J., 2010. The Electrochemcial Society. *Investigation of Proton Transport in the Catalyst Layer of PEM Fuel Cells by Electrochemical Impedance Spectroscopy,* 28(23), pp. 147-157.

Cleghorn, S. et al., 2006. A polymer electrolyte fuel cell life test: 3 years of continuous operation. *Journal of Power Sources,* Volume 158, pp. 54- 446.

Cohen, A., 2019. Clean Hydrogen Power Can Refuel Debate For Transportation Industry. *Forbes magazine*, 28 May.

Cook, B., 2002. Introduction to fuel cells and hydrogen technology. *Engineering Science & Education Journal,* 11(6), p. 205 – 216.

Cooper, K. & Smith, M., 2006. Electrical test methods for on-line fuel cell ohmic resistance measurement. *Journal of Power Sources,* 160(2), pp. 1088-1095.

Crabtree, G., Dresselhas, M. & Buchanan, M., 2004. The Hydrogen Economy. *Physics Today,* pp. 1-7.

Curnick, O., Mendes, P. & Pollet, B., 2010. Enhanced durability of a Pt/C electrocatalyst derived from Nafion-stabilised colloidal platinum nanoparticles. *Electrochemicstry communications,* Volume 12, pp. 1017-1020.

Darling, R. & Meyers, J., 2005. Mathematical model of platinum movement. *Journal of The Electrochemical Society,* 152(1), pp. A242-A247.

Darling, R. & Meyers, J., 2005. Mathematical model of platinum movement. *Journal of The Electrochemical Society,* 152(1), pp. A242-A247.

Das, V. et al., 2017. Recent advances and challenges of fuel cell based power system architectures and control – A review. *Renewable and Sustainable Energy Reviews,* Volume 73, pp. 10-18.

Debe, M., 2012. Electrocatalyst approaches and challenges for automotive fuel cells. *Nature,* 22 June, Volume 486, pp. 43-44.

Debe, M., 2012. Electrocatalyst approaches and challenges for automotive fuel cells. *Nature,* Volume 486, pp. 43-51.

Deng, H. et al., 2016. Effect of electrode design and operating condition on performance of hydrogen alkaline membrane fuel cell. *Applied Energy,* Volume 183, pp. 1272-1278..

Dhanushkodi, S. et al., 2013. Carbon corrosion fingerprint development and de-convolution of performance loss according to degradation mechanism in PEM. *Journal of Power Sources,* Volume 240, pp. 114-121.

Dubau, L. et al., 2014. Carbon corrosion induced by membrane failure: The weak link of PEMFC long-term performance. *International Journal of Hydrogen Energy,* Volume 39, pp. 21902-21914.

Eslamibidgoli, M. & Eikerling, M., 2016. How theory and simulation can drive fuel cell electrocatalysis. *Nano Energy,* Volume 29, pp. 334-361.

Fan, L., 2013. *Development and Characterisation of functional composite materials for advanced energy conversion technologies,* Stocklhom: Royal Institute of Technology.

Fan, L. et al., 2019. Mechanism of Water Content on the Electrochemical Surface Area of the Catalyst Layer in the Proton Exchange Membrane Fuel Cell. *J. Phys. Chem. Lett.,* p. 6409–6413.

Ferreira, P. et al., 2005. Instability of Pt／C Electrocatalysts in Proton Exchange Membrane Fuel Cells: A Mechanistic Investigation. *The Electrochemical Society,* 152(11).

Francia, C., Ijeri, V., Specchia, S. & Spinelli, P., 2011. Estimation of hydrogen crossover through Nafion® membranes in PEMFCs. *Journal of Power Sources,* 196(4), pp. 1833-1839.

Garland, N., Benjamin, T. & Kopasz, J., 2007. DOE Fuel Cell Program: Durability Technical Targets and Testing Protocols. *ECS Transactions,* 11(1), p. 923.

Gasteiger, H., Kocha, S., Sompalli, B. & Wagner, F., 2005. Activity benchmarks and requirements for Pt, Pt-alloy, and non-Pt oxygen. *Applied Catalysis B: Environmental,* Volume 56, pp. 9-35.

Gasteiger, H., Panels, J. & Yan, S., 2004. Dependence of PEM fuel cell performance on catalyst loading. *Journal of Power Sources,* 127(1-2), p. 162–171.

Ghassemi, A. & Pak, A., 2011. Pore scale study of permeability and tortuosity for flow through particulate media using Lattice Boltzmann method. *International Journal for Numerical and Analytical Methods in Geomechanics,* Volume 35, pp. 866-901.

Gode, P. J. F. L. G., Lundblad, A. & Sundholm, G., 2003. Influence of electrode structure on electrochemical performance of the PEFC cathode. *Electrochemical Acta,* Volume 48, p. 4178.

Gomadam, P. & Weidner, J., 2005. Analysis of electrochemical impedance spectroscopyin proton exchange membrane fuel cells. *International Journal of Energy Research,* Volume 29, p. 1133–1151.

Greszler, T., Caulk, D. & Sinha, P., 2012. The Impact of Platinum Loading on Oxygen Transport Resistance. *Journal of the Electrochemical Society,* 159(12), p. F831.

Gu, W., Baker, D. R., Liu, Y. & Gasteiger, H. A., 2009. Handbook of Fuel Cells - Fundamentals, Technology and Applications. In: G. H. Yokokawa & W. Vielstich, eds. s.l.:John Wiley & Sons.

Haas, H. & Davis, M., 2009. Electrode and Catalyst Durability Requirements in Automotive PEM Applications:Technology Status of a Recent MEA Design and Next Generation Challenge. *s. ECS transactions,* 25(1), pp. 1623-1631.

Haile, S., 2013. *Fuel cell materials and components,* California: California Institute of Technology.

Hannach, M., Pauchet, J. & Prat, M., 2011. Pore network modeling: Application to multiphase transport inside the cathode catalyst layer of proton exchange membrane fuel cell. *Electrochimica Acta,* 56(28), pp. 10796-10808.

Hannach, M., Pauchet, J. & Prat, M., 2011. Pore network modeling: Application to multiphase transport inside the cathode catalyst layer of proton exchange membrane fuel cell. *Electrochimica Acta,* 56(28), pp. 10796-10808.

Hannach, M. et al., 2014. Characterization of pore network structure in catalyst layers of polymer electrolyte fuel cells. *Journal of Power Sources,* Volume 247, pp. 322-326.

Harop, P., 2019. *IDtechEx: Products.* [Online]
Available at: https://www.idtechex.com/en/research-report/fuel-cell-vehicles-2019-2029/627

Haug, A. et al., 2002. Increasing proton exchange membrane fuel cell catalyst effectiveness through sputter deposition. *Journal of the Electrochemical Society,* 149(3), pp. A280-A287.

Hickner, M., Fujimoto, C. & Cornelius, C., 2006. Transport in sulfonated poly (phenylene)s: Proton conductivity, permeability, and the state of water. *Polymer,* Volume 47, p. 4238–4244..

Hickner, M., Fujimoto, C. & Cornelius, C., 2006. Transport in sulfonated poly (phenylene)s: Proton conductivity, permeability, and the state of water. *Polymer,* Volume 47, p. 4238–4244.

Hinebaugh, J. & Fishman, Z. a. B. A., 2010. Unstructured Pore Network Modeling with Heterogeneous PEMFC GDL Porosity Distributions. *The Electrochemical Society,* 157(11), p. B1651.

Holton, O. & Stevenson, J., 2013. The Role of Platinum in Proton Exchange Membrane Fuel Cells. 57(4), p. 259.

Huanga, T. et al., 2012. Ultra-low Pt loading for proton exchange membrane fuel cells by catalyst coating technique with ultrasonic spray coating machine. . *International Journal of Hydrogen Energy,* 37(18), pp. 13872-13879.

Inoue, H. & Higuchi, E., 2009. Japan, Patent No. 252521.

Jalani, N. et al., 2006. Performance analysis and impedance spectral signatures of high temperature PBI–phosphoric acid gel membrane fuel cells. *Journal of Power Sources,* 160(2), pp. 1096-1103.

Jang, J. et al., 2009. Complex Capacitance Analysis of Ionic Resistance and Interfacial Capacitance in PEMFC and DMFC Catalyst Layers. *Journal of the Electrochemical Society,* 156(11), p. B1293.

Jang, J. et al., 2009. Complex Capacitance Analysis of Ionic Resistance and Interfacial Capacitance within Cathode Layers of PEMFC and DMFC Electrodes. *ECS Transactions,* 25(1), p. 985.

Jang, S.-E. & Kim, H., 2010. Effect of Water Electrolysis Catalysts on Carbon Corrosion in Polymer Electrolyte Membrane Fuel Cells. *JHCS Communications,* 132(42), p. 14701.

Jeon, S. et al., 2010. Effect of ionomer content and relative humidity on polymer electrolyte membrane fuel cell (PEMFC) performance. *International Journal of Hydrogen Energy,* Volume 35, pp. 9678-9686.

Jeon, S. et al., 2010. Effect of ionomer content and relative humidity on polymer electrolyte membrane fuel cell (PEMFC) performance of membrane electrode assemblies (MEAs) prepared by decal transfer method. *International Journal of Hydrogen Energy,* Volume 35, pp. 9678-9686.

Ji, M. & Wei, Z., 2009. A Review of Water Management in Polymer Electrolyte Membrane Fuel Cells. *Energies,* 2(4), pp. 1057-1106.

Jomori, S., Nonoyama, N. & Yoshida, T., 2012. Analysis and modeling of PEMFC degradation: Effect on oxygen transport. *Journal of Power Sources,* Volume 215, pp. 18-27.

Jouin, M. et al., 2013. Prognostics and Health Management of PEMFC – State of the art and remaining challenges. *International Journal of Hydrogen Energy,* 38(35), pp. 15307-15317.

Jourdan, M., Mounir, H. & El Marjani, A., 2014. *Compilation of factors affecting durability of Proton Exchange Membrane Fuel Cell (PEMFC).* Ouarzazate, 2014 International Renewable and Sustainable Energy Conference (IRSEC), pp. 542-547.

Jourdan, M., Mounir, H. & Marjani, R., 2015. Compilation of factors affecting durability of Proton Exchange Membrane Fuel Cell (PEMFC). *2014 International Renewable and Sustainable Energy Conference (IRSEC),* pp. 542-547.

Jung, C., Kim, S., Lee, S. & Yi, S., 2016. Three-dimensional reconstruction of coarse dense catalyst layer for proton exchange membrane fuel cells. *Electrochemica Acta,* Volume 211, pp. 142-147.

Jung, C.-Y., Kim, T.-H. & Yi, S.-E., 2014. Ultrahigh PEMFC Performance of a Thin-Film, Dual-electrode Assembly with Tailored Electrode Morphology. *ChemSusChem,* 7(2), pp. 466-473.

Jung, C., Vahc, Z., Kim, T. & Yi, S., 2014. Investigation of the dual-layered electrode composed of catalyst layers with different phase separation levels for PEMFC. *Electrochemica Acta,* Volume 196, pp. 495-502.

Karan, K., 2007. Assessment of transport-limited catalyst utilization for engineering of ultra-low Pt loading polymer electrolyte fuel cell anode. *Electrochemistry Communications,* 9(4), pp. 747-753.

Khajeh-Hosseini-Dalasm, M., Kermani, M., Moghaddam, G. & Stockie, J., 2010. A parametic study of cathode catalyst layer structural parameters on the performance of a PEM fuel cell. *Journal of Hydrogen Energy,* Volume 35, pp. 2417-2427.

Kim, G. et al., 2015. Design of an Advanced Membrane Electrode Assembly Employing a Double-Layered Cathode for a PEM Fuel Cell. *ACS Applied Materials & Interfaces,* 7(50), p. 27581–27585.

Kim, K. et al., 2010. The effects of Nafion ionomer content in PEMFC MEAs prepared by catalyst-coated membrane (CCM) spraying method. International Journal of Hydrogen Energy. Volume 35, pp. 2119-2126.

Kim, K. et al., 2010. The effects of relative humidity on the performances of PEMFC MEAs with various Nafion ionomer contents. *International Journal of Hydroegn Energy,* 35(23), pp. 13104-13110..

Kim, O. et al., 2013. Ordered macroporous platinum electrode and enhanced mass transfer in fuel cells using inverse opal structure. *Nature Communications,* 4(2473), pp. 1-9.

Knights, S. C. K. S.-P. J. &. W. D., 2004. Aging mechanisms and lifetime of PEFC and DMFC. *Journal of Power Sources,* 127(1), pp. 127-134.

Kongkanand, A. G. W. &. M. M., 2017. *Proton-Exchange Membrane Fuel Cells with Low-Pt Content,* Pontiac: s.n.

Kongkanand, A. & Mathias, M., 2016. The Priority and Challenge of High-Power Performance of Low Platinum Proton-Exchange Membrane Fuel Cells. *The Journal of Physical Chemistry Letters,* 7(7), pp. 1127-1137.

Kreitmeier, S., Schuler, G. A., Wokaun, A. & Büchi, F., 2012. Investigation of membrane degradation in polymer electrolyte fuel cells using local gas permeation analysis. *Journal of Power Sources,* Volume 212, pp. 139-147.

Kreuer, K., 1997. On the development of proton conducting materials for technological applications. *Solid State Ionics,* 97(1-4), pp. 1-15.

Kreuer, K., 2000. On the complexity of proton conduction phenomena. *Solid State Ionics,* Volume 136–137, p. 149–160.

Kundu, S., Fowler, M., Simon, L. & Grot, S., 2006. Morphological features (defects) in fuel cell membrane electrode assemblies. *Journal of Power Sources,* 157(2), pp. 650-656.

Kusoglu, A. et al., 2007. Mechanical response of fuel cell membranes subjected to a hygro-thermal cycle. *Journal of Power sources,* Volume 161, pp. 987-996.

Larminie, J. & Dicks, A., 2003. *Fuel Cell Systems Explained.* 2nd ed. England: John Wiley & Sons.

Lee, S. et al., 1998. Effects of Nafion impregnation on performances of PEMFC electrodes. *Electrochimica Acta,* 43(24), pp. 3693-3701.

Lee, S. et al., 1998. Effects of Nafion impregnation on performances of PEMFC electrodes. *Electrochemica Acta,* 43(24), pp. 693-701.

Litster, S. & McLean, G., 2004. *PEM Fuel Cell Electrodes.* North Vancouver: Journal of Power Sources.

Liu, J., Liu, C.-T., Zhao, L. & Wang, Z.-B., 2015. Highly Durable Direct Methanol Fuel Cell with Double-Layered Catalyst Cathode. *Journal of Nanomaterials,* Volume 2015.

Liu, X., Guo, H. & Ma, C., 2006. Water flooding and two-phase flow in cathode channels of proton exchange membrane fuel cells. *Journal of Power Sources,* 156(1), p. 267–280.

Liu, X., Guo, H. & Ma, C., 2006. Water flooding and two-phase flow in cathode channels of proton exchange membrane fuel cells. *Journal of Power Sources,* 156(1), p. 267–280.

Liu, X., Guo, H., Ye, F. & Ma, C., 2007. Water flooding and pressure drop characteristics in flow channels of proton exchange membrane fuel cells. *Electrochemica Acta,* Volume 52, p. 3607–3614.

Liu, X., Guo, H., Ye, F. & Ma, C., 2007. Water flooding and pressure drop characteristics in flow channels of proton exchange membrane fuel cells.. *Electrochemica Acta,* Volume 52, p. 3607–3614.

Li, W. & Lane, A., 2011. Resolving the HUPD and HOPD by DEMS to determine the ECSA of Pt electrodes in PEM. *Electrochemical communications,* Volume 13, pp. 913-916.

Li, Z., Zheng, Z., Xu, L. & Lu, X., 2019. A review of the applications of fuel cells in microgrids: opportunities and challenges. *BMC Energy,* 1(8).

Macauley, N. et al., 2018. Performance of Stratified Fuel Cell Catalyst Layer. *Electrochemical Society,* Volume MA2017-02, p. 1379.

Malevich, D. et al., 2008. Effect of Relative Humidity on Electrochemically Active Area and Impedance. *The electrochemical society,* 16(2), pp. 1763-1774.

Malko, D., Lopes, T., Ticianelli, E. & Kucernak, A., 2016. A catalyst layer optimisation approach using electrochemical impedance spectroscopy for PEM fuel cells operated with pyrolysed transition metal-N-C catalysts. *Journal of Power Sources,* Volume 323, pp. 189-200.

Marquis, J. & Coppens, M.-O., 2013. Achieving ultra-high platinum utilization via optimization of PEM fuel cell cathode catalyst layer microstructure. *Chemical Engineering Science,* 11 October, Volume 102, pp. 151-162.

Marr, C. & Li, X., 1999. Composition and performance modelling of catalyst layer in a proton exchange membrane fuel cell. *Journal of Power Sources,* Volume 77, pp. 17-27.

Martin, S., Garcia-Ybarra, P. & Castillo, J., 2010. High platinum utilization in ultra-low Pt loaded PEM fuel cell cathodes prepared by electrospraying. *International Journal of Hydrogen Energy,* 35(19), pp. 1046-10451.

Ma, S., Solterbeck, C., Odgaard, M. & Skou, E., 2009. Microscopy studies on pronton exchange membrane fuel cell. *Applied Physics A,* Volume 96, pp. 581-589.

Matsuda, H., Fushinobu, K., Ohma, A. & Okazaki, K., 2011. Structural effect of cathode catalyst layer on the performance of PEFC. *Journal of Thermoscience and Technology,* Volume 6, pp. 154-163.

Migliardini, F. & Corbo, P., 2013. CV and EIS Study of Hydrogen Fuel Cell Durability in Automotive Applications. *International Journal of Electrochemical Science,* Volume 8, p. 11035.

Millingotn, B., Whipple, V. & Pollet, B., 2011. A novel method for preparing proton exchange membrane fuel cell electrodes by the ultrasonic-spray technique. *Journal of Power Sources,* 192(20), pp. 8500-8508.

Monk, P., 2001. *Fundamentals of Electro-Analytical Chemistry.* Singapore: Wi;ey & Sons.

Nanakoudis, A., 2019. *SEM: Types of Electrons and the Information They Provide.* [Online] Available at: https://www.thermofisher.com/blog/microscopy/sem-types-electrons-and-the-information-they-provide/

Nguyen, T. & Knobbe, M., 2003. A liquid water management strategy for PEM fuel cell stacks. *Journal of Power Sources,* Volume 114, p. 70–79.

Norin, L., Kostecki, R. & McLarnon, F., 2002. Study of Membrane Degradation in High Power-Lithium Ion Cells. *Electrochemical and Solid-State letters,* 5(4), pp. A67-A69.

O'Hayre, R., Barnett, D. & Prinz, F., 2005. The Triple Phase Boundary: A Mathematical Model and Experimental Investigations for Fuel Cells. *Journal of the Electrochemical Society,* 152(2), pp. A439-A444..

O'Hayre, R., Cha, S.-W., Colella, W. & Prinz, F. B., 2016. *Fuel Cell Fundamentals.* New York: Wiley & Sons.

Oh, H., Lee, J. & Kim, H., 2012. Electrochemical carbon corrosion in high temperature proton exchange membrane fuel cells. *International Journal of Hydrogen Energy,* Volume 37, pp. 10844-10849.

Ohma, A. et al., 2011. Analysis of proton exchange membrane fuel cell catalyst layers for reduction of platinum loading at Nissan. *Electrochemica Acta,* 56(28), pp. 10832-10841.

Okada, T., 1999. The effect of impurity ions at the anode side on the membrane performances: Part 1. *Journal of Electroanalytical Chemistry,* 465(1), p. 1–17.

Owejan, J., Owejan, J. & Gu, W., 2013. Impact of Platium Loading and Catalyst Layer Structure on PEMFC Performance. *The Electrochemical Society,* Volume 160, p. F824.

Paganin, V., Ticianelli, E. & Gonzalez, E., 1996. Development and electrochemical studies of gas diffusion electrodes for polymer electrolyte fuel cells. *Journal of Applied Electrochemistry,* Volume 26, pp. 297-304.

Park, G. et al., 2004. Effect of PTFE contents in the gas diffusion media on the performance of PEMFC. *Journal of Power Sources,* 131(1-2), pp. 182-187.

Park, J.-H.et al., 2012. Understanding the mechanism of membrane electrode assembly degradation by carbon corrosion by analyzing the microstructural changes in the cathode catalyst layers and polarization losses in proton exchange membrane fuel cell. *Electrochemica Acta,* Volume 83, pp. 294-304.

Park, Y. & Caton, J., 2008. An experimental investigation of electro-osmotic drag coefficients in a polymer electrolyte membrane fuel cell. *International Journal of Hydrogen Energy,* 33(24), pp. 7513-7520.

Parthasaraty, B. D. S. S. A. &. A. J. & Martin, C., 1992. The Platinum Microelectrode/Nafion Interface: An Electrochemical Impedance Spectroscopic Analysis of Oxygen Reduction Kinetics and Nafion Characteristics. *Journal of the Electrochemical Society,* 139(6), p. 1634.

Pasaogullari, U. & Wang, C., 2005. Two-phase transport in polymer electrolyte fuel cells with bi-layer cathode gas diffusion media. *Journal fo Electrochemical Society,* 152(1), p. A380–A390.

Passalacqua, E. et al., 1998. Influence of the structure in low-Pt loading electrodes for polymer electrolyte fuel cell. *Electrochemica Acta,* Volume 2001, pp. 3665-3673.

Passalacqua, E. et al., 2001. Nafion content in the catalyst layer of polymer electrolytefuel cells: effects on structure and performance. *Electrochemica Acta,* Volume 43, pp. 3665-3673.

Passos, R., Paganin, V. & Ticianelli, E., 2006. Studies of the performance of PEM fuel cell cathodes with the catalyst layer directly applied on Nafion membranes. *Electrochemica Acta,* 51(25), pp. 5239-5245.

Qi, Z. & Kaufmann, A., 2003. Low Pt loading high performance cathodes for PEM fuel cells. *Journal of Power Sources,* Volume 113, pp. 37-43.

Rabat, H. & Brault, P., 2007. *Plasma Sputtering Deposition of PEMFC Porous Carbon Platinum Electrodes.* France, Wiley Online Library, pp. 81-86.

Rajalakshmi, N. & Dhathathreyan, K., 2007. Catalyst layer in PEMFC electrodes – fabrication, characterization and analysis. *Cheemical Engineering Journal,* 129(1-3), pp. 31-40.

Ray, P., 2018. *Global Hydrogen Fuel Cell Vehicle Sales Seeing Progress.* [Online]
Available at: https://www.hybridcars.com/global-hydrogen-fuel-cell-vehicle-sales-seeing-progress/

Roshandel, R., Farhanieha, B. & Saievar-Iranizad, E., 2005. The effects of porosity distribution variation on PEM fuel cell performance. *Renewable Energy,* 30(10), pp. 1557-1572.

Santacesaria, S., 1997. Kinetics and transport phenomena in heterogeneous gas-solid and gas-liquid-solid systems. *Catalysis Today,* 34(3-4), pp. 411-420.

Santarelli, M., Torchio, M. & Cochis, P., 2006. Parameters estimation of a PEM fuel cell polarization curve and analysis of their behavior with temperature. *Journal of Power Sources,* 159(2), pp. 824-835.

Sasikumar, G., Ihm, J. & Ryu, H., 2004. Optimum Nafion content in PEM fuel cell electrodes. *Electrochim Acta,* Volume 50, pp. 601-605.

Schmidt, T. et al., 1998. Characterization of high-surface-area electrocatalysts using a rotating disk electrode configuration. *Journal of the Electrochemical Society,* 145(7), pp. 2354-2358.

Scibioh, M. et al., 2008. Investigation of various ionomer-coated carbon supports for direct methanol fuel cell applications. *Applied Catalysis B: Environmental,* 77(3-4), pp. 373-385.

Sethuraman, V., Weidner, J., Haug, A. & Protsailo, L., 2008. Durability of Perfluorosulfonic Acid and Hydrocarbon Membranes: Effect of Humidity and Temperature. *Journal of Electrochemical Society,* 155(2), p. B119.

Shahgaldi, S., Ozden, A., Li, X. & Hamdullahpur, F., 2018. Cathode catalyst layer design with gradients of ionomer distribution for proton exchange membrane fuel cells. *Energy Conversion and Management,* Volume 171, pp. 1476-1486.

Shao-Horn, Y. et al., 2007. Instability of supported platinum nanoparticies in low-temperature fuel cells. *Topics in Catalysis,* Volume 46, p. 285–305.

Shin, S.-J.et al., 2002. Effect of the catalytic ink preparation method on the performance of polymer electrolyte membrane fuel cells. *Journal Electrochemistry,* 106(1-2), pp. 146-152.

Shukla, S. et al., 2015. Analysis of Low Platinum Loading Thin Polymer Electrolyte Fuel Cell Electrodes Prepared by Inkjet Printing. *Electrochimica Acta,* Volume 156, pp. 289-300.

Sing, K., 2001. The use of nitrogen adsorption for the characterisation of porous materials. *Colloids and Surfaces A: Physicochemical and Engineering Aspects,* Volume 1987-1988, pp. 3-9.

Sing, K., 2015. Assessment of Surface Area by Gas Adsorption. In: *Adsorption by Powders and Porous Solids: Principles, Methodology and Application.* Second ed. Oxford: Academic Press, pp. 237-263.

Soboleva, T. et al., 2011. PEMFC Catalyst Layers: The Role of Micropores and Mesopores on Water Sorption and Fuel Cell Activity. *ACS Publications,* Volume 3, pp. 1827-1837.

Soboleva, T. et al., 2010. On the Micro-, Meso-, and Macroporous Structures of Polymer Electrolyte Membrane. *ACS Applied Materials and Interfaces,* 2(2), pp. 375-384.

Solasi, R. et al., 2007. On mechanical behavior and in-plane modeling of constrained PEM fuel cell membranes subjected to hydration and temperature cycles. *Journal of Power Sources,* 167(2), pp. 366-377.

Song, C. et al., 2007. PEM fuel cell reaction kinetics in the temperature range of 23–120 °C. *Electrochemical Acta,* 57(7), pp. 2552-2561.

Song, D. et al., 2004. Numerical optimization study of the catalyst layer of PEM fuel cell cathode. *Journal of Power Sources,* 126(1-2), pp. 104-111.

Song, J., Cha, S. & Lee, W., 2001. Optimal composition of polymer electrolyte fuel cell electrodes determined by the AC impedance method. *Journal of Power Sources,* Volume 94, pp. 78-84.

Song, Y. et al., 2006. Dependence of high-temperature PEM fuel cell performance on Nafion content. *Journal of Power Sources,* Volume 154, pp. 138-144.

Speder, J., Zana, A. & Arenz, M., 2016. The colloidal tool-box approach for fuel cell catalysts: Systematic study of perfluorosulfonate-ionomer impregnation and Pt loading. *Catalysis Today,* Volume 216, pp. 82-89.

Speder, J., Zana, A. & Arenz, M., 2016. The colloidal tool-box approach for fuel cell catalysts: Systematic study of perfluorosulfonate-ionomer impregnation and Pt loading. *Catalysiis Today,* Volume 216, pp. 82-89.

Speder, J. et al., 2014. Comparative degradation study of carbon supported proton exchange membrane fuel cell electrocatalysts – The influence of the platinum to carbon ratio on the degradation rate. *Journal of Power Sources,* Volume 261, pp. 14-22.

Spernjak, D. et al., 2012. Influence of the microporous layer on carbon corrosion in the catalyst layer. *Journal of Power Sources,* Volume 214, pp. 386-398.

Srinivasarao, M., Bhattacharyya, D., Rengaswamy, R. & Narasimhan, S., 2010. Performance analysis of a PEM fuel cell cathode with multiple catalyst layers. *International Journal of Hydrogen Energy,* Volume 35, pp. 6356-6365.

Starz, K., Auer, E., ThLehmann, T. & Zuber, R., 1999. Characteristics of platinum-based electrocatalysts for mobile PEMFC applications. *Journal of Power Sources,* 84(2), pp. 167-172.

Su, H.-N., Liao, S.-J. & Wu, Y.-N., 2010. Significant improvement in cathode performance for proton exchange. *Journal of Power Sources,* Volume 195, p. 3477–3480.

Sun, W., Peppley, B. & Karan, K., 2005. An improved two-dimensional agglomerate cathode model to study the influence of catalyst layer structural parameters. *Electrochemica Acta,* Volume 50, p. 3359–3374.

Suzuki, A. et al., 2011. Ionomer content in the catalyst layer of polymer electrolyte membrane fuel cell (PEMFC): Effects on diffusion and performance. *International Journal of Hydrogen Energy,* 36(3), pp. 2221-2229.

Taillades, G. et al., 2010. Intermediate Temperature Anode-Supported Fuel Cell Based on BaCe0.9Y0.1O3 Electrolyte with Novel Pr2NiO4 Cathode. In: *Fuel Cells: From Fundamentals to Systems.* s.l.:Wiley Online Library, pp. 166-173.

Takahashi, S. et al., 2015. Analysis of the Microstructure Formation Process and its Influence on the Performance of Polymer ElectrolyteFuel-Cell Catalyst Layers. *ChemElectroChem,* Volume 2, pp. 1560-1567.

Tang, H., Qi, Z., Ramani, M. & Elter, J., 2006. PEM fuel cell cathode carbon corrosion due to the formation of air/fuel boundary at the anode. *Journal of Power Sources,* 158(2), pp. 1306-1312.

Tang, H., Wang, S., Pan, M. & Yuan, R., 2007. Porosity-graded micro-porous layers for polymer electrolyte membrane fuel cells. *Journal of Power Sources,* Volume 166, pp. 41-46.

Taniguchia, A., Akita, T., Yasuda, K. & Miyazaki, Y., 2004. Analysis of electrocatalyst degradation in PEMFC caused by cell reversal during fuel starvation. *Journal of Power Sources,* 130(1-2), pp. 42-49.

Taylor, S. et al., 2016. The Effect of Platinum Loading and Surface Morphology on Oxygen Reduction Activity. *Electrocatalysis,* Volume 7, p. 287–296.

Thepkaew, J., Therdthianwong, A. & Therdthianwong, S., 2008. Key parameters of active layers affecting proton exchange membrane (PEM) fuel cell performance. *Energy,* Volume 33, pp. 1794-1800.

Thommes, M. et al., 2015. Physisorption of gases, with special reference to the evaluation of surface area and pore size distribution. *Pure Applied Chemistry,* 87(9-10), p. 1051– 1069.

Tian, Y. & Wu, J., 2018. A comprehensive analysis of the BET area for nanoporous materials. *AIChE Journal,* 64(1), pp. 286-291.

Uchida, M., Aoyama, Y., Ehda, E. & Ohta, A., 1995. Investigation of the microstructure in the catalyst layer and effects of both perfluorosulfonate ionomer and PTFE-loaded carbon on the catalyst layer of polymer electrolyte fuel cells. *Journal of Electrochemical Society,* 142(12), pp. 4143-4149.

Uygun, Z. & Sezgintürk, M., 2011. A novel, ultra sensible biosensor built by layer-by-layer covalent attachment of a receptor for diagnosis of tumor growth. *Analytica Chimica Acta,* 706(2), pp. 343-348.

Uygun, Z. & Uygun, H., 2014. A short footnote: Circuit design for faradaic impedimetric sensors and biosensors. *Sensors and Actuators B: Chemical,* Volume 202, pp. 448-453.

Vilekar, S. & Datta, R., 2010. The effect of hydrogen crossover on open-circuit voltage in polymer electrolyte membrane fuel cells. *Journal of Power Sources,* 195(8), pp. 2241-2247.

Wagner, F. et al., 2006. Catalyst Development Needs and Pathways for Automotive PEM Fuel Cells.. *ECS Transactions,* 3(1), pp. 19-29.

Wan, C.-H., Lin, M.-T., Zhuang, Q.-H. & Lin, C.-H., 2006. Preparation and performance of novel MEA with multi catalyst layer structure for PEFC by magnetron sputter deposition technique. *Surface and Coatings Technology,* 201(1-2), pp. 214-222.

Wang, Q., Eikerling, M., Song, D. & Liu, Z., 2004. Structure and performance of different types of agglomerates in cathode catalyst layers of PEM fuel cells. *Journal of Electroanalytical chemistry,* Volume 573, pp. 61-69.

Wee, J., Lee, K. & Kim, S., 2007. Fabrication methods for low-Pt-loading electrocatalysts in proton exchange membrane fuel cell systems. *Journal of Power Sources,* 165(2), pp. 667-677.

Wei, Z. et al., 2006. Numerical analysis of Pt utilization in PEMFC catalyst layer using random cluster model. *Electrochemica Acta,* 51(15), pp. 3091-3096.

Wells, O., 2001. Scanning Electron Microscopy. In: J. Buschow, et al. eds. *Encyclopedia of Materials: Science and Technology.* s.l.:s.n.

Wilson, M., Garzon, F., Gottesfeld, S. & Kurt, E., 1993. Surface Area Loss of Supported Platinum in Polymer Electrolyte Fuel Cells. *Journal of Electrochemical Society,* 140(10), pp. 2872-2877.

Wilson, M., Valerio, J. & Gottesfeld, S., 1995. Low platinum loading electrodes for polymer electrolyte fuel cells fabricated using thermoplastic ionomers. *Electrochemica acta,* 40(3), pp. 355-363.

Wood III, D. L., Chlistunoff, J. & Majewski, B. L., 2009. Nafion Structural Phenomena at Platinum and Carbon Interfaces. *Journal of the American Chemical Society,* 131(50), pp. 18096-18104.

Wu, J. et al., 2008. Diagnostic tools in PEM fuel cell research: Part I Electrochemical techniques. *International Journal of Hydrogen Energy,* 33(6), pp. 1735-1746.

Xie, Z. et al., 2005. Functionally Graded Cathode Catalyst Layers for Polymer Electrolyte Fuel Cells II. Experimental Study of the Effect of Nafion Distribution. *Journal of Electrochemical Society,* 152(6), pp. A1171-A1179.

Xiong, L. & Manthiram, A., 2005. High performance membrane-electrode assemblies with ultra-low Pt loading for proton exchange membrane fuel cells. *Electrochimica Acta,* 50(16-17), pp. 3200-3204.

Xu, H., Song, Y., Kunz, H. & Fenton, J., 2005. Effect of Elevated Temperature and Reduced Relative Humidity on ORR Kinetics for PEM Fuel Cells. *Jounal of Electrochemical Society,* 152(9), pp. A1828-A1836.

Yang, C. et al., 2001. Approaches and technical challenges to high temperature operationof proton exchange membrane fuel cells. *Journal of Power Sources,* Volume 103, pp. 1-9.

Yan, Q., Toghiani, H. & Wu, J., 2006. Investigation of water transport through membrane in a PEM fuel cell by water balance experiments. *Journal of Power Sources,* 158(1), pp. 316-325.

Yau, T., Cimenti, M., Bi, X. & Stumper, J., 2011. Effects of cathode gas diffusion layer design on polymer electrolyte membrane fuel cell water management and performance. . *Journal of Power Sources,* 196(22), pp. 9437-9444.

Yoon, Y.-G.et al., 2003. A multi-layer structured cathode for the PEMFC. *Journal of Power Sources,* 118(1-2), pp. 189-192.

Young, A., Stumper, J. & Gyenge, E., 2009. Characterizing the Structural Degradation in a PEMFC. *Journal of the Electrochemical Society,* 156(8), pp. B913-B922.

Yousfi-Steiner, N. et al., 2008. A review on PEM voltage degradation associated with water management: Impacts, influent factors and characterization. *Journal of Power Sources,* 183(1), pp. 260-274.

Yuan, X. et al., 2011. A review of polymer electrolyte membrane fuel cell durability test protocols.. *Journal of Power Sources,* Volume 196, pp. 9107-9116.

Yu, X. & Ye, S., 2007. Recent advance and durability advancement of Pt/C catalytic cathode in PEMFC Part II: Degradation mechanism and durability enhancement of carbon surported platinum catalyst. *Journal of Power Sources,* Volume 172, pp. 145-154.

Yu, X. & Ye, S., 2007. Recent advances in activity and durability enhancement of Pt/C catalytic cathode in PEMFC Part II: Degradation mechanism and durability enhancement of carbon supported platinum catalyst. *Journal of Power Sources,* Volume 172, pp. 145-154.

Zamel, N., 2016. The catalyst layer and its dimensionality- A look into its ingredients and how to characterize their effects. *Journal of Power Sources,* 5 February.pp. 1-19.

Zawodzinski, T., Davey, J., Valerio, J. & Gottesfeld, S., 1995. The water dependence of electro-osmotic drag in proton-conducting polymer electrolytes. *Electrochima Acta,* Volume 40, p. 297–302.

Zawodzinski, T. et al., 1993. Water uptake by and Transport Through Nafion. *Journal of Electrochemical Society,* 140(4), p. 117.

Zawodzinski, T. J. et al., 1993. Water uptake by and transport through Nafion 117 membranes. *Jounal of Electrochemical Society,* Volume 140, p. 1041–1047.

Zenyuk, I., Das, P. & Weber, A., 2016. Understanding Impacts of Catalyst-Layer Thickness on Fuel-Cell Performance via Mathematical Modeling. *Journal of The Electrochemical Society,* 163(7), p. F691.

Zhang, F.-Y.et al., 2009. Quantitative characterization of catalyst layer degradation in PEM fuel cells by X-ray photoelectron spectroscopy. *Electrochemica Acta,* 54(16), pp. 4025-4030.

Zhang, H., Li, J., Tang, H. & Lin, Y. P. M., 2014. Hydrogen crossover through perfluorosulfonic acid membranes with variable side chains and its influence in fuel cell lifetime. *Internationla Journal of Hydrogen Energy,* 39(28), pp. 15989-15995.

Zhang, J., 2008. In: J. Zhang, ed. *PEM Fuel Cell Electrocatalysts and Catalyst Layers.* Vancouver: Springer Science & Business Media, pp. 1-78.

Zhang, J. et al., 2006. PEM fuel cell open circuit voltage (OCV) in the temperature range of 23 °C to 120 °C. *Journal of Power Sources,* 163(1), pp. 532-537.

Zhang, X. & Shi, P., 2006. Dual-bonded catalyst layer structure for PEMFC. *Electrochemistry Communications,* Volume 8, pp. 1129-1234.

Zhan, Z. et al., 2007. Gas diffusion throguh differently structured gas diffusion layers for PEMFC. *Journal of Power Sources,* Volume 32, p. 4443..

Zhao, Q. & Benziger, J., 2013. Mechanical Properties of Perfluoro Sulfonated Acids: The Role of Tepmerature and Solute activity. *Journal of Polymer Science,* 51(11), pp. 1-11.

Zhiani, M. & Majidi, S., 2013. Effect of MEA conditioning on PEMFC performance and EIS response under steady state condition. *International Journal of Hydrogen Energy,* Volume 38, pp. 9819 -9825.

Zhuo, Z. et al., 2010. Internation Journal of Hydrogn Energy. *Durability study of Pt–Pd/C as PEMFC cathode catalyst. ,* Volume 35, pp. 1719-1726.